

UNIVERSITY OF HELSINKI

REPORT SERIES IN ASTRONOMY

No. 36

The multiscale interstellar medium from massive molecular clouds to cold cores

Emma Mannfors

ACADEMIC DISSERTATION

Faculty of Science
University of Helsinki
Helsinki, Finland

To be presented, with the permission of the Faculty of Science of the University of Helsinki, for public criticism in Physicum E204 on 30.01.2026 .

Helsinki 2026

Cover picture: Integrated intensity map of ^{12}CO molecular line emission in the λ Orionis West cloud, observed with the TRAO telescope as part of the B-FROST project (PAPER-III).

ISSN 1799-3024 (print version)
ISBN 978-952-84-1977-8 (print version)
Helsinki 2026
Helsinki University Print (Unigrafia)

ISSN 1799-3032 (pdf version)
ISBN 978-952-84-1978-5 (pdf version)
ISSN-L 1799-3024
<http://ethesis.helsinki.fi/>
Helsinki 2026

Electronic Publications @ University of Helsinki
(Helsingin yliopiston verkkojulkaisut)

Emma Mannfors: **The multiscale interstellar medium from massive molecular clouds to cold cores**, University of Helsinki, 2026, 69 p. + appendices, University of Helsinki Report Series in Astronomy, No. 36, ISSN 1799-3024 (print version), ISBN 978-952-84-1977-8 (print version), ISSN 1799-3032 (pdf version), ISBN 978-952-84-1978-5 (pdf version), ISSN-L 1799-3024

Abstract

Our galaxy is filled with clouds of cold gas and dust. From giant molecular clouds in the Milky Way's spiral arms down to dense cores and protostars, the processes driving cloud evolution and star formation are complex. Clouds are affected by local and global magnetic fields, turbulence at multiple scales, as well as feedback from bright stars. It is impossible to observe or simulate all physical processes simultaneously and thus assumptions must always be made.

I have performed and analyzed observations of molecular clouds from parsec-to core-scales using continuum FIR emission and MIR extinction, CO spectra, and polarization data. Multiple clouds in the Orion cloud complex have been studied to understand high-mass star-formation and feedback from massive stars. I have created a catalog of hundreds of dense Galactic clumps to better understand how clump properties change as a function of environment. Synthetic observations have been performed to better understand how limited observations and data reduction affect derived conclusions in PAPER-IV.

Large-scale surveys are crucial for comparing molecular clouds and star formation throughout the Galaxy, as each telescope and reduction method introduces different sources of uncertainty into data. The catalog of PAPER-I includes observations of around 50 clouds imaged with the same telescopes and analyzed using consistent methods. Even then, conclusions are affected by worsening resolution with increasing distance to the cloud; nonetheless we detect a sample of clumps and cores in a variety of environments and at different evolutionary states. PAPER-III also presents one of the first publications on the new B-FROST CO($J=1-0$) survey, focusing on a molecular ring surrounding a bright OB star. When other sources in the B-FROST survey are analyzed with the same methods, we will be able to evaluate more systematically how star-formation processes differ depending on the environment.

The formation of high-mass stars is poorly understood. Orion is the nearest high-mass star-forming region and enables us to observe these regions at high resolution.

While the λ Orionis ring (PAPER-III) is located at the edge of an H_{II} region, the OMC-3 filament (PAPER-II and PAPER-V) is located in a less evolved region which does not yet host much star formation. In both PAPER-II and PAPER-V we detected filament widths lower than the canonical width of 0.1 pc, and in PAPER-II a significant difference between filament and clump properties extracted from data at 20'' and 40'' resolutions.

This thesis presents analysis of dense clumps and molecular clouds in a wide sample of Galactic environments. The data and results presented herein will allow the astronomical community to better understand the interaction between molecular clouds, cores, and their environment.

Acknowledgements

Thank you to my pre-examiners, assistant Prof. Jouni Kainulainen and Prof. Alvaro Hacar, and to Prof. Hacar for also acting as opponent. The work involved in this thesis would not have been possible without support from our research group and colleagues. To my supervisor Dr. Mika Juvela, thank you for always giving careful and thorough feedback while still allowing me to be an independent researcher. When I started my master's thesis in the ISM group, Mika S. was always ready to help with questions about academia, programming, and the history of Finnish black metal. I am happy that our group expanded again after the pandemic. Job, you have been such a good addition to our group. It has been a pleasure to work on B-FROST with you and you have brought up so many important questions about our analysis. I know you have a strong future in research. Devika, thank you for being a friend and support during my final two years. You helped so much with questions about SOC and radiative transfer, and even more with support when I was stressed about life and academia. (And thank you for the cat pictures from Kerala and the many restaurant recommendations.) All three of you have been great conference friends. Laura Z. allowed me to join your ALMA proposals and to help organize a conference already during my master's; both of these were crucial in helping me to secure funding for my PhD. Thank you to Jorma Harju for help especially with astrochemistry questions. During my PhD I have worked closely within the Galactic Cold Cores collaboration, which is composed of the most welcoming, supportive, and clever people who have made work a pleasure. I'll miss our annual workshops (and am especially sad about missing the Lake District).

This research was possible due to funding from the PAPU doctoral program as well as the Vilho, Yrjö, and Kalle Väisälä grant from the Finnish Academy of Science and Letters. I am grateful to everyone who believed in my research.

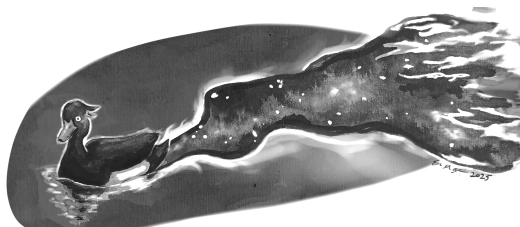
I had the best desk-neighbors. Natalia, I am sad that we did not get to spend much time as officemates but the few months between starting my PhD and lockdown were nice. Alex, you were a wonderful neighbor. We had a lot of fun bopping to music at our desks. You have spent so much effort on social activities for the astrocorridor, thinking up thoughtful gifts for people who are leaving, and in general being a wonderful person. To the rest of the Party Office (Mikko, Atte, and Vesa), thank you for the company. We were the best at distracting each other with coffee breaks, random discussions, and music. I can't list the whole astrocorridor, so instead I will only say: I'll miss all of you.

When the astrocorridor coffee breaks weren't enough, I could always go visit the A-corridor. Especially thank you to Deanna for allowing me to complain about

academia, for all the queer and art events outside of work, and for pictures of your cats. Thank you to Anna for the PhD peer support, knitting company, and for the few times you were able to drag me to the gym.

To the board and actives of Meridiaani ry, it has been fun to help organize events even after my retirement. The organization has grown so much during my time at the university and I can see Meridiaani is in good hands.

The past two Kumpulan Speksi productions have provided a much-needed break from academia and a creative outlet. Special thanks first to the dancers of Kuolema Korjaa, who showed me that rejoining speksi after 4 years was a good idea. Likewise,



thank you to the actors of Minä Olen Puu. You are the best plants, bunnies, and wizards a person/duck could ask for. I gratefully acknowledge the directors for casting me in my dream roles: Giant Duck who is also an Elder god as well as Wizard with Fancy Hat. The costume team,

the actors of Kuolema, and dancers and makeup crew of Puu also deserve special thanks. I'll miss the close community we formed backstage both years.

I have made so many friends during my time at the university. Thank you to Sampo, my friend since the English philology days. To all the friends I made in Kumpula, even those who managed to escape physics, especially Rene for also getting me back into knitting. Thank you to my former tutor and current GM Ilmo and the rest of our tabletop gaming squad: Hanna, Lepe, Teo, Satu, and Veera. (RIP Ulfgard, Grog, and whoever we manage to get killed between writing these acknowledgements and my defense).

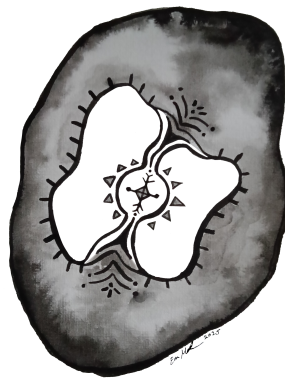
Thank you to my parents, Berit and Keijo, for helping me financially during my studies, and thank you for not complaining when I decided I wanted to switch majors to astrophysics. Thank you to Berit for catsitting Luna whenever I had a conference, interview, or other event where I wanted to avoid MeowMeowMeow in the background. I could not have done this without your support.



Finally, thank you to Luna: my research assistant, lap(top) warmer, and personal opera singer. You could not read this (because you are a cat), but thank you for attending every meeting, lecture, and workshop. You helped with B-FROST observations (thank you for not breaking the telescope by walking on my laptop) and always kept me company. You have been the best (and loudest) PhD companion and nicest loaf I could ever ask for. May you always have a sunbeam and a warm lap to lay in. Until we meet again, rest easy little friend.



Oi Ukko ylijumala
Toatto vanha taivahaini
Sie olet pilvien pitäjä
Hattarojen hallitsija
Nostan luontoni lovesta
Syntini syvästä maasta
Polvin maasta potkaelen
Tuorehista turpehista
Nouse kuuta kazomah
Tähtiä tähyämäh
Tunnikseni voimakseni
Veäkseni voimakseni
Havun alta haltieni
Havun alta hattu peänä
Kiven alta kinnas keäässä
- SKVR I4 13. / SKVR I4 1754.
Hoto, Iron-Poavilan vaimo
Uhtua, Viena 1846/1894



This carpenter to blessem him bigan,
And seyde, 'help us, seinte Frideswyde!

This man is falle, with his astromye,
In som woodnesse or in som agonye;
I thoghte ay wel how that it sholde be!
-Geoffrey Chaucer, *Canterbury Tales*,

The Milleres Tale 3450

List of publications

Publications included in this thesis

Paper I: (Mannfors et al., 2021)

Mannfors, E., Juvela, M., Bronfman, L., et al., *Characterization of dense Planck clumps observed with Herschel and SCUBA-2*, A& A, (2021) vol. 654. pp. A123

Paper II: (Mannfors et al., 2025)

Mannfors, E., Juvela, M., Liu, T., & Pelkonen, V.-M., *Comparison of Herschel and ArTéMiS observations of massive filaments*, A& A, (2025) vol. 695. pp. A242

Paper III: Mannfors et al., subm.

Mannfors, E., Vorster, J., Montillaud, J., et al., *B-FROST: B-Fields and starFormation across Scales with TRAO II: λ Orionis*.

Paper IV: (Juvela et al., 2022)

Juvela, M., Mannfors, E., Liu, T., & Tóth, L. V., *Synthetic Next Generation Very Large Array line observations of a massive star-forming cloud*, A& A, (2022) vol. 666. pp. A74

Paper V: (Juvela & Mannfors, 2023)

Juvela, M., & Mannfors, E., *Filaments in the OMC-3 cloud and uncertainties in estimates of filament profiles*, A& A, (2023) vol. 671. pp. A111

Publications not included in this thesis

Montillaud et al., *in prep*

Vorster et al., *in prep*

Kou et al. (2025)

Eden et al. (2024)

Mai et al. (2024)

Ren et al. (2023)

Liu et al. (2022)

Juvela et al. (2020)

List of abbreviations

ALMA	Atacama Large Millimeter/submillimeter Array
APEX	Atacama Pathfinder EXperiment
B-Fields	Magnetic fields
CMF	Core mass function
ESA	European Space Agency
ESO	European Southern Observatory
FIR	Far-infrared
FWHM	Full-width at half maximum
GMC	Giant molecular cloud
HMSF	High-mass star-formation
HPBW	Half-power beamwidth
IR	Infrared
IRDC	Infrared dark cloud
IMF	Initial mass function
ISM	Interstellar medium
ISRF	Interstellar radiation field
JCMT	James Clerk Maxwell Telescope
LOS	Line of sight
MBB	Modified blackbody (function)
MC	Molecular cloud
MIR	Mid-infrared
ngVLA	Next-generation Very Large Array
NIR	Near-infrared
PACS	Photodetector Array Camera and Spectrometer
RT	Radiative transfer
SF	Star formation
SFE	Star formation efficiency
SED	Spectral energy distribution
SN(e)	Supernova(e)
SPIRE	Spectral and Photometric Imaging REceiver
TRAO	Taeduk Radio Astronomy Observatory
UV	Ultraviolet
YSO	Young stellar object

List of symbols, constants, and units

Symbols

Symbol	Meaning	Units	Notes
ν	frequency	Hz	
λ	wavelength	m	
M	Mass	M_{\odot} , kg	
T	temperature	K	
t_{ff}	Free-fall time	s, yr	Eq. 4.5
ρ	density	kg m^{-3}	
$N(\text{X})$	Column density of element/molecule X	cm^{-2}	
$n(\text{X})$	Volume density of element/molecule X	cm^{-3}	
A_v	extinction	mag	
Σ_{X}	Surface density of X	$[\text{X}] \text{pc}^{-2}$	
c_s	Sound speed	km s^{-1}	
β	dust opacity spectral index		
κ_{ν}	dust opacity	$\text{cm}^2 \text{g}^{-1}$	
τ_{ν}	optical depth		
\odot	Sun		

Constants

Symbol	Meaning	Value (SI)	
G	Gravitational constant	6.6743×10^{-11}	$\text{m}^3 \text{kg}^{-1} \text{s}^{-2}$
k_B	Boltzmann constant	1.380649×10^{-23}	$\text{m}^2 \text{kg s}^{-2} \text{K}^{-1}$
h	Planck constant	$6.62607015 \times 10^{-34}$	$\text{m}^2 \text{kg s}^{-1}$
c	speed of light in a vacuum	299 792 458	m s^{-1}

Units

Symbol	Meaning	Corresponding unit in SI
\circ	degrees	$180^\circ = \pi^{\text{rad}}$
'	arcminutes	$60' = 1^\circ$
"	arcseconds	$60'' = 1'$
sr	steradians	radian ²
pc	parsecs	$3.086 \times 10^{16} \text{ m} = 3.26 \text{ lightyears}$
au	astronomical units	$1.496 \times 10^{11} \text{ m} = 4.85 \times 10^{-6} \text{ pc}$
K	Kelvins	$0 \text{ K} = -273.15 \text{ C}$
M_\odot	Solar masses	$1.989 \times 10^{30} \text{ kg}$
Jy	Jansky	$10^{-26} \text{ W m}^{-2} \text{ Hz}^{-1}$

Molecules

Symbol	Definition	Other common isotopomers	Fist detection in the ISM
H	(Atomic) Hydrogen		
H ₂	Molecular Hydrogen		1970
H _I	Neutral (atomic) Hydrogen		
H _{II}	Ionized Hydrogen		
CO	Carbon monoxide	¹² CO, ¹³ CO, C ¹⁸ O	1970
CO ₂	Carbon dioxide		1989

Contents

1	Introduction	1
1.1	The Milky Way galaxy	2
1.2	A brief look at a star's lifecycle	3
1.3	The interstellar medium (ISM)	7
1.4	Aims of this thesis	7
1.5	Structure of this thesis	9
2	Background	10
2.1	The components of the ISM	10
2.1.1	Gas	10
2.1.2	Dust	10
2.2	The scales of the ISM	11
2.3	Physical processes affecting the ISM	13
2.3.1	Gravity	13
2.3.2	Turbulence	13
2.3.3	Magnetic fields	15
2.3.4	Pressure	16
2.4	Continuum radiative transfer	17
2.4.1	The blackbody function	17
2.4.2	The radiative transfer equation	17
2.4.3	Optical depth τ	18
2.4.4	The modified blackbody (MBB) function	19
2.5	Line radiative transfer	21
2.5.1	Estimating molecular column densities	23
3	Observing the ISM	25
3.1	Emission and extinction	25
3.2	The atmosphere	26
3.3	Telescopes	27

3.4	Large-scale observing programs	30
3.4.1	Galactic Cold Cores Survey and follow-up projects	30
3.4.2	B-FROST	31
3.5	Chemistry of the ISM and how to observe molecular clouds	31
3.5.1	Formation and destruction of molecules in the ISM	31
3.5.2	Carbon monoxide (CO)	32
3.6	How to "observe" simulations	33
4	Molecular clouds	35
4.1	The properties of molecular clouds	37
4.1.1	Larson relations	37
4.1.2	Star formation rate and star formation efficiency	38
4.1.3	Timescales of star formation	38
4.1.4	Molecular cloud lifetimes	39
4.2	The difficulty in determining distance to molecular clouds	40
4.3	Large-scale Galactic features	41
4.4	Filaments	42
4.4.1	The infinite cylinder theory of filaments	43
4.4.2	Formation and fragmentation of filaments	43
4.4.3	Filament properties	44
4.4.4	Filaments and magnetic fields	46
5	Clumps, cores, and star formation	48
5.1	The virial theorem	50
5.1.1	Virial mass	50
5.2	Jeans criterion	51
5.3	The initial- and core mass functions (IMF and CMF)	52
5.4	Properties of clumps and cores	53
5.4.1	How to extract cores from the data	53
5.4.2	The shape of clumps	53
5.5	High-mass star formation (HMSF)	55
5.6	Feedback	56
5.7	Theories of star formation	57
5.7.1	Monolithic core collapse	58
5.7.2	Competitive accretion	58
5.7.3	Global hierarchical collapse	59
5.7.4	Inertial-inflow	59
5.8	YSO classes	60

6	Summary of the publications	62
6.1	Paper I	62
6.2	Paper II	64
6.3	Paper III	65
6.4	Paper IV	66
6.5	Paper V	67
7	Concluding remarks	68
	Bibliography	69

1 Introduction

Interstellar space is not empty. Instead, massive clouds of cold gas and dust fill our galaxy. It is from these dense clouds that new generations of stars and their planets form. Billions of years ago, our own Sun formed from a similar collapsing cloud of gas. The elements in our planet and even our bodies were once part of the interstellar medium (ISM). To truly understand the birth and evolution of our galaxy, we must understand the ISM.

For millennia people throughout the world have observed dark patches across the night sky: in many Aboriginal cultures the Emu in the sky crosses the plane of the Milky Way from its feet in the Great Rift to its head in the coalsack nebula (Norris, 2007). Even today people detect familiar shapes in interstellar clouds, such as the Eagle in Orion (cover photo, PAPER-III), Cat's eye nebula, and the Butterfly nebula. In the modern era, research into the cold ISM began in 1904 when Johannes Hartmann presented observations of calcium lines that originated between the variable star δ Orionis and the Earth (Hartmann, 1904). With the advent of infrared (IR) astronomy in the 1960s (Rieke, 2009), the importance of this field has grown.

Properties of natal gas determine the conditions under which stars and their planets form, as well as affect the type of stars which are born. Especially the prevalence of high-mass stars will drive strong effects which can change the shape of galaxies. Many large-scale simulations of galaxy evolution are not able to resolve the process of star formation (SF) in detail, and must instead rely on models to calculate number of stars formed and their effect on the galaxy. Even outside the field of ISM research, the processes occurring in these cold regions of space are crucial. Despite advances in observations, theory, and modeling of the ISM important questions about the energy transfer between scales, the earliest stages of SF, and the driving factors of cloud evolution remain.

In interstellar space, concentrations of gas and dust form massive clouds (Fig. 1.1a). Gas concentrates onto dense filaments such as those in the Orion nebula (frames a,b,e). Within these filaments, density fluctuations and local gas movements create overdensities (frame f), clumps which can under the right conditions begin to

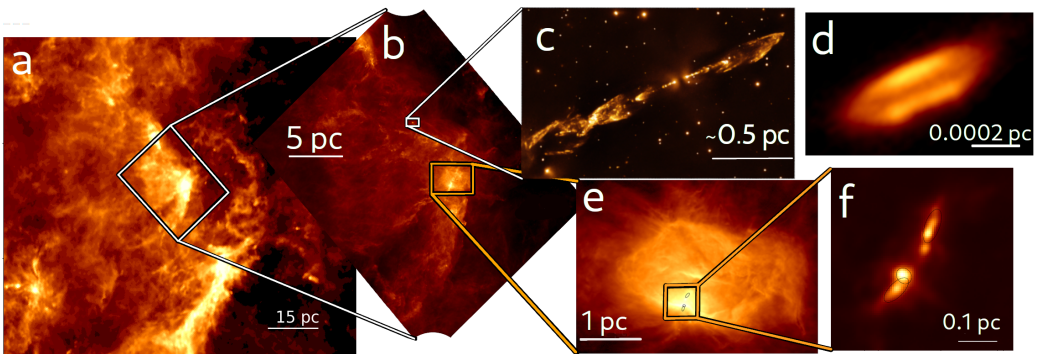


Figure 1.1: The Orion region at different scales. (a): Parsec-scale cloud filaments observed with the *Planck* telescope. (b): Zoom-in on a dense region, imaged with the *Herschel* telescope. (c): Outflows from a young star imaged with the VLT. (ESO/M. McCaughrean) (d): The same young star in its protostellar envelope with ALMA. (ALMA (ESO/NAOJ/NRAO)/ Lee et al.) (e): A dense giant molecular cloud imaged with *Herschel*. (f): Zoom-in onto dense cores within the cloud imaged with the SCUBA-2 instrument on the JCMT.

collapse under gravity, forming stars. Young stellar objects (protostars; YSOs) are still surrounded by their protostellar envelopes (frame d) and can create energetic outflows and jets (frame c).

1.1 The Milky Way galaxy

The Milky Way is a Sbc-type spiral galaxy of (baryonic) mass $M_{\text{MW}} \approx 0.21 \times 10^{12} M_{\odot}$ ⁽¹⁾ based on recent Gaia observations (Watkins et al., 2019). In addition to a dark matter halo and billions of older stars extending up to 1 kpc above and below the Galactic plane, the Galaxy contains a large amount of cold gas, dust, and young stars, which are concentrated in the Galaxy’s spiral arms (Karttunen et al., 2010). This dense gas disk extends to around 100 pc above and below the plane of the Galaxy but is around 20 kpc in diameter (Heyer & Dame, 2015). Neither the thickness of the thin molecular gas layer nor its midpoint are constant across the Galaxy. Observations of small, high-velocity CO clouds and faint CO emission suggest the presence of a second molecular disk, three times wider than the thin

⁽¹⁾ $M_{\odot} = 1$ solar mass, $\sim 1.989 \times 10^{30}$ kg

CHAPTER 1. INTRODUCTION

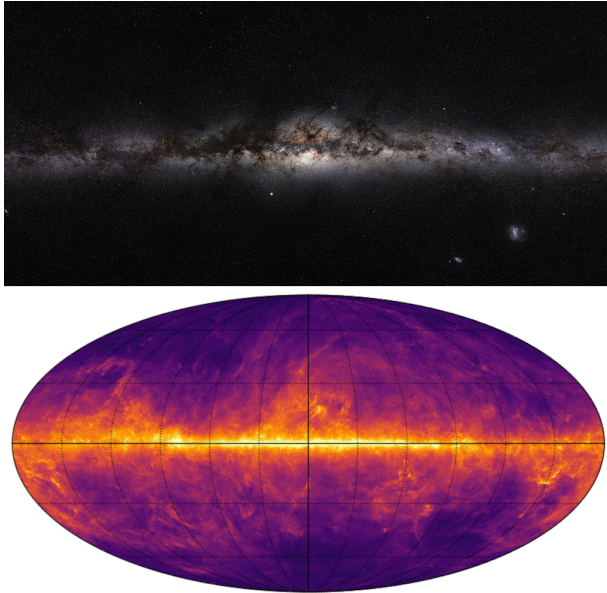


Figure 1.2: (Top): The disk of the Milky Way galaxy in optical wavelengths from the GigaGalaxy Zoom project (ESO et al., 2009). The light comes from the stars in the disk of the Galaxy. The cold ISM is seen as dark clouds blocking the background stars. Credit: ESO/S. Brunier. (Bottom): Planck 857 GHz ($\sim 350 \mu\text{m}$) all-sky map, showing the cold dust in the Galaxy in infrared emission. Accessed through the *Planck* archive (IRSA, 2025).

molecular disk (Dame & Thaddeus, 1994; Malhotra, 1994; Magnani & Smith, 2010), and comparable in thickness to the atomic hydrogen (H_I) disk (Heyer & Dame, 2015). As clouds in the thick disk correlate with the spiral arms, it is suggested that the gas in the thick molecular disk has been expelled from the thin disk by feedback and supernovae from high-mass SF (HMSF; Dobbs et al., 2011; Heyer & Dame, 2015). When viewed from the Earth 90% of the SF comes from the inner Galaxy ($\ell = -60$ to 60 degrees). In 3D space, half of the SF of the Galaxy also takes place within the molecular ring ($R_\text{gal} \leq 5.8 \text{ kpc}$; Elia et al., 2022). The Galaxy, as seen from Earth, is shown at optical and IR wavelengths in Fig. 1.2. In optical, the cold gas forms a dark web across the band of bright stars. In IR, however, the cold dust becomes visible due to its own emission. Hereafter, the term *the Galaxy* with a capital G refers to the Milky Way galaxy.

1.2 A brief look at a star’s lifecycle

Stars are born from collapsing clouds of gas and dust within the dense ISM. Gas within these clouds often forms filamentary structures (Elmegreen & Elmegreen, 1979; Schneider & Elmegreen, 1979; Bally et al., 1987; Myers, 2009; Molinari et al., 2010; André et al., 2010; Men’shchikov et al., 2010, see Fig. 1.3a). Internal turbu-

1.2. A BRIEF LOOK AT A STAR'S LIFECYCLE

lence, external pressure, gravity, and magnetic fields can cause further fragmentation of these filaments, creating dense clumps and cores. With enough mass to overcome the dissipative effects of turbulence and pressure, cores can begin to collapse and matter will accrete onto the protostellar core (Fig. 1.3b). As the core's density increases, so does the temperature until conditions allow nuclear fusion to begin (at around $T \sim 3 \times 10^6$ K; Reid & Hawley, 2006). The most important properties of a star are its mass and, to a lesser extent, metallicity². More massive stars form and develop faster, which can disrupt further formation of low-mass stars. A star's evolutionary state and size can be described by its position on the Herzsprung-Russel (HR) diagram (Fig. 1.4), which plots the star's luminosity against its surface temperature. At birth, protostars follow the Hayashi curve (vertical dashed line in Fig. 1.4; Hayashi, 1961; Hayashi & Hoshi, 1961) at a temperature around 2000 K regardless of mass, and then move along Henyey tracks (Fig. 1.4, colored solid lines; Henyey et al., 1955), increasing in temperature before reaching the Main Sequence. During its youth, a star is volatile, with large bursts. It can continue accreting mass from the surrounding medium, but ultraviolet (UV) radiation and stellar outbursts will begin to dispel the surrounding gas (Fig. 1.3c). This feedback is more pronounced with higher-mass stars. At birth, a star will be surrounded by an accretion disk from which planets can form.

The Main Sequence is the "middle age" of a star's lifetime (Fig. 1.3d, black line in Fig. 1.4). During this period, a star is relatively stable. Its properties (temperature, size, etc) are determined mostly by its mass. The spectral class of a star is denoted with a letter and number, with the classes (from hottest to coolest) being O, B, A, F, G, K, M L, T, Y, and with e.g. an M0 star being brighter than an M8 star. L, T, and Y stand for brown dwarfs, stars which fuse deuterium but have insufficient mass to fuse hydrogen. During the main sequence a star exists in hydrostatic equilibrium where it is supported against gravitational collapse by radiation pressure from hydrogen fusion happening in its core. How this fusion happens depends on the star's mass. Lower-mass stars such as the Sun fuse two hydrogen atoms into helium with the pp-chain (proton-proton chain); this method occurs when the core temperature is under 20 million Kelvin (Karttunen et al., 2010). In stars with mass over $\sim 1.5 M_\odot$, energy is mainly produced with the CNO cycle, where a series of reactions between carbon, nitrogen, oxygen, and one hydrogen atom eventually forms $^{12}\text{C} + ^4\text{He}$. Even during their lifetime, higher-mass stars thus create a wider array of heavier elements; furthermore due to high UV radiation, high-mass stars ($M_* \geq 8 M_\odot$) will ionize their environment. The main sequence phase lasts anywhere from one million to

²the fraction of mass composed of elements other than hydrogen or helium

CHAPTER 1. INTRODUCTION

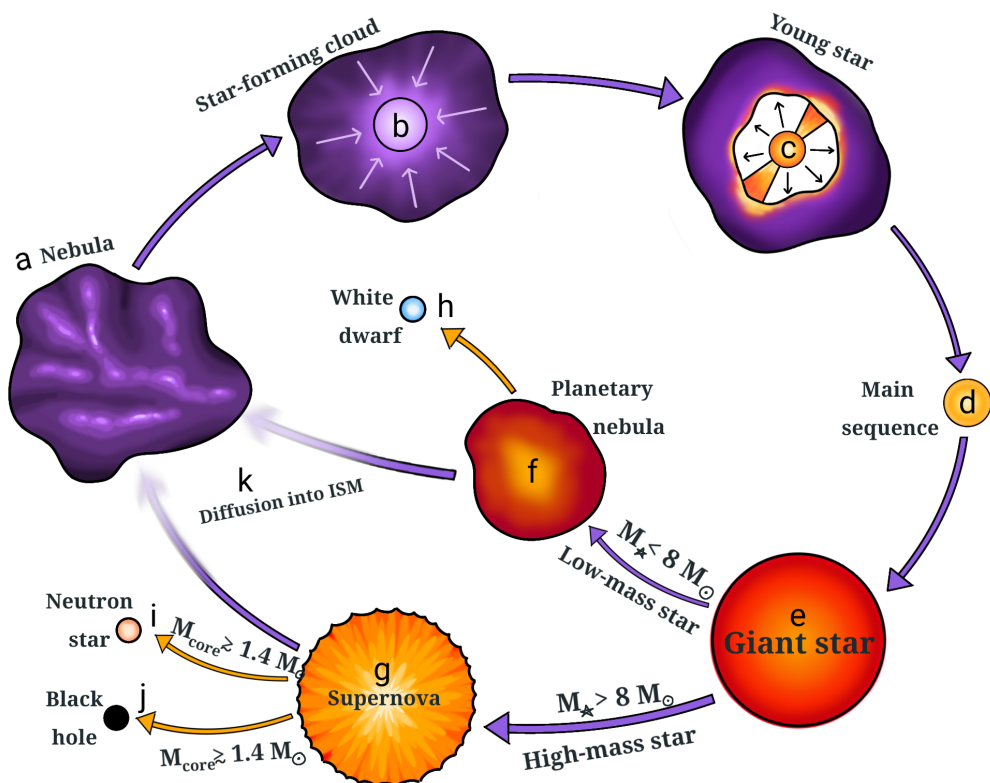


Figure 1.3: The life cycles of stars and gas within the ISM, from a nebula (a) to SF (b-c), stellar main sequence (d), to stellar death (e-j) and diffusion of enriched matter back into the ISM (k).

1.2. A BRIEF LOOK AT A STAR'S LIFECYCLE

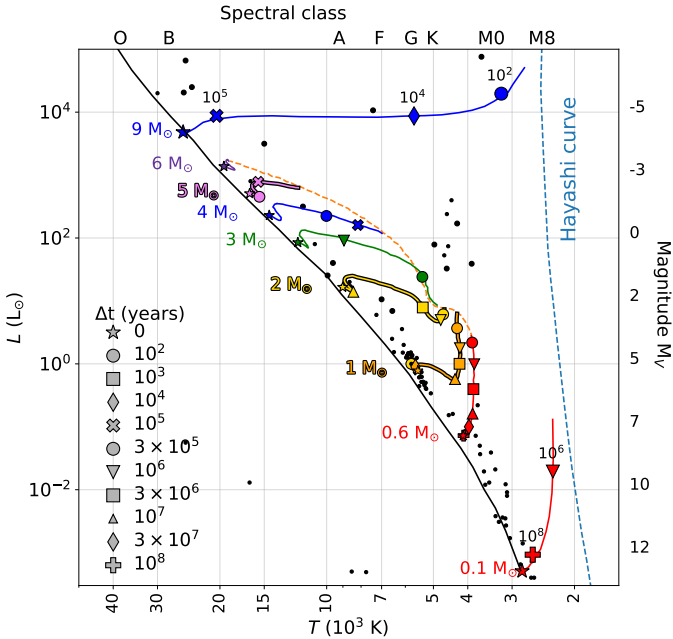


Figure 1.4: HR-diagram, showing the main sequence (black line), the region of Hayashi curves (blue dashed line), and the Henyey tracks (colored solid lines) for stars of masses 0.1 – $9 M_{\odot}$. The colored symbols represent the number of years since the onset of SF (Δt). The data for masses 0.6 – $6 M_{\odot}$ come from Fig. 10 of Palla & Stahler (1993), whose models do not include the vertical portion of the Henyey or Hayashi tracks. The black dots show the positions of some individual stars.

tens of billions of years. The higher a star's mass, the shorter the lifetime. The main sequence of a Sun-like star is \sim 10 billion years, whereas a high-mass O-type star will live for only \sim 3–10 million years and the lowest-mass M-type stars can live for hundreds of billions of years (Bertulani, 2013).

Once hydrogen in the star's core is depleted, death begins (Fig. 1.3e–j). Nuclear fusion of heavier elements (from helium up to iron) in shells around the core can stave off collapse for some millions of years, with higher-mass stars being able to fuse heavier elements. During its old age and death, the star will have massive outflows and bursts, emitting matter into the surrounding ISM and possibly producing dust. Stars more massive than $1.5 M_{\odot}$ will explode in a supernova at their death, further enriching the surrounding environment with heavy elements but also potentially throwing gas and dust out of the galactic disk. Depending on stellar mass, a star may explode completely, or collapse into a white dwarf, neutron star, or black hole. Most heavy elements present in the Universe are created during stellar old age and death.

1.3 The interstellar medium (ISM)

The ISM includes all baryonic matter within a galaxy not in stars, planets, or other solid bodies. It covers a wide array of scales, temperatures, and sizes. In the Galactic disk, the ISM makes up around 10–15% of the total (visible) mass (Ferrière, 2001).

The ISM is made up of three distinct phases: the cold neutral medium (CNM) at $T < 300$ K, the warm medium at $T \sim 10^4$ K (Field et al., 1969), and the hot ionized medium (HIM) at $T \sim 10^6$ K (McKee & Ostriker, 1977; Saintonge & Catinella, 2022). The cold medium is subdivided into molecular and cold atomic gas, and the warm ISM into warm neutral (WNM) and ionized (WIM) components. These phases are summarized in Table 1.1. In terms of volume, the HIM and WIM dominate, whereas most of the gas mass is located in the cold medium in galaxies like the Milky Way (Saintonge & Catinella, 2022). Around 75% of the cold ISM within nearby, late-type star-forming galaxies is atomic, mostly hydrogen. The remaining 25% is in molecular form (Saintonge & Catinella, 2022). At large scales, the cold ISM is concentrated near the Galactic plane, and within the spiral arms. At smaller scales, the ISM forms filamentary and clumpy clouds of dense matter, embedded within more diffuse gas. **Hereafter, the *ISM* will refer to specifically to the cold interstellar medium.**

In interstellar space, high-energy radiation such as UV photons from hot young stars heat matter so that any molecules are destroyed. Within dense clouds, particles are better shielded from the interstellar radiation field (ISRF) and have temperatures below 100 K. UV radiation cannot penetrate into the densest regions (density $\rho \geq 10^4$ atoms cm $^{-3}$), allowing molecules to exist. Hundreds of molecular species, including complex organic molecules (COMs), have been detected in the ISM; the Cologne Database lists around 330 molecules detected within the ISM or circumstellar shells³. COMs are defined as carbon-bearing molecules made of six or more atoms (Herbst & van Dishoeck, 2009), and some of the largest interstellar molecules are carbon fullerenes such as C₇₀ (Cami et al., 2010).

1.4 Aims of this thesis

SF research has often been fragmented due to its complicated nature. Recent efforts to connect observations at different scales and wavelengths have helped to form a more universal picture of the ISM and SF, but much work is still needed. This thesis connects observations from clump and core scales to those of molecular clouds.

³As of February 2025 (CDMS, 2025)

1.4. AIMS OF THIS THESIS

Component	T (K)	n (cm $^{-3}$)	Σ_{\odot} (M_{\odot} pc $^{-2}$)	\mathcal{M} (10 $^9 M_{\odot}$)
Molecular	10 – 20	10 2 – 10 6	~2.5	~1.3 – 2.5
Cold atomic	50 – 100	20–50	~3.5	≥ 6.0
Warm atomic	6 000 – 10 000	0.2–0.5	~3.5	≥ 6.0
Warm ionized	~8 000	0.2–0.5	~1.4	≥ 1.6
Hot ionized	~10 6	~0.0065		

Table 1.1: Properties of the different ISM components, adapted from Table 1 of Ferrière (2001). T is the temperature of the gas, n the number density of hydrogen nuclei near the Sun, Σ_{\odot} the azimuthally-averaged mass density per area at the solar circle, and \mathcal{M} the mass contained in the entire Milky Way. Both density and Σ_{\odot} depend on location in the Galaxy, and Σ_{\odot} and \mathcal{M} assume a composition of 70.4% hydrogen, 28.1% helium, and 1.5% metals.

Additionally, assumptions are necessary in science. Often, necessary data do not exist for a complete analysis of a certain region and in simulations, computational power limits the number of physical processes which can be calculated. When performing fitting of theories to models, our chosen parameters can strongly affect the derived properties of our data. In many papers, we have used models to attempt to quantify the effect of either assumptions or limited observations on our conclusions.

PAPER-I investigates a large number of cores and clumps in a wide selection of Galactic environments. With the catalog produced, we can estimate SF properties as a function of galactic environment, cloud mass, and evolutionary state. PAPER-II and PAPER-V study the OMC-3 filament in Orion at both the cloud and clump scale, in emission (PAPER-II) and extinction (PAPER-V). Furthermore, in these papers we have attempted to quantify sources of error in filament fitting procedures using models. PAPER-III studies dense clouds in the λ Orionis ring at large scales, attempting to characterize the effect of feedback on a molecular cloud (MC). As part of the B-FROST survey, λ Orionis will in the future be compared with the other B-FROST sources, giving a more coherent picture of MC evolution as a function of environment. PAPER-IV is a simulation paper, focusing on how a proposed telescope array would be able to recover properties of an MC in spite of line-of-sight (LOS) confusion.

CHAPTER 1. INTRODUCTION

1.5 Structure of this thesis

I provide the theoretical background for my research in Chapter 2 and discuss observing of the ISM in chapter 3. The next two chapters discuss important physical processes occurring on larger (cloud) scales (chapter 4) and small (clump and smaller) scales (chapter 5). Finally, I summarize the included publications in Chapter 6. Acronyms and symbols used in this thesis are listed before the table of contents.

2 Background

2.1 The components of the ISM

2.1.1 Gas

Roughly 99% of matter within the cold ISM is in gas form as ions, atoms, and molecules. As in the rest of the Universe, the ISM is composed primarily of hydrogen (H; 90.8% by number [70.4% by mass]), followed by helium (He; 9.1% [28.1%]). Heavier elements, called metals, make up around 0.12% [1.5%] of the ISM (Ferrière, 2001). Most of the detected molecules and all of the large ($n \geq 6$ atoms) molecules listed on the Cologne Database for Molecular Spectroscopy (CDMS, 2025) are organic, i.e. contain carbon (Herbst & van Dishoeck, 2009).

Molecules in the ISM were first detected in the 1930s by astronomers at the Mount Wilson Observatory (Merrill, 1934, 1936), who detected interstellar absorption of unknown origin at wavelengths between 3800–6700 Å in stellar spectra. These spectra were found to originate between the star and the Earth and correlated with transitions of simple molecular species (Swings & Rosenfeld, 1937; McKellar, 1940). In the following century hundreds of complex species have been found (Woon, 2025). Due to the extremely low densities and temperatures in the ISM which leads to extremely low rates of collisions, an atom or molecule which has been excited is more likely to stay in an excited state until it spontaneously decays. These so-called forbidden lines, which are not likely (or possible) in laboratory conditions on Earth, include the hydrogen 21-cm line, which is caused by a spin-flip transition of the hydrogen atom and has been crucial in the study of neutral hydrogen in the Galaxy.

2.1.2 Dust

Around 0.5–1% (by mass) of the ISM is within larger solid particles, known as dust (Ferrière, 2001). Most of the dust is composed of silicates and carbon compounds potentially surrounded by a layer of ice that range in radius a from ~ 10 nm to $0.5\ \mu\text{m}$ (Herbst & van Dishoeck, 2009). These are smaller than dust found in the

CHAPTER 2. BACKGROUND

Solar System ($a \sim 0.1\text{--}1\,\mu\text{m}$; Messenger et al., 2013) or on Earth ($a \sim 2.5\text{--}10\,\mu\text{m}$; EPA, 2023). Much of the interstellar dust is formed during the end of a star's life, in the outflows of asymptotic giant branch stars and after these stars' deaths, when the resulting stellar remnant star ionizes its ejecta (Cami et al., 2010).

Within the dense ISM, up to 60% of the oxygen that is not found in silicates is instead within ice mantles on dust grains (Boogert et al., 2015). Water is the dominant ice species, but many compounds (such as CO, CO₂, CH₄, NH₃, CH₃OH) are also detected as ices (Yamamoto, 2017). In dense cores water ice has a fractional abundance with respect to molecular hydrogen H₂ of around 10^{-4} , which is similar to that of gas-phase CO (Herbst & van Dishoeck, 2009). Solid-phase CO and CO₂ can have somewhat smaller abundances (Herbst & van Dishoeck, 2009), though all abundances depend on region. Ice must be shielded from UV radiation and so needs a certain column density to form: in the Taurus MC, water ice is only detected above extinction $A_{\text{v}} \geq 3^{\text{mag}}$. More volatile CO species require even lower temperatures and higher shielding to freeze out onto dust grains; CH₃OH ice is only observed above $A_{\text{v}} = 9 \pm 3^{\text{mag}}$ (Chiar et al., 1995, 2011; Whittet et al., 2011; Boogert et al., 2011, 2015).

Polycyclic Aromatic Hydrocarbons (PAHs)

Polycyclic Aromatic Hydrocarbons (PAHs) are large, carbon-based molecules of size from 30 up to 100 atoms (Herbst & van Dishoeck, 2009). Spectra of many star-forming galaxies, as well as the ISM of the Milky Way, show strong emission features at 3.3, 6.2, 7.7, 8.6, 11.2, 12.7, and 17.1 μm (Gillett et al., 1973; Li, 2020, Fig. 2.1). These emission lines are believed to result from the vibrational modes of PAHs (Leger & Puget, 1984; Allamandola et al., 1985) which have been excited by interstellar photons (Draine et al., 2021). The level of excitation of PAHs depends on both the chemical and physical properties of the PAHs themselves, as well as on the properties of the starlight illuminating the dust (Draine et al., 2021), making them a useful tool to understand dust composition and the local environment. UV radiation from massive stars decreases PAH abundance due to dissociation of the molecules.

2.2 The scales of the ISM

The ISM has structures on all scales, from galactic to sub-parsec, as illustrated in Fig. 2.2. Diffuse, ionized gas also exists outside galaxies (Fig. 2.2 a,b) but this gas can fall back onto a galactic disk and enrich the ISM. Spiral galaxies contain more (cool) gas and dust compared to elliptical galaxies and thus most stars are born in

2.2. THE SCALES OF THE ISM

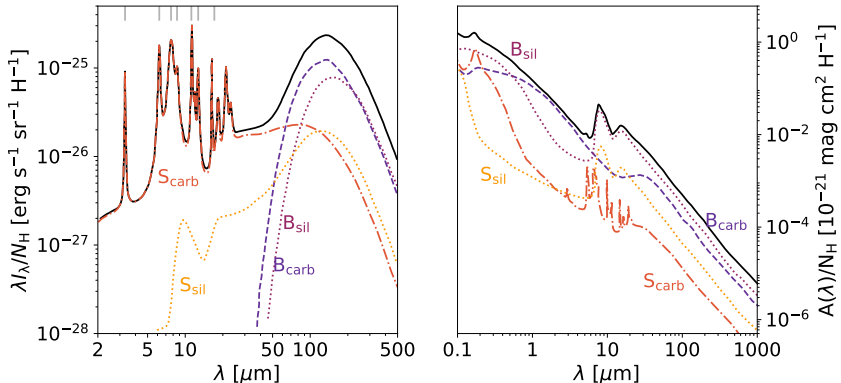


Figure 2.1: (Left): Model of dust emission from the diffuse ISM at high Galactic latitudes ($|b| \geq 25^\circ$), redrawn from Li & Draine (2001). (Right): Model for the contribution of different types of dust grains to the interstellar extinction, redrawn from Li & Draine (2001). B_{carb} and B_{sil} refer to big ($a \geq 250 \text{ \AA}$), and S_{carb} and S_{sil} to small carbonaceous and silicate grains, respectively. The carbonaceous small-grain curve includes contribution from PAHs. The vertical gray lines on the left frame mark the wavelengths of the main PAH features.

spiral or irregular galaxies. Figure 2.2c shows a spiral galaxy face-on. The central bulge, which contains more old stars is redder, while hot, young stars are shown in blue. Gas is preferentially located in the spiral arms, though star-forming regions also exist between spiral arms and further from the Galactic disk.

The largest individual clouds are known as giant molecular clouds (GMCs) at scales of hundreds of parsecs and are found where gas is the most dense. The sites of the most massive SF are often located at the intersections of multiple colliding filaments or sheets, where gas is accreted onto a central hub (Fig. 2.2d). Smaller filaments and MCs (Fig. 2.2e) are present in lower-mass regions such as those at higher galactic latitudes. Filaments are not uniform structures, but instead can fragment further into denser clumps (Fig. 2.2f). Clumps in turn can contain smaller cores that can each give birth to one or a few stars (Fig. 2.2g). I adopt the commonly-used definitions: **clumps** are overdensities of gas with sizes $\sim 1 \text{ pc}$, which may in the future form a cluster of stars. A **core** is a structure within a clump of size $\sim 0.1 \text{ pc}$, which can form one or a few stars (Offner et al., 2014; Motte et al., 2018a). Cores can be divided into starless and protostellar cores based on the presence of YSOs within the core. Starless cores do not show signs of current SF, but can be either prestellar (likely to form stars in the future) or unbound starless (too diffuse for gravitational

collapse).

2.3 Physical processes affecting the ISM

Four phenomena control the formation, evolution, and dissipation of structure within the ISM: gravity, turbulence, magnetism, and pressure, illustrated by the virial theorem (Eq. 5.1).

2.3.1 Gravity

Matter is attracted to matter through gravitational attraction. This force is incredibly weak, especially at the large scales within the ISM. Gravitational force between two particles of masses m_1 and m_2 at separation d is defined by $F_G = (G \times m_1 \times m_2)/d^2$, where G is the gravitational constant. Dense cores are often assumed to be spherical structures. The gravitational energy Ω_G of a homogeneous sphere is described by

$$\Omega_G = \frac{3GM^2}{5R}, \quad (2.1)$$

where R is the radius of the sphere and M its mass.

2.3.2 Turbulence

Interstellar turbulence describes the random gas flows within the ISM. Turbulent energy can be injected into the ISM at large scales by (Elmegreen & Scalo, 2004):

- stars (protostellar winds, expanding H_{II} regions, O star and Wolf-Rayet winds, supernovae)
- galactic rotation in the shocks of spiral arms or bars
- gaseous self-gravity through swing-amplified instabilities and cloud collapse
- Kelvin-Helmholtz and other fluid instabilities
- Galactic gravity during disk-halo circulation, the Parker instability, and galaxy interactions,

and at smaller scales with (Elmegreen & Scalo, 2004)

- sonic reflections of shock waves hitting clouds

2.3. PHYSICAL PROCESSES AFFECTING THE ISM

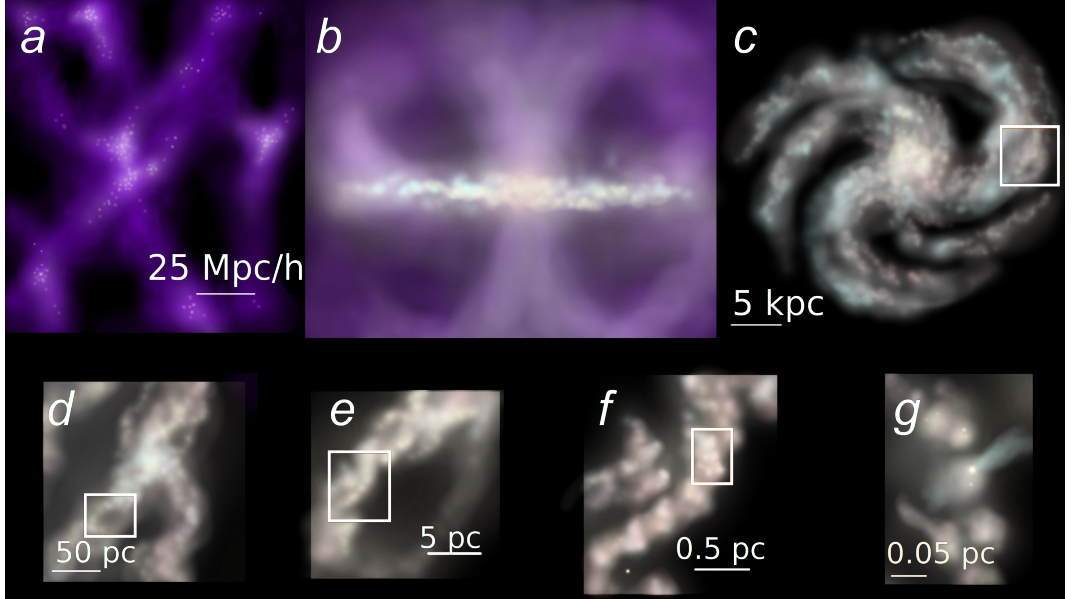


Figure 2.2: Schematic view of the scales of gas and dust. The white boxes in most frames show the zoom area onto the next region. (a) The cosmic web, with the diffuse intergalactic medium in purple. Each white dot represents a large galaxy. Inspired by images produced by the Millenium simulations (MPA, 2025). (b,c) A spiral galaxy. Frame b shows the galaxy edge-on. The circumgalactic medium (CGM) is drawn in purple, showing a central outflow as well as accretion back onto the galactic disk. Frame c shows the same galaxy face-on. The CGM is not shown, but rather the spiral arm structure is visible. Star-forming regions with hot young stars are shown in bluish color. (d) A parsec-scale hub-filament system, where the northern and two southern filaments are colliding, feeding SF in the region. (e) An individual filament which is beginning to fragment. (f) Clumps within the fragmenting filament (g) Zoom into one clump to show sub-parsec scale cores. A few YSOs are visible within the cores, as is an outflow from a massive YSO in the central core. Figure produced by the author.

CHAPTER 2. BACKGROUND

- cosmic ray streaming and other instabilities
- field star motions and winds
- energy cascades from larger scales.

Turbulence within the ISM at all but the smallest scales is usually supersonic, suggesting that turbulence alone cannot form small-scale clumps and cores (Padoan et al., 2001; Larson, 2003). This transition from supersonic to subsonic turbulence occurs at scales around 0.05–0.1 pc (Larson, 2003), near the size of cores and the theorized characteristic width of interstellar filaments (see Sect. 4.4.3). Interstellar turbulence can be estimated using spectral line observations, where the width of the spectral line gives the level of turbulence. High-resolution studies of clouds with no ongoing SF show low velocity dispersions suggesting that turbulence in the early stages of SF is close to or even below the scale of thermal motions (Pillai et al., 2011; Sánchez-Monge et al., 2013; Beuther et al., 2015; Zhang et al., 2024; Beuther et al., 2025).

2.3.3 Magnetic fields

Unpolarized dust grains in the ISM are oriented randomly, but magnetic (B) fields can cause grains to align with the B field lines. Thus, observations of dust polarization are one of the strongest methods to understand the interstellar B field. The stokes I , Q , U , and V vectors are used to detect polarization of dust grains. The term I is the full intensity, Q and U are the linearly polarized intensities rotated 45° from each other, and V the circularly polarized intensity (Steinacker et al., 2013). The I , Q , and U vectors can be used to determine orientation of the plane-of-the-sky component of the magnetic field, as was done in the B-FROST project.

$$\Psi = 0.5 \text{atan}(U, Q) + \pi/2, \quad (2.2)$$

$$p = \frac{\sqrt{Q^2 + U^2}}{I}, \quad (2.3)$$

where Ψ is the polarization angle, p the polarization fraction, and the term $\pi/2 = 90^\circ$ describes the angle between the polarization and B-field vectors. Ψ gives the direction of the magnetic field, which can in turn be compared with structures and velocity fields in the ISM. These data together can help astronomers understand how (or if) magnetic fields in the ISM drive cloud evolution and the transport of gas. Polarization fraction p can be used to infer dust properties. It has been observed to be anticorrelated with local column density, likely as the B-field is also dependent

2.3. PHYSICAL PROCESSES AFFECTING THE ISM

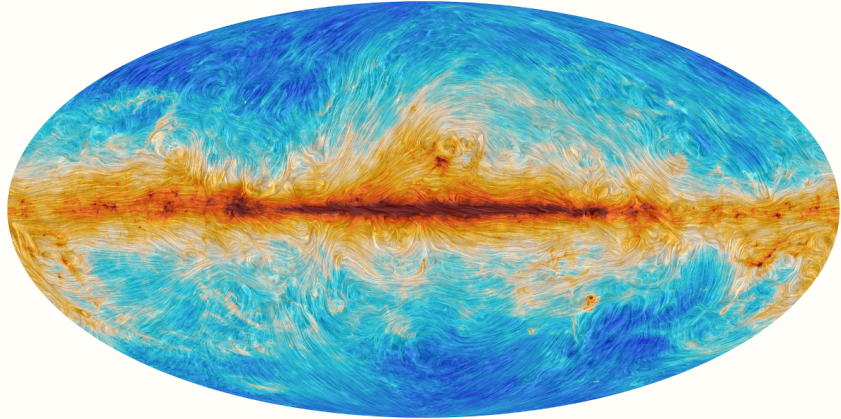


Figure 2.3: Map of the Galactic magnetic field from the *Planck* satellite, using polarized dust emission at 353 GHz. The colorscale corresponds to local gas column density, with red being the most dense and blue the most diffuse. Credit: ESA and the Planck Collaboration

on the local radiation field (Pattle et al., 2021); we also detect this anticorrelation in PAPER-III and B-FROST I. Combining hundreds of B-field measurements, Pattle et al. (2023) show that volume density is also anticorrelated with B-field strength. The large-scale Galactic B-field as observed by the Planck satellite is shown in Fig. 2.3 and illustrates how large-scale diffuse gas structures follow B-field lines.

2.3.4 Pressure

Gas surrounding a MC will exert pressure on the cloud due to particle collisions. Further external pressure comes from radiation, especially near bright stars and from outflows and feedback from high-mass YSOs. It can be estimated from the kinetic energy of the more diffuse material surrounding a dense cloud. This kinetic energy can be observed using spectral lines of the diffuse ISM, and if the spectral class of a star or YSO is known, the radiation pressure can also be estimated. Support from external pressure can confine a cloud that would otherwise have insufficient mass for gravitational collapse. In PAPER-III we have observed compression of the dense CO cloud surrounding a bright OB star. Several dense cores, at least one containing a YSO, are located in this region. These cores however do not appear to have sufficient mass for gravitational collapse without external support.

2.4 Continuum radiative transfer

2.4.1 The blackbody function

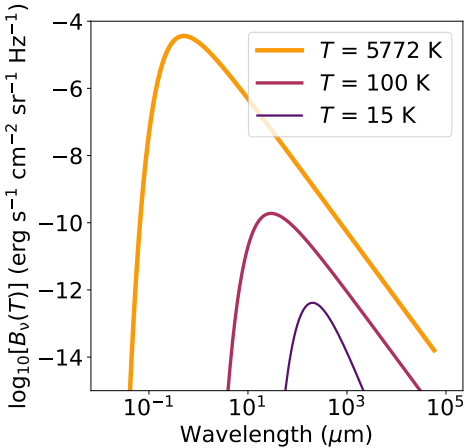


Figure 2.4: Blackbody spectra corresponding to the Sun ($T \sim 5772$ K, orange line) and an object at 100 K (red line). The plot includes the modified blackbody spectrum $B_\nu(T = 15\text{ K})\nu^{1.8}$ as a template for the emission of interstellar dust (dark line).

An object emitting as a black body has a continuous emission spectrum with total intensity and peak of emission corresponding solely to the object's temperature. Its emission is described by the Planck law

$$B_\nu(T) = \frac{2h\nu^3}{c^2} \frac{1}{e^{h\nu/k_B T} - 1}, \quad (2.4)$$

where h is the Planck constant, c the speed of light in a vacuum, k_B the Boltzmann constant, ν the frequency of the radiation, and T the temperature. In general, a hotter object will have higher intensity and be visible at shorter wavelengths. This is visible in Fig. 2.4; the emission of the Sun ($T \sim 5772$ K) peaks at around 500 nm, the emission of a blackbody at $T = 100$ K peaks at longer wavelengths around 30 μm .

2.4.2 The radiative transfer equation

Observed intensity represents a sum of all emission and absorption along a line of sight. To separate these components, radiative transfer (RT) modeling is often necessary. A radiation field is defined by its specific intensity $\bar{I}(\bar{x}, \bar{n}, \lambda)$, where \bar{x} is the location in space, \bar{n} the direction of propagation of the radiation, and λ the wavelength (or ν the frequency). The RT equation is (Steinacker et al., 2013)

$$\frac{dI}{ds} = -\kappa(s, \lambda)\rho(s)I(s, \lambda) + j(s, \lambda), \quad (2.5)$$

where the left-hand side represents the change in intensity over a distance s , the first term on the right-hand side $[-\kappa(s, \lambda)\rho(s)I(s, \lambda)]$ the extinction due to matter,

2.4. CONTINUUM RADIATIVE TRANSFER

and the second term $[j(s, \lambda)]$ the emission of the medium. In the case of dust, the intensity results from thermal emission by dust grains themselves, as dust re-emits absorbed radiation at wavelengths $\geq 1\text{ }\mu\text{m}$ (Steinacker et al., 2013). The source function is the ratio between the emission coefficient j and extinction coefficient κ

$$S_\nu \equiv j_\nu / \kappa_\nu. \quad (2.6)$$

These quantities are dependent on wavelength. To complicate matters, dust in the ISM is generally made up of a mixture of various grain sizes and compositions, with differing optical properties.

Dust grains in the ISM can scatter light, in other words change the direction of propagation of photons. Extinction is thus defined as the combination of the effects of scattering and absorption, while light scattered from other directions can also increase the intensity of observed radiation. Scattering from dust is strongest in near-infrared (NIR¹) and shorter wavelengths, but light scattered at mid-infrared (MIR²) wavelengths from grains deeper inside dense cores, known as coreshine, can also be observed (Steinacker et al., 2010).

It is often assumed that dust grains are in thermal equilibrium with the local radiation field at an equilibrium temperature T_{eq} , defined as the temperature at which energy of emitted radiation equals the energy of radiation absorbed by a dust grain (Steinacker et al., 2013). As this temperature depends explicitly on the grain properties, T_{eq} can vary even within the same location between gains of different size and composition. Due to their smaller heat capacities, smaller grains and PAHs do not reach equilibrium temperature and instead have strong fluctuations, emitting at temperatures larger than T_{eq} (Steinacker et al., 2013).

2.4.3 Optical depth τ

Optical depth describes the attenuation of background radiation over a line of sight, and is defined as $d\tau_\nu \equiv \kappa_\nu ds$. By including τ_ν in Eq. 2.5, one can derive a complete RT solution (Mangum & Shirley, 2015).

$$I_\nu = I_\nu(0)e^{-\tau_\nu} + \int_0^\tau \exp \left[-(\tau_\nu - \tau') \right] S_\nu d\tau', \quad (2.7)$$

where the first term describes the attenuation of background radiation by matter, and the second term describes the combination of emission and attenuation of said

¹ $\lambda_{\text{NIR}} \approx 0.7 - 2.5\text{ }\mu\text{m}$

² $\lambda_{\text{MIR}} \approx 3 - 25\text{ }\mu\text{m}$

CHAPTER 2. BACKGROUND

emission by matter. This equation ignores scattering, but that is usually a valid approximation at far-infrared (FIR³) and radio wavelengths.

Whether the medium is optically thick or thin affects the form of the RT equation which can be used. In the optically thin case, $\tau_\nu \ll 1$, thus $1 - e^{-\tau} \approx \tau$, and the RT equation (Eq. 2.7) can be approximated as $I_\nu = I_\nu(0)e^{-\tau_\nu} + B_\nu\tau_\nu$, making the observed intensity directly proportional to the amount of matter along the line of sight. In the optically thick case, $\tau \gg 1$, Eq. 2.7 reduces to $I_\nu = S_\nu$, so that intensity depends on the source function only (and in case of dust only on the dust temperature). With the exception of protostellar cores and clouds of very high column densities, such as the infrared dark clouds (IRDCs), FIR dust emission is typically optically thin.

2.4.4 The modified blackbody (MBB) function

Dust emission at mid-infrared and longer wavelengths can be used to estimate column densities by observing emission and assuming a dust opacity κ_ν . Submillimeter dust opacities are approximated with a power-law of $\kappa_\nu \propto \nu^\beta$, where β is the opacity spectral index. In the optically thin case, Eq. 2.7 can be written as

$$I_\nu = S_\nu(1 - e^{-\tau}) \quad (2.8)$$

$$\sim B_\nu(T_{\text{dust}}) \times \tau \quad (2.9)$$

$$= B_\nu(T_{\text{dust}}) \times S_\nu \times \kappa_0 \left(\frac{\nu}{\nu_0}\right)^\beta. \quad (2.10)$$

Both T and β determine the shape of the Spectral Energy Distribution (SED), or the intensity of the source at different wavelengths.

From observations, it is estimated that $\beta \approx 1.6$ – 2.4 in the dense cold ISM (Dupac et al., 2003; Juvela et al., 2015b; Yi et al., 2018). Lower indices of $0.8 \leq \beta \leq 1.6$ are found in warmer, more diffuse matter (Dupac et al., 2003). For a sample of 52 dense regions within the Galaxy we calculated $\beta = 1.7 \pm 0.1$ (PAPER-I) and find similar values of ~ 1.8 in the λ Orionis East cloud in PAPER-III. Dust temperature has been noted to anticorrelate with β . The strength of this anticorrelation can provide information on the chemical composition, structure, and grain size distribution of interstellar dust (Ossenkopf & Henning, 1994; Kruegel & Siebenmorgen, 1994; Mennella et al., 1998; Dupac et al., 2003; Meny et al., 2007; Compiègne et al., 2011; Juvela et al., 2011). Part of this observed anticorrelation is due to observational noise (Shetty et al., 2009a,b; Juvela & Ysard, 2012; Juvela et al., 2013).

³ $\lambda_{\text{FIR}} \geq 25 \mu\text{m}$

2.4. CONTINUUM RADIATIVE TRANSFER

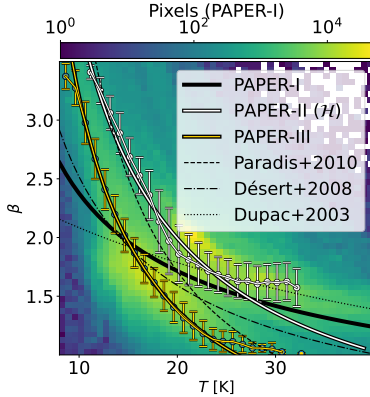


Figure 2.5: Histogram of dust temperature against opacity spectral index β for the 52 fields included in PAPER-I, with the calculated $T - \beta$ relation shown in black. Fits to *Herschel* data from PAPER-II and PAPER-III are shown with white and yellow solid lines, respectively. Mean β per 1 K temperature bin is shown with 1σ errorbars. We add fits from the literature: Paradis et al. (2010) (dashed line), Désert et al. (2008) (dash-dotted line), and Dupac et al. (2003) (dotted line). Reproduced from Fig. 5a of PAPER-I.

However, simulations performed in PAPER-I show that the anticorrelation is not due to noise alone; the same findings have been found within other cold clouds and near the galactic poles (Fig. 2.5; Dupac et al., 2003; Désert et al., 2008; Paradis et al., 2010; Planck Collaboration et al., 2014; Juvela et al., 2015b). *Herschel* data from PAPER-II and PAPER-III also show this anticorrelation. This (unpublished) finding is shown in Fig. 2.5. The relations are steeper than that calculated in PAPER-I, at $\beta_{\text{OMC-3}} \propto T^{-0.95}$ and $\beta_{\lambda\text{Ori}} \propto T^{-1.21}$ but are similar to the fit of Paradis et al. (2010).

The dust opacity κ_ν describes the absolute value of the optical depth relative to the total ISM mass, however the reference dust opacity κ_0 has been observed to depend on location and environment (Stepnik et al., 2003; Juvela et al., 2015b,a; Lewis et al., 2022). Beckwith et al. (1990) quoted an often-used reference dust opacity of $\kappa_0 = 0.1$ at $\nu_0 = 1000$ GHz, but κ_0 can also be estimated for example by using gamma rays or K-band extinction and total hydrogen column density (Lombardi et al., 2014; Lewis et al., 2022). In BFROST I we perform this fitting, finding $\kappa_0 \approx (5.2 - 10.2) \times 10^{-3} \text{ cm}^2 \text{ g}^{-1}$ at 353 GHz. This difference in κ_0 propagates to estimates of column density, with a higher value of κ_0 lowering estimates of $N(\text{H}_2)$ in PAPER-III.

If assuming the optically thin case, the flux detected from a source can be described as $F_\nu = \Omega \times B_\nu(T) \times \tau_\nu$, where Ω is the source solid angle. Using an observed SED, one can fit a modified blackbody (MBB) spectrum:

$$F_\nu = F_{\nu,0} \frac{B(\nu, T)}{B(\nu_0, T)} \left(\frac{\nu}{\nu_0} \right)^\beta, \quad (2.11)$$

CHAPTER 2. BACKGROUND

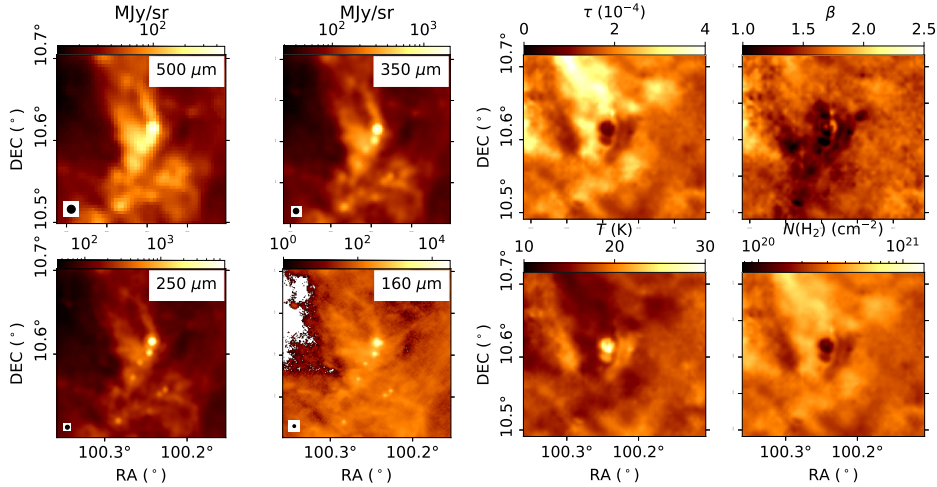


Figure 2.6: MBB analysis of an interstellar cloud from PAPER-I. (Left): A part of the Monoceros MC, G202, in four wavelengths (*Herschel* SPIRE 500, 350, 250 μm and PACS 160 μm). The black circles in the lower left show the beam size for each instrument. (Right): Maps of optical depth $\tau_{250\mu\text{m}}$, opacity spectral index β , temperature T , and column density $N(\text{H}_2)$ obtained from MBB fits at the PSW resolution.

where F_ν is the flux at a frequency ν , $F_{\nu,0}$ the flux at a reference frequency ν_0 , and $B(\nu, T)$ the Planck function at temperature T . Figure 2.6 shows *Herschel* observations of a dense cloud on the left, and the results of MBB fitting on the right. MBB fitting is complicated by different dust populations along a line of sight as assuming only one temperature component along the LOS can underestimate column density. Fits with multiple temperature components are feasible and reduce error, but come at significantly increased computational costs (Juvela, 2023).

2.5 Line radiative transfer

RT of spectral lines follows similar principles as continuum radiative transfer, where κ and j are based on populations of atoms or molecules at differing energy levels. Figure 2.7 shows the pathways of energy change in atoms and molecules between upper (u) and lower (l) energy states. A , B , and C are the rates of spontaneous radiative de-excitation, stimulated radiative (de-)excitation, and collisional (de-)excitation, re-

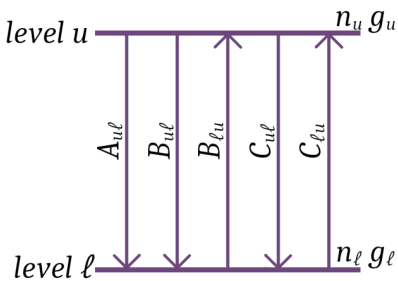


Figure 2.7: Schematic of energy level transitions between an upper energy level u and lower energy level ℓ , with arrow and subscript denoting the direction of transfer.

spectively. Particles of course cannot be spontaneously excited and so A only applies from upper to lower levels.

Molecular lines can exhibit varying optical depths. In many dense MCs, ^{12}CO is optically thick whereas other common isotopologs such as ^{13}CO and especially C^{18}O , as well as dense gas tracers such as NH_3 , can be optically thin. This is not always the case, for example in B-FROST observations of λ Orionis E in PAPER-III we detect several dense cores in which ^{13}CO also is optically thick. By observing a combination of species with different optical depths or multiple transitions one can estimate both excitation temperature T_{ex} and optical depth τ_ν .

Critical line density

The critical density (n_{crit}) for a transition between u and l is defined as the density at which the rate of spontaneous radiative de-excitation is equal to the rate of collisional de-excitation

$$n_{\text{crit}} = \frac{A_{ul}}{\langle \sigma_{ul} v \rangle}, \quad (2.12)$$

where $\langle \sigma_{ul} v \rangle$ is the collisional rate coefficient averaged over a Maxwellian distribution. For gas with a density much larger than n_{crit} , the upper energy state is sufficiently populated by collisions so that $T_{\text{ex}} = T_{\text{kin}}$. In CO, this density is quite low at $\sim (2 - 3) \times 10^3 \text{ cm}^{-3}$ for the $J = 1-0$ transition (Heyer & Dame, 2015; Saintonge & Catinella, 2022).

In local thermodynamical equilibrium (LTE), level populations follow the Boltzmann distribution.

$$\frac{n_u}{n_l} = \frac{g_u}{g_l} \exp \left(- \frac{\Delta E}{k_B T_{\text{ex}}} \right), \quad (2.13)$$

where n is the population of upper u and lower l levels, g is the statistical weight of particles on both levels, and $\Delta E = \Delta(h\nu)$ is the difference in energy between the

CHAPTER 2. BACKGROUND

two states. The excitation temperature T_{ex} describes the temperature at which level populations would be according to the Boltzmann distribution. In LTE, the kinetic and excitation temperatures of the gas are equal, but especially many of the optically thin lines show sub-thermal excitation with $T_{\text{ex}} < T_{\text{kin}}$.

Radiation temperature

Assuming an intensity of radiation I , a black body emitting at the same intensity has a temperature defined as the radiation temperature T_R (Mangum & Shirley, 2015).

$$T_R \equiv \frac{c^2}{2k_B\nu^2} \Delta I_\nu, \quad (2.14)$$

where ΔI is the difference in intensity between the source and the background. When observing a source in the sky, the source radiation temperature is estimated based on the intensity detected in a reference region containing only background emission and compared to the intensity detected on the source

$$T_R = f \left[J_\nu(T_{\text{ex}}) - J_\nu(T_{\text{bg}}) \right] \left[1 - \exp(-\tau_\nu) \right], \quad (2.15)$$

where the filling factor f describes the fraction of the telescope beam that is filled by the source and J_ν is defined by $J_\nu = \frac{c^2}{2k_B\nu^2} B_\nu$ (Mangum & Shirley, 2015).

2.5.1 Estimating molecular column densities

The column density of molecules in an upper energy state N_u can be related to the optical depth by (Mangum & Shirley, 2015)

$$N_u = \frac{3h}{8\pi^3|\mu_{lu}|^2} \left(e^{h\nu/k_B T} - 1 \right)^{-1} \int \tau_\nu dv, \quad (2.16)$$

where μ_{lu} is the dipole matrix element relating to the transition rate A and τ_ν is integrated over velocity v . Total column density can then be estimated by assuming Boltzmann distribution-like populations on other excitation levels at temperature T_{ex} . When a molecule is optically thin, column density can be estimated directly from the integrated intensity of the observed line. Column density estimation is more difficult in the optically thick case, and for this reason it is common to observe ^{12}CO and ^{13}CO together, estimate $N(^{13}\text{CO})$ from the optically thin ^{13}CO line, and then assume a ^{12}CO -to- ^{13}CO -ratio (R) to estimate the total CO column density. This method was used to estimate CO column density in the B-FROST project using a

2.5. LINE RADIATIVE TRANSFER

variable R from simulations by Szűcs et al. (2014). C¹⁸O observations are often used in conjunction with ¹²CO and ¹³CO observations with the same methods, providing a view of denser gas.

3 Observing the ISM

At optical wavelengths, the ISM of our galaxy is visible in absorption, as a dark band covering light from background stars (Fig. 1.2, left). Cold dust emits radiation at IR and longer wavelengths (Fig. 1.2, right) approximately according to the MBB function (Eq. 2.11). Cold gas which has not begun to form stars will be visible in the millimeter and submillimeter range and protostars at shorter NIR and MIR wavelengths.

Photometry, spectroscopy, and polarimetry can all be used to study the ISM. Photometry measures the brightness of sources within a certain wavelength range, spectroscopy the emission as a function of wavelength, and polarimetry the polarization of interstellar dust grains. Polarimetry can be used to approximate the strength and direction of the magnetic field.

3.1 Emission and extinction

As illustrated by Fig. 1.2, gas in the ISM can be observed both through emission at IR and radio wavelengths, and using extinction of background starlight at MIR and shorter wavelengths. While much of this thesis focuses on emission, extinction has been used in PAPER-V to probe the structure of OMC-3, and in PAPER-III (and B-FROST I) to fit for κ_0 . Extinction A_v is correlated to column density, often with the assumed ratio of $N(\text{H}_2)/A_v = 10^{21} \text{ cm}^{-2} \text{ mag}^{-1}$ (Bohlin et al., 1978; Sadavoy et al., 2012). Extinction can be calculated by measuring the reddening of background stars or galaxies, as more blue light than red is extinguished by the ISM. The extinction maps used in PAPER-III and the B-FROST project were obtained using stars from the 2MASS¹ survey and the NICEST method, which calculates NIR color-excess to estimate extinction (Lombardi & Alves, 2001; Lombardi, 2009). Another method to calculate extinction, used e.g. in PAPER-V, is to interpolate the background surface brightness over the source and calculate the attenuation of the light from the source to estimate τ_ν . Extinction requires sufficient column density of gas for starlight to

¹Two-micron all-sky survey

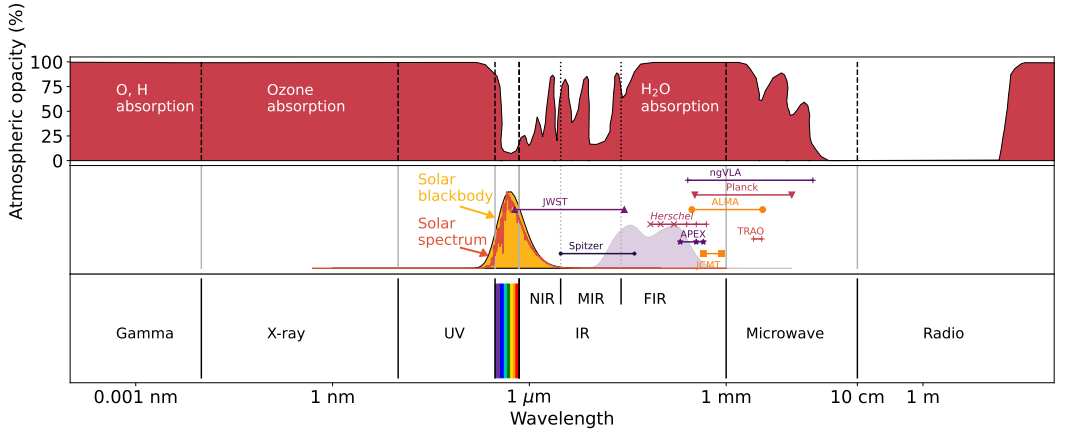


Figure 3.1: Top: Transmission of the atmosphere. Middle: The wavelength ranges of telescopes included in this thesis. The solid orange curve shows the solar blackbody spectrum overplotted with the true solar spectrum (red) from NREL (2025), and the fainter purple curve the combined MBB spectra of interstellar dust with components at temperatures of 10, 20, 50, and 100 K. All blackbody spectra are normalized to have similar intensities. Bottom: the wavelength ranges. The x-axis is the same in all frames.

be affected (and a sufficient number of background stars), but if gas or dust becomes optically thick background starlight is no longer visible and this fitting gives only a lower limit of column density.

3.2 The atmosphere

The atmosphere is effective in blocking radiation at wavelengths shorter than ~ 100 nm and longer than a few meters. In between these regions, water vapor absorption also blocks some incoming radiation, which is why ground-based telescopes must be built at high altitudes and in dry regions. However, the atmosphere is transparent at two windows: the optical window from ~ 300 nm to $2\ \mu\text{m}$, and the radio window at wavelengths of $\sim 1\ \text{cm}$ – $10\ \text{m}$. Atmospheric opacity as a function of wavelength is shown in Fig. 3.1, top.

In practice, this means that observing from the ground is only possible in the visible, NIR, and radio wavelengths. However, even at these wavelengths the atmosphere introduces some attenuation and adds noise. In contrast, space telescopes have sig-

nificantly higher risk, high cost, and high environmental impact due to launches but are not affected by the atmosphere. The wavelength range of some IR and radio telescopes are shown in Fig. 3.1, middle panel.

3.3 Telescopes

Single-dish telescopes use a single main mirror or lens (with additional optical elements) to focus light into a receiver. This light may pass through filters or other instruments. The resolution of a telescope θ depends on the wavelength of the radiation λ and on the angular diameter of the dish D as $\theta \approx \frac{\lambda}{D}$. Therefore a radio telescope must be significantly larger than an optical telescope to achieve the same resolution, but there are obviously limits on the size of a single antenna. Interferometers are used to achieve a higher resolution than would be possible with single dishes, as the resolution of an interferometer depends on the distance between the two most distant antennae (the baseline). Signals from each antenna pair are correlated in Fourier space to achieve a finished image with very high resolution.

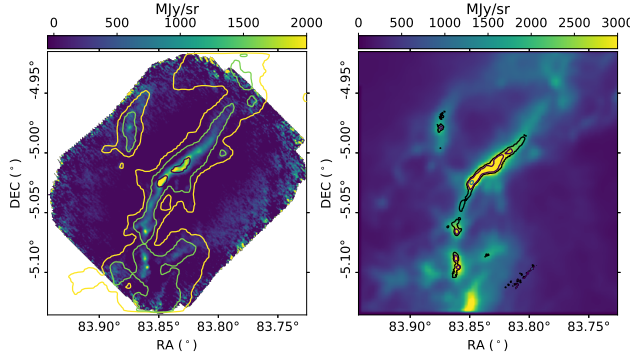


Figure 3.2: Intensity maps of OMC-3 in Orion with the ground-based APEX telescope (left) and space-based *Herschel* telescope. Contours are at levels of 500, 1000, and 3500 MJy sr⁻¹. The maps have been background-corrected to have a uniform zero-point.

reduction also filters away large-scale structures (larger than the size of the detector array). Figure 3.2 shows a filament in Orion Molecular Cloud (OMC) 3, observed from the ground (left) and space (right). The larger-scale extended structure is not detected in ground-based observations. To combat data loss from interferometric

Interferometers also have a maximum recoverable scale, or the largest size of structures visible with the instrument. Due to the correlation of signals from interferometric antennae, all large-scale structure is filtered out. A similar loss of large-scale emission can occur in ground-based submillimeter observations where observations are done by scanning receivers over the source. The atmosphere introduces noise into the observations, which must be removed. This sky-noise

3.3. TELESCOPES

and ground-based observations, high-resolution data are often combined with low-resolution single-dish observations to detect emission on both small and large scales, as was done in PAPER-II and PAPER-V.

Space telescopes

In this thesis, the *Herschel*, Planck, Gaia, and Spitzer satellites play a role. Other notable space observatories include the James Webb Space Telescope (JWST) and the Hubble Space Telescope (HST).

- **Spitzer:** Spitzer was a NIR/MIR space telescope, launched in 2003. Its main mission lasted until 2009, and after depletion of the coolant its "warm phase" observations lasted until 2020 (Werner et al., 2004; NASA, 2019). The infrared Array Camera (IRAC) on Spitzer observed at four wavelengths ($3.6\text{ }\mu\text{m}$, $4.5\text{ }\mu\text{m}$, $5.8\text{ }\mu\text{m}$, and $8\text{ }\mu\text{m}$) and the Multiband Imaging Photometer for Spitzer (MIPS) at wavelengths of $24\text{ }\mu\text{m}$, $70\text{ }\mu\text{m}$, and $160\text{ }\mu\text{m}$.
- **Planck:** The European Space Agency's (ESA) Planck space telescope operated at radio wavelengths. Its primary mission was to study the cosmic microwave background, but in doing so it also imaged the cold foreground dust within the Galaxy (ESA, 2006). *Planck* has also performed polarization observations, creating plane-of-sky component (dust and synchrotron) magnetic field maps.
- **Herschel:** ESA's *Herschel* Space observatory (Pilbratt et al., 2010) observed the sky at FIR wavelengths. *Herschel* was active during 2009-2013 and orbited at the second Lagrange (L2) point (1.5 million kilometers from Earth, in the direction opposite to the Sun; ESA, 2010). *Herschel* had three instruments, two of which have been used in this thesis: the Photodetector Array Camera and Spectrometer (PACS; Poglitsch et al., 2010) and the Spectral and Photometric Imaging REceiver (SPIRE; Griffin et al., 2010). The PACS instrument observed at 70 , 100 , and $160\text{ }\mu\text{m}$, and the SPIRE instrument at 250 , 350 , and $500\text{ }\mu\text{m}$. The Heterodyne Instrument for the Far Infrared (HIFI) instrument was a spectrometer observing between 625 - $240\text{ }\mu\text{m}$ and 208 - $157\text{ }\mu\text{m}$ with a spectral resolution of 0.7 km s^{-1} or better and a resolution of 11 - $44''$ (Herschel Science Centre, 2017) but has not been used in this thesis. Due to being in space, *Herschel* was able to image the extended structure of the ISM and was therefore instrumental in the development of this field.
- **Gaia:** ESA's Gaia observatory is an optical telescope created to measure the positions and velocities of ~ 2 billion stars, including many young stars and

CHAPTER 3. OBSERVING THE ISM

YSOs down to a magnitude of $20^{\text{(2)}}$). Gaia began operations in 2014. The third data release (DR3) was published in June 2022 and contains full astrometry for 1.46 billion stars as well as all-sky Galactic extinction maps (Gaia, 2022). This all-sky mapping has created an unprecedented image of the 3D structure of the Galaxy. Gaia YSOs can be correlated with MCs to more accurately determine distances to clouds, and YSO catalogs have been used to study the star formation status of cores.

Ground-based telescopes

For optimal observing conditions, ground-based telescopes are located preferentially at high elevation, in regions with low water vapor content. Many of the largest telescopes are located in the Atacama Desert in Chile, on La Palma in the Canary Isles, and on Mauna Kea, in Hawai'i. The studies presented in this theses used data mainly from three ground-based radio telescopes:

- **APEX:** The Atacama Pathfinder EXperiment (APEX) telescope has a 12-m main dish, observing at submillimeter and millimeter wavelengths (Güsten et al., 2006; ESO, 2025b). As of 2025 it hosts two facility instruments (nFlash, SEPIA) and four PI instruments (ArTéMiS, PI230, LASMA, CHAMP). The ArTéMiS (Architectures de bolometres pour des Telescopes a grand champ de vue dans le domaine sub-Millimetrique au Sol) instrument is a bolometer observing at 200, 350, and 450 μm (Revéret et al., 2014; APEX, 2024). It was built by CEA-Sarclay and IAS in France in collaboration with the European Southern Observatory (ESO).
- **JCMT:** The James Clerk Maxwell Telescope (JCMT) is a 15-m diameter submillimeter telescope located on Mauna Kea in Hawai'i. It hosts the Submillimetre Common-User Bolometer Array 2 (SCUBA-2) instrument, a bolometer camera which observes at 450 and 850 μm as well as the POL-2 polarimeter, also operating at the same wavelengths (EAS, 2025).
- **TRAO:** The Taeduk Radio Astronomy Observatory (TRAO) was a 13.7-m single-dish radio telescope which observed in the frequency range of 86 to 115 GHz (3.5–2.6 mm) located in the Republic of Korea (KASI, 2025). TRAO was decommissioned in 2024.

²Higher magnitude = fainter object; the faintest objects visible with the naked eye in a dark location is $\sim 6^{\text{mag}}$.

Interferometers

- **ALMA:** The Atacama Large Millimeter/submillimeter Array (ALMA) is a radio interferometer located in the Chajnantor plateau in Chile (NRAO, 2025a). Observing frequencies range from 35 GHz in band 1 to 950 GHz in band 10, with the largest antenna spacing being 16 km (ESO, 2025a). The largest scales recovered by 12-m array observations are $\sim 50''$, limited by the physical size of each antenna. The Atacama Compact Array (ACA), consisting of smaller 7-m antennae and one 12-m antenna, is able to observe larger structures.
- **ngVLA:** The next-generation VLA (ngVLA) is a proposed upgrade of the The Karl G. Jansky Very Large Array (VLA; NRAO, 2025b). The ngVLA will be composed of approximately 244 antennae spread across the continental USA, Hawai'i, and Puerto Rico, with a compact array located in New Mexico (NRAO, 2025c). The ngVLA is planned to observe at frequencies of 1.2 – 50.5 GHz and 70 – 116 GHz (249.8 – 5.9 mm and 4.2 – 2.6 mm).

3.4 Large-scale observing programs

While many observations focus on individual targets, the wealth of information provided by a large-scale survey is useful to draw more universal conclusions. Work in this thesis has been part of the Galactic Cold Cores and B-FROST surveys.

3.4.1 Galactic Cold Cores Survey and follow-up projects

Planck observed thousands of cold, dense clumps within the Galaxy. These were collected into the Planck Galactic Cold Clumps catalog (Planck Collaboration et al., 2011a,b, 2016a). A large *Herschel* key science program, Galactic Cold Cores (GCC; PI: M. Juvela), observed around 100 of these targets with the PACS and SPIRE instruments at higher resolution (Juvela et al., 2010; Montillaud et al., 2015). Sources from this *Herschel* catalog were later observed with ground-based instruments (JCMT, TRAO) in the TOP-SCOPE (TRAO Observations of PGCCs -SCUBA-2 Continuum Observations of Pre-protostellar Evolution) project (Liu et al., 2018). While PAPER-I was a direct part of the GCC project, also e.g. the ArTéMiS observations in PAPER-II were based on GCC sources.

CHAPTER 3. OBSERVING THE ISM

3.4.2 B-FROST

The B-Fields and staR fOrmatiOn across Scales with TRAO (B-FROST) survey was a TRAO key science program (PI: J. Montillaud) with observations of the ^{12}CO and ^{13}CO $J = 1-0$ transitions performed from November 2021 to March 2022 and November 2022 to March 2023 (Montillaud et al., *in prep.*; hereafter B-FROST I). We observed eight regions in six molecular clouds at a resolution of $\sim 40''$ and at large scales, with map sizes of up to 4° . In the B-FROST data we also include the Monoceros OB 1 region, which was observed with the same setup in 2019-2020 with the COMplete view of the MONoceros OB1 molecular complex (COMMON; PI: J. Montillaud) TRAO large program (Montillaud et al., *in prep.*). The B-FROST fields were chosen to represent a large sample of clouds in differing environments. This diverse sample at a uniform resolution enables comparison of gas dynamics and physical processes in multiple environments. Analysis of this project has started with a focus on MBM12 (Vorster et al, *in prep*) and λ Orionis (PAPER-III).

3.5 Chemistry of the ISM and how to observe molecular clouds

There are two factors affecting whether a certain molecule is detected: the actual existence of the molecule in the region, and whether the molecule can be observed with the instrument in question. The ISM contains hundreds of complex molecules, with the most common being the relatively simple species molecular hydrogen (H_2) and carbon monoxide (CO).

3.5.1 Formation and destruction of molecules in the ISM

Long timescales are required for the creation of H_2 . Estimated from cosmic-ray ionization, the time taken to convert H atoms to molecular H_2 is estimated to be $2.6/n_{\text{H}} \text{ Myr}$ (Goldsmith & Li, 2005; Heyer & Dame, 2015). The production of H_2 proceeds faster in denser regions: in shells at the edges of H_{II} regions, or through compression by stellar winds, supernovae, or shocks of convergent gas streams (Glover & Mac Low, 2007; Clark et al., 2012; Smith et al., 2014a). Molecular hydrogen is mainly formed on the surface of dust grains (Gould & Salpeter, 1963; Hollenbach & Salpeter, 1971) and is excited by UV photons from its electric-vibrational-rotational ground state into the Lyman ($\lambda < 1108 \text{ \AA}$) or Werner ($\lambda < 1008 \text{ \AA}$) bands. In $\sim 15\%$ of cases the molecule radiatively de-excites into an unbound state which dissociates the molecule (Heyer & Dame, 2015). As this dissociation is caused by UV radia-

3.5. CHEMISTRY OF THE ISM AND HOW TO OBSERVE MOLECULAR CLOUDS

tion, a larger percentage of the hydrogen is molecular deeper inside a cloud due to self-shielding and dust attenuation (Solomon & Wickramasinghe, 1969; Solomon & Klemperer, 1972; Hollenbach et al., 1971). At solar metallicity and at low radiation fields, Hydrogen gas is believed to be fully molecular at column densities above $(1 - 2) \times 10^{20} \text{ cm}^{-2}$ (Hollenbach et al., 1971; Sternberg & Dalgarno, 1995; McKee & Krumholz, 2010; Sternberg et al., 2014).

As H_2 is a symmetric molecule, it has no permanent dipole moment. Further, the rotational levels of the Hydrogen molecule have large spacing leading to inefficient (or no) radiation at the low temperature of dense molecular clouds (Heyer & Dame, 2015), instead requiring temperatures over 500 K or high amounts of UV radiation (Saintonge & Catinella, 2022). In warm or shocked matter, H_2 can be detected with rotational or vibrational emission, and through vibrational or UV absorption (Herbst & van Dishoeck, 2009). However, in most cases astronomers are forced to use other, more easily-detected compounds as tracers for molecular gas. The most common of these is CO with a typical abundance of 10^{-4} when compared to molecular hydrogen (Herbst & van Dishoeck, 2009).

The formation of CO molecules depends on local density and gas composition, with primary precursors being CO^+ in diffuse regions and OH in denser regions (Sheffer et al., 2008; Visser et al., 2009). Absorption of UV photons can dissociate the molecule and thus a shielding layer of gas is required for the stable formation of CO (van Dishoeck & Black, 1988; Visser et al., 2009). Modeling of photodissociation suggests that most C is bound into CO molecules at column densities over $(1 - 3) \times 10^{21} \text{ cm}^{-2}$ (Visser et al., 2009).

As required densities for CO formation are an order of magnitude larger than those required for H_2 formation, CO is not able to trace H_2 in low-density environments (Heyer & Dame, 2015). In very cold, dense regions CO can freeze out onto dust grains, once again leading to a lower gas-phase CO abundance (Bergin et al., 1995; Acharyya et al., 2007) and in these regions, dense gas tracers such as NH_2 , N_2H^+ , and NH_3 are used to trace molecular gas (Pillai et al., 2011). Ices on dust grains can however also be observed using their absorption in molecular vibrational transitions at multiple IR wavelengths (Boogert et al., 2015), revealing species that seem to be missing from gas-phase observations.

3.5.2 Carbon monoxide (CO)

CO was first observed in the ISM at 2.6 mm by Wilson et al. (1970). In contrast to H_2 , the low rotational energy transitions of the CO molecule ($J_u \leq 4$) are in the millimeter and submillimeter wavelengths and only 5-22 K above the ground state

CHAPTER 3. OBSERVING THE ISM

(Bolatto et al., 2013; Heyer & Dame, 2015; Saintonge & Catinella, 2022). Most interstellar C atoms in the gas phase combine with O to form CO molecules at $A_v \geq 1 - 3^{\text{mag}}$. As ^{12}CO is abundant at these densities, the lowest transition ($J=1-0$) is optically thick and thus radiation emitted does not escape the gas but is instead re-absorbed. The $J = 1$ level is thus well-populated even in regions with density lower than the critical density. High optical depth and low required density lead to strong CO line emission and an ease in detecting ^{12}CO (Heyer & Dame, 2015).

Masses of clouds are often derived from CO emission, using an assumed ratio of integrated intensity of CO ($W(\text{CO})$) to H_2 column density, known as the X-factor ($X(\text{CO})$). Changes in $X(\text{CO})$ thus affect the derived properties of molecular clouds. Both gamma-ray and dust emission observations suggest that $X(\text{CO})$ in the central Galaxy is 3-10 times lower than in the Solar neighborhood (Blitz et al., 1985; Sodroski et al., 1995). This ratio is highly uncertain in the outer Galaxy but likely increases due to photodissociation of CO in low-metallicity regions (Narayanan et al., 2012). $X(\text{CO})$ can also change within a single cloud (Pineda et al., 2008). Column densities probed by CO are limited to $A_v \sim 2 - 7^{\text{mag}}$, bounded by the decreasing CO abundance at the low end and by high optical depths and depletion onto grain surfaces at the high end (Pineda et al., 2008, 2010; Ripple et al., 2013; Heyer & Dame, 2015).

3.6 How to "observe" simulations

In simulations, one has a 3D understanding of the structure, kinematics, and other physical processes happening in the simulated cloud; however due to computational limitations one must always make assumptions about some aspects of physics. Theories of SF can be tested by creating synthetic observations from a full 3D simulated model cloud. The creation of synthetic single-dish observations proceeds as follows (illustrated in Fig. 3.3):

1. Use RT modeling to solve for temperature and energy level populations in the cloud and estimate radiation from the cloud and background along each line of sight.
2. Integrate this radiation over a certain time, creating an ideal observation with perfect resolution and no noise.
3. Using the half-power beamwidth ($HPBW$) of the simulated telescope, convolve the observations to lower angular resolution.

3.6. HOW TO "OBSERVE" SIMULATIONS

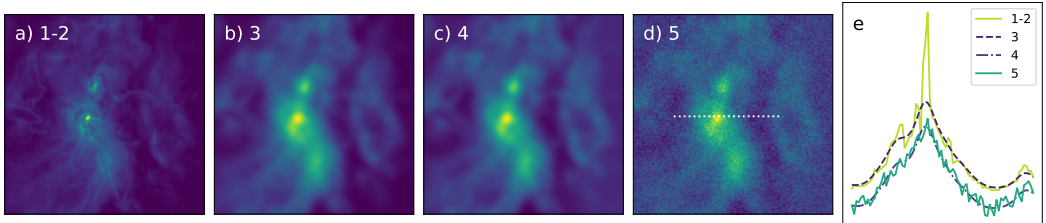


Figure 3.3: Creation of single-dish observations from the synthetic observations of N_2H^+ from PAPER-IV, zoomed in on a dense region. Values in the upper left corner correspond to the step. 1-2) Integrated intensity map of the ideal simulation. 3) Convolved with a beam of 15 pixels. 4) Removed all structure over 200 pixels in size. 5) Added Gaussian noise at 5% of intensity. Frame e shows the intensity profile across the clump, marked by the white dashed line in panel d.

4. Using the maximum recoverable scale of the observations, remove structures on scales larger than those visible to the telescope.
5. Finally, add Gaussian white noise to the observations to simulate the instrumental noise from the telescope and the effects of the atmosphere.

To simulate interferometric observations, these steps can be replaced by using programs such as CASA (CASA Team et al., 2022). In PAPER-IV, our synthetic observations were then analyzed using observational methods, testing whether one could recover the 3D properties of the cloud. The comparison of simulations and observations is crucial to understand the effect of assumptions made when analyzing astronomical images. They are also crucial in development of telescopes and instrumentation, as PAPER-IV was created at part of the ngVLA telescope planning process.

4 Molecular clouds

While the majority of clouds in the ISM are small and low-mass, most of the molecular mass in the Galaxy can be found in clouds with mass $M \geq 10^5 M_\odot$. MCs have a theoretical upper mass limit of $\sim 5 \times 10^6 M_\odot$ (Heyer & Dame, 2015). Figure 4.2 shows the location of many important molecular clouds, including those studied in this thesis. Most MCs are concentrated near the Galactic plane. The background image of *Planck* emission corresponds approximately to the column density of cold gas within the ISM; most gas is also concentrated within the Galactic plane. Those fields which are far from the plane (including G006 and L1780) are generally nearby, low-mass clouds. At a distance of ~ 400 pc, the Orion MC complex is the nearest high-mass SF region. Many other high-mass regions (including W40 and Monoceros OB1) are located at distances ≥ 500 pc and are in the plane of the Galaxy.

As UV radiation dissociates molecular gas, MCs cannot exist without an outer, shielding layer of atomic gas and dust. Due to the differing column density requirements for sufficient shielding and element-dependent chemistry, MCs can be thought of as having concentric layers (Fig. 4.1). The outer layer is composed of molecular hydrogen and atomic carbon. Interior to this layer, carbon is locked inside CO. In the densest regions CO freezes out onto dust grains, and dense gas tracers such as NH_2 and N_2H^+ become dominant (Heyer & Dame, 2015).

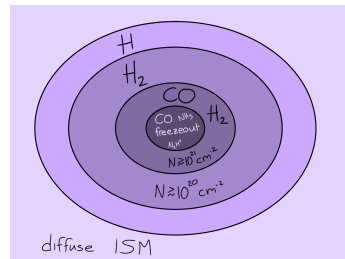


Figure 4.1: Schematic of a molecular cloud, with increasing density and decreasing temperature illustrated with darker colors.

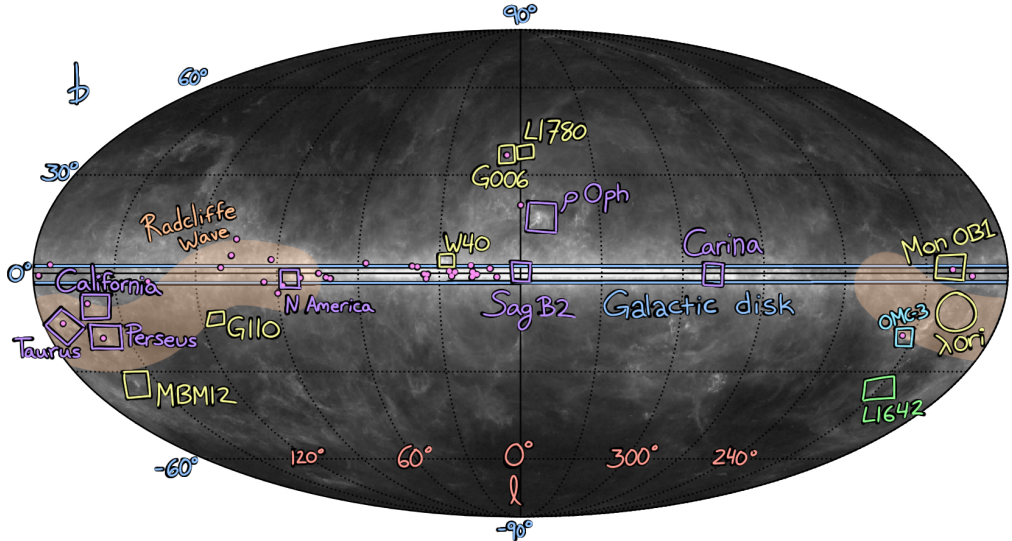


Figure 4.2: Distribution of molecular clouds within the Milky Way. Yellow labels correspond to clouds which are included in the B-FROST survey. The λ Orionis ring (PAPER-III) is located inside the yellow circle. OMC-3 from PAPER-II and PAPERV is marked in blue, L1642 (Juvela et al., 2020) in green, and the pink circles represent the sources in PAPER-I. Other important molecular clouds are drawn in purple. The blue horizontal lines show the extent of the Galactic disk ($\pm 2^\circ$ from the Galactic plane), and the orange curve shows the approximate extent of the Radcliffe wave.

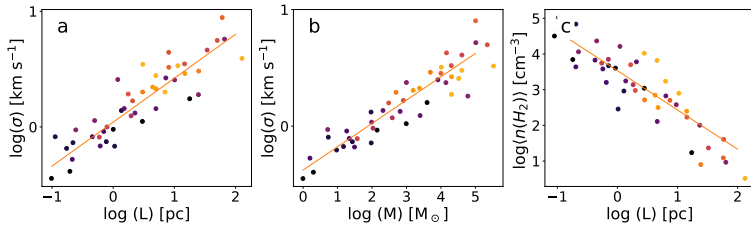


Figure 4.3: The Larson relations, showing a) cloud length against velocity dispersion b) mass against velocity dispersion c) size against density. Reproduced from Figs. 1, 3, and 5 of Larson (1981).

4.1 The properties of molecular clouds

4.1.1 Larson relations

In a study of multiple nearby interstellar clouds, Larson (1981) derived three well-known empirical laws.

$$\sigma \propto R^{0.5} \quad (4.1)$$

$$\rho \propto R^{-1} \quad (4.2)$$

$$\sigma \propto M^{0.25}, \quad (4.3)$$

where σ is the 3D velocity dispersion, R the radius of the cloud, ρ the density, and M is the mass.

The first law, relating cloud size to interstellar turbulence, suggests that molecular clouds are turbulent structures and turbulence occurs at all cloud length scales. The second law, correlating cloud size to its density, implies that the mass surface density Σ_{MC} does not significantly change between clouds and that smaller cloud complexes are more likely to be denser. The third law states that clouds in virial equilibrium are expected to have a positive correlation between mass and velocity dispersion. With a kinetic energy of $0.5M\sigma^2$ and a gravitational potential energy described by Eq. 2.1, a cloud in virial equilibrium (Sect. 5.1) is expected to have $\sigma \sim \frac{GM}{R}$ (Larson, 1981). These three equations are not independent, demonstrated in an expression relating the virial mass to the cloud mass (Heyer & Dame, 2015).

$$\sigma_v = \sqrt{(\pi G/5)R_{\text{MC}}\Sigma_{\text{MC}}} \quad (4.4)$$

More recent CO surveys have studied the applicability of these relations in various environments. Heyer & Dame (2015) plotted cloud radius against velocity dispersion

4.1. THE PROPERTIES OF MOLECULAR CLOUDS

from data collected from the Galactic center, the molecular ring, and the outer Galaxy (Dame et al., 1986; Solomon et al., 1987; Oka et al., 2001; Heyer et al., 2001). The clouds in the inner Galaxy best fit the Larson relations, however MCs in the Galactic center show significantly higher velocity distribution (five times larger) than theories predict (Shetty et al., 2012). In contrast, a relation between σ and size is not visible in the outer Galaxy due to the high scatter in velocity dispersion and the low range of sizes. Heyer & Dame (2015) suggest that this breakdown in Larson's relations is due to the assumption of constant surface density Σ for all clouds; observations suggest decreasing surface density with increasing Galactocentric radius. Although Falgarone et al. (2009) have extended this analysis to smaller clump sizes, they also note increased scatter in velocity dispersion at $R < 1$ pc.

4.1.2 Star formation rate and star formation efficiency

Star formation rate (SFR) describes the average mass of molecular gas converted to stars per year. The estimated SFR surface density in the solar neighborhood is $\Sigma_{SFR} = 1.7 \times 10^{-3} M_\odot \text{ yr}^{-1} \text{ kpc}^{-2}$ (Bovy, 2017; Sun et al., 2022). Star formation efficiency (SFE) describes the percentage of available molecular gas which is formed into stars. Based on studies of hundreds of MCs across ~ 100 galaxies, SFE per free-fall time (see below) $\epsilon_{\text{ff}} \approx 0.5^{+0.7}_{-0.3}\%$ (Schinnerer & Leroy, 2024), suggesting that SF is not an efficient process.

4.1.3 Timescales of star formation

Theoretical timescales for various processes set upper or lower bounds on certain phenomena.

Free-fall time

The time taken for a pressureless cloud or core to collapse into a protostar due to gravity alone gives a lower bound on how quickly a cloud can form stars. In reality, turbulence and magnetic fields can slow this collapse and the density of the cloud will change due to accretion. Free-fall time t_{ff} is

$$t_{\text{ff}} = \sqrt{\frac{3\pi}{32G\rho_0}}, \quad (4.5)$$

where G is the gravitational constant and ρ_0 is the average density of the cloud before collapse. As $t_{\text{ff}} \propto \rho_0^{-1/2}$, higher density regions should collapse faster. A

CHAPTER 4. MOLECULAR CLOUDS

sample of 80 external galaxies from the PHANGS-ALMA CO(J=2-1) survey shows mean $\langle t_{\text{ff}} \rangle \approx 11^{+5.5}_{-4.3}$ Myr (Sun et al., 2022; Schinnerer & Leroy, 2024).

Dispersion time

The dispersion timescale considers a cloud with mass much lower than its virial mass (Eq. 5.2), i.e. a cloud which will not collapse under its own gravity or form stars. Without external support, the cloud will disperse in

$$t_{\text{disp}} \approx \frac{R}{\sigma}, \quad (4.6)$$

where R is the radius of the cloud and σ the internal velocity dispersion (Ward-Thompson & Whitworth, 2011).

Depletion timescale

Though SF is not efficient, every generation of stars removes some matter from the ISM. The depletion timescale describes the time over which SF can continue given the current SFR and available gas supply, assuming no inflows or replenishment of matter. This value in nearby spiral galaxies is ~ 1 Gyr (Tacconi et al., 2013; Saintonge et al., 2013; Saintonge & Catinella, 2022), and is defined as

$$t_{\text{dep}} = \frac{M_{\text{gas}}}{\text{SFR}}, \quad (4.7)$$

where M_{gas} is the mass of the molecular gas reservoir. The depletion timescale of course neglects replenishment from the intergalactic medium, cooling of hot gas, and stellar ejecta.

4.1.4 Molecular cloud lifetimes

The mean cloud lifetime t_{MC} , i.e. the time during which a MC remains a coherent structure capable of creating protostars, has been a much debated topic for decades (Blitz & Shu, 1980; Ballesteros-Paredes & Hartmann, 2007; Heyer & Dame, 2015). A lower limit is set by the free-fall time (Eq. 4.5), which is ~ 2 Myr for a cloud with density $n = 250 \text{ cm}^{-3}$ (Heyer & Dame, 2015). Cloud lifetimes can be estimated using the distribution of H₂ with respect to the atomic and ionized gas components, the arm to interarm contrast, and the presence and age of YSOs within clouds (Heyer & Dame, 2015).

4.2. THE DIFFICULTY IN DETERMINING DISTANCE TO MOLECULAR CLOUDS

Arguments in support of long or intermediate-length cloud lifetimes, around 10^8 years, are based on the lack of MCs in interarm regions (Cohen et al., 1980). If GMCs are born from collisions of smaller MCs, the time required to build up mass would be even longer (Scoville & Hersh, 1979). Studies on the ages of clusters and newborn stars associated with molecular gas, in turn, seem to suggest shorter MC lifetimes ($t_{\text{MC}} \approx \tau_{\text{ff}}$). Elmegreen (2000) found that star cluster ages are similar to cloud crossing times in the Large Magellanic Cloud (LMC)¹, suggesting that SF is rapid. These findings are supported by Hartmann et al. (2001) and Ballesteros-Paredes & Hartmann (2007). Within the Solar neighborhood, most MCs are associated with stars of ages less than 3 Myr, whereas clusters with age over 5 Myr are usually not associated with CO emission. In addition, most MCs do not have a population of post-pre-main-sequence stars, suggesting that only one generation of SF occurs within MCs in the Solar neighborhood. Based on these more recent studies, it seems that SF begins soon after the formation of the MC, and the MC is quickly destroyed by feedback from massive young stars (Kim et al., 2022).

4.2 The difficulty in determining distance to molecular clouds

Many physical parameters of molecular clouds, such as mass, length scales, and thus gravitational stability, can only be calculated if the distance to the cloud is known. However, estimation of distances from observations is rarely trivial. Several methods exist, including kinematic distance and association of MCs to known structures, YSOs, or stars.

The kinematic distance method assumes a certain Galactic rotation curve such as that of Brand & Blitz (1993). Central radial velocities of clouds combined with the cloud's position in the sky are matched with this rotation curve to estimate the location of the cloud in 3D space. This method is uncertain as the velocity of interstellar gas is affected by outflows, supernovae, turbulence, and other processes. Furthermore, internal velocity dispersion and local velocity gradients such as infall motions can confuse the determination of position from velocity. However, as most Galactic molecular gas is located within GMCs (Heyer & Dame, 2015) which are generally better defined than more diffuse atomic clouds and have lower intracloud velocity dispersion, the distance ambiguity is lower than for atomic gas. A further issue arises for clouds within the Solar circle due to distance confusion: a certain

¹Our nearest neighbor, a bright irregular galaxy with high cold gas content and SFR, which is not actually a cloud.

CHAPTER 4. MOLECULAR CLOUDS

velocity will correspond to a near distance (lower than the distance to the Galactic center; 8.5 kpc) and a far distance (above 8.5 kpc). Kinematic distance calculations do attempt to compensate for local motions and distance confusion. This method was used to determine the distance to 27 fields in PAPER-I using TRAO ^{12}CO line observations.

If a MC is likely to be part of a well-known cloud structure, such as the Orion SF region, then the cloud can be assumed to have the distance of the structure. This method was used for many clumps in the PGCC catalog. In addition, many evolved (G)MCs are associated with young massive stars. Masers² (bright emission found in accretion disks and the outflows of massive YSOs) provide an excellent way to measure precise distance as the YSOs are still embedded in their natal cloud. Parallaxes with accuracy of $\sim 10''$ for ~ 100 masers have been measured using radio interferometry³ (Heyer & Dame, 2015). Accurate parallaxes have also been calculated for millions of stars and YSOs using Gaia data, and these (proto)stars can then be associated with MCs. Finally, due to its all-sky coverage and high precision, Gaia observations have been used to create high-resolution 3D extinction maps of the Galaxy. In PAPER-III and the B-FROST project we have used the cloud distances derived from Gaia data (Zucker et al., 2019).

4.3 Large-scale Galactic features

Through large-scale kinematic surveys and thanks to the high accuracy and coverage of Gaia data, structures spanning several kiloparsecs have been detected in the Galaxy. In addition to the spiral arms, these represent the largest scales of molecular gas structures within galaxies. Strongly elongated IRDCs, called bones, have been detected in the nearby Scutum-Centaurus arm at a distance of 3.1 kpc. At least 11 bone candidates exist in this region, with a mean length of $0.5 \pm 0.2^\circ$ (29.9 ± 14.2 pc), a mean width of $0.004 \pm 0.002^\circ$ (0.2 ± 0.1 pc), and a mean aspect ratio of 67.9 ± 37 (Goodman et al., 2014; Zucker et al., 2015). Seven large-scale, velocity-coherent Giant Molecular Filaments (GMFs) with mean lengths of $2.2 \pm 0.8^\circ$ (116.1 ± 60.4 pc) have been discovered near the Galactic plane. Those GMFs which are more closely associated with a spiral arm have a higher fraction of dense gas than those located in inter-arm regions (Ragan et al., 2014).

Several nearby MCs were thought to belong to an expanding ring of gas tilted 17° to the Galactic plane, named the Gould Belt (Herschel, 1847; Gould, 1874; Bobylev,

²Microwave Amplification by Stimulated Emission of Radiation

³as of 2015

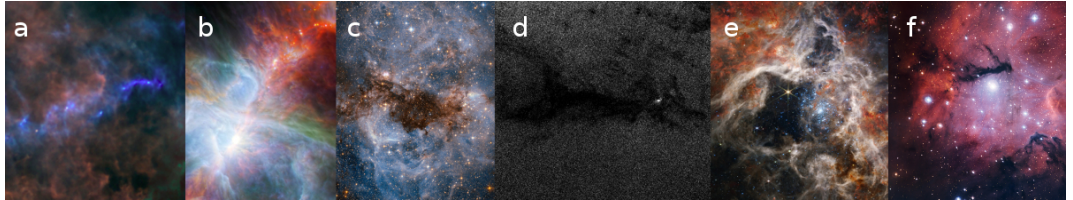


Figure 4.4: Examples of filaments in the Galaxy. (a): G82.65-2.00 with *Herschel* (b): Orion imaged with *Herschel* and Spitzer. (c): The H_{II} region N159 and Papillon Nebula in the LMC with Hubble. (d): A dark nebula in Orion using Gaia extinction. (e): The Tarantula Nebula (30 Doradus) in the LMC with JWST. (f): The Gum 15 SF region in Vela from the La Silla observatory in Chile.

Credits: (a) ESA/Herschel/SPIRE/M. Juvela (b) ESA/PACS/NASA/JPL-Caltech/IRAM. (c) ESA/Hubble/NASA. (d) A. Moitinho/M. Barros/C. Barata, U. of Lisbon, Portugal; H. Savietto, Fork Research, Portugal; ESA/Gaia/DPAC. (e) NASA, ESA, CSA, STScI, Webb ERO Production Team. (f) ESO.

2014). Later studies have discovered a velocity-coherent arrangement of gas which contains most clouds originally thought to belong to the Gould Belt, named the Radcliffe wave (Alves et al., 2020). This structure is around 2.7 kpc long with an aspect ratio of $\sim 20:1$ (Alves et al., 2020, labeled on Fig. 4.2).

4.4 Filaments

Dense gas in the ISM has been observed to form filamentary structures (Elmegreen & Elmegreen, 1979; Schneider & Elmegreen, 1979; Bally et al., 1987; Myers, 2009; Molinari et al., 2010; André et al., 2010; Men'shchikov et al., 2010), as shown in Fig. 4.4. Filamentary structure is also hierarchical and covers many scales: in a large sample of filaments observed with the *Herschel* SPIRE instrument, Schisano et al. (2014) found widths in the range 0.1-2.0 pc. Using higher-resolution interferometric molecular-line observations, Hacar et al. (2018) detected filaments with mean widths of only 0.035 pc in Orion. Compared to the 100-pc-scale bones, these illustrate the prevalence of filaments on all Galactic scales. Filaments are characterized by their aspect ratio, being many times longer than they are wide. However, they are often complex structures, driven by turbulence, magnetic fields, and local velocity gradients. Filaments are clearly fundamental to SF. Scientists have attempted to understand their formation and evolution using many assumptions and models.

4.4.1 The infinite cylinder theory of filaments

In the simplest model filaments can be modeled as infinite, self-gravitating cylinders. This theory was first presented by Stod  kiewicz (1963) and Ostriker (1964), who described their pressure (P) and density (ρ) by $P = C\rho^{1+1/n}$. Here C is a constant and the polytropic index $n = 0$ for a liquid, and $n = 1 \rightarrow \infty$ for an isothermal ideal gas. Within the ISM negative indices of $-3 \leq n \leq -0.3$ best fit observations (Toci & Galli, 2015; Tabatabaei et al., 2024). Both polytropic, and ideal self-gravitating cylinders have finite radii and masses per length. Mean density $\langle \rho \rangle$, the density profile as a function of radius r , $\rho_{\text{eq}}(r)$, and mass are described by

$$\langle \rho \rangle = \rho_0 \frac{1}{(1 + \frac{1}{8}\xi^2)^2} \quad (4.8)$$

$$\rho_{\text{eq}}(r) = \rho_0 \left[1 + \left(\frac{r}{H} \right)^2 \right]^{-2} \text{ where } H = \sqrt{\frac{2c_s^2}{\pi G \rho_0}} \quad (4.9)$$

$$M(\xi) = \frac{2k_B T}{G \mu m_H} \frac{1}{(1 + 8/\xi^2)}, \quad (4.10)$$

where ρ_0 is the density at the center of the cylinder and ξ is the distance from the center (Ostriker, 1964; Recchi et al., 2013). The critical mass per unit length is described by

$$\left(\frac{M}{L} \right)_{\text{crit}} = \frac{2k_B T}{G \mu m_H} = \frac{2\sigma_{\text{TH}}^2}{G}, \quad (4.11)$$

where k_B is the Boltzmann constant, T is the temperature, $\mu = 2.8$ is the mean molecular weight per free particle, m_H is the mass of a hydrogen atom, and G is the gravitational constant. The thermal velocity dispersion σ_{TH} is defined as:

$$\sigma_{\text{TH}} = \sqrt{\frac{k_B T_{\text{kin}}}{\mu m_H}}. \quad (4.12)$$

In filaments with mass greater than the critical line mass, self-gravity causes the filament to collapse.

4.4.2 Formation and fragmentation of filaments

Filaments can form through interstellar turbulence. Interacting shocks within an initially uniform medium can create regions of higher density when converging flows collide. If these regions become massive enough, i.e. if the local Jeans length (see

below) becomes smaller than the size of the fluctuation, these structures can begin to collapse (Klessen et al., 2004; Myers, 2009). Density fluctuations within MCs are generated due to supersonic turbulence, with self-gravity dominating the forces within the densest regions, in a process called gravoturbulent fragmentation (Klessen et al., 2004; Jappsen et al., 2005). Large-scale shocks dominate long-wavelength turbulence (Klessen et al., 2004) and these shocks can easily sweep up material, creating massive coherent structures. Due to this coherence, the internal velocity dispersion is smaller than in the turbulent flow, leading to clustered protostellar cores which are unstable against gravity and can thus lead to clustered SF.

According to simulations, even in regions of high magnetic energy which prevents turbulence, shocks are still formed by motions along the field lines. These shocks will then compress the gas by up to a factor of the square of the Mach number (Ostriker et al., 1999, 2001; Padoan et al., 2001; Larson, 2003). As Mach numbers in MCs are typically $\sim 5\text{--}10$, gas may be compressed by two orders of magnitude in density (Larson, 2003). Magnetic fields can also create filamentary structures when gas follows along magnetic instabilities (Nakamura & Li, 2008; Myers, 2009).

The Jeans length of filaments is given by (Larson, 1985; Hartmann, 2002)

$$\lambda_J = 3.94 \frac{c_s^2}{G\Sigma} = 1.5 T_{10} A_V^{-1} [\text{pc}], \quad (4.13)$$

where Σ is the corresponding surface density, c_s the sound speed, G the gravitational constant, and the second form of the equation uses $A_V[\text{mag}] = \Sigma/4.4 \times 10^{-3} \text{ g cm}^{-2}$ where T_{10} is the temperature in units of 10 K. The corresponding critical mass is thus

$$M_J = 24 T_{10}^2 A_V^{-1} M_\odot. \quad (4.14)$$

Using Larson (1985), Hartmann (2002) estimated a timescale for fragmentation of

$$t \sim 3.7 T_{10}^{1/2} A_V^{-1} [\text{Myr}], \quad (4.15)$$

Assuming a mean $A_V \sim 5^{\text{mag}}$, this corresponds to a Jeans length of $\lambda_J \sim 0.3 \text{ pc}$ and a collapse timescale of $t \sim 0.74 \text{ Myr}$ (Klessen et al., 2004). This corresponds well to, for example, the number of protostars detected in the Taurus filament contrasted with the mass and age of the filament (Hartmann, 2002).

4.4.3 Filament properties

As density increases inward, the dust temperature profile increases radially outward from filament center, most likely due to the external radiation field (Stepnik et al., 2003; Palmeirim et al., 2013; Recchi et al., 2013). Grain properties have also been observed to change within a filament (Stepnik et al., 2003).

The width of interstellar filaments

Assuming a cylindrical filament under hydrostatic equilibrium, the radial profile of a filament can be described by a Plummer function (Plummer, 1911; Nutter et al., 2008; Arzoumanian et al., 2011)

$$Y = N_0 \left(1.0 + \left(\frac{r}{R_{\text{flat}}} \right)^2 \right)^{0.5 - 0.5p}, \quad (4.16)$$

where N_0 describes the central column density of the filament, r the distance from the center of the filament, R_{flat} the width of the inner flat part of the Plummer curve, and p the slope of the filament, with a higher value of p describing a more centrally peaked filament. The resulting full-width at half-maximum ($FWHM$) of the Plummer function is

$$FWHM = 2|R| \sqrt{2^{2/(p-1)} - 1}, \quad (4.17)$$

and is more resistant to the degeneracy between R_{flat} and p .

A controversial topic in ISM studies has been the characteristic width of filaments. Already in early *Herschel* observations a common width of 0.1 pc was found within the low-mass clouds of the Gould belt (André et al., 2014). Analyzing multiple filaments in IC 5146, Aquila, and Polaris, Arzoumanian et al. (2011) found that regardless of central mass all the filaments show a central width of around 0.1 pc. Assuming a gas temperature of 10 K, the thermal Jeans width in this sample should instead range from 0.01-1 pc based on the sample of central column densities. Later studies have expanded this discovery to a wider sample of clouds also using other instruments (Juvela et al., 2012; Malinen et al., 2012; Palmeirim et al., 2013; Benedettini et al., 2015; Kirk et al., 2015; Kainulainen et al., 2016; André et al., 2016; Rivera-Ingraham et al., 2016). Possible reasons for this characteristic width include a change from supersonic to subsonic turbulence in gas (Padoan et al., 2001; Feder-rath, 2016) or the dissipation of magneto-hydrodynamic (MHD) waves (Hennebelle & André, 2013; Hennebelle, 2013).

However, recent papers, including PAPER-II, have called the universality of this width into question (Smith et al., 2014b; Panopoulou et al., 2017, 2022; Mannfors et al., 2025). For example, filament width has been found to be correlated with distance (Rivera-Ingraham et al., 2016; Panopoulou et al., 2022; Mannfors et al., 2025). This result can be seen in Fig. 4.5, where the relation between resolution of observations $HPBW$ ($HPBW \approx \text{distance} \times \text{angular resolution}$) and the filament $FWHM$ follows an approximately linear trend. Recent publications have suggested

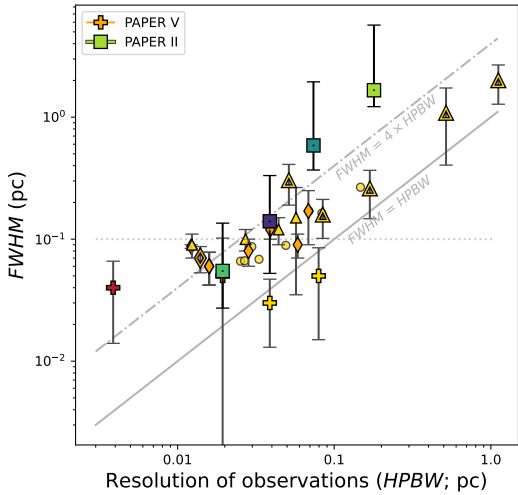


Figure 4.5: Resolution of observations ($HPBW$) compared to the mean derived width of filaments. The plot contains data from PAPER-II (squares) and PAPER-V (plusses). Also included are values from the literature: *Herschel* continuum observations (yellow triangles) from Palmeirim et al. (2013); Schisano et al. (2014); Zhang et al. (2020); André et al. (2022); Zhang et al. (2022); Li et al. (2023), and continuum observations using other telescopes (orange diamonds) from Hill et al. (2012); Salji et al. (2015); Federrath et al. (2016); Kainulainen et al. (2016); Howard et al. (2019); Zavagno et al. (2020); Schuller et al. (2021). Reproduced from Fig. 5 of PAPER-II.

that this distance-dependence is the result of beam convolution of a Plummer-like filament with an intrinsic $FWHM$ of 0.08–0.1 pc (André et al., 2022). Simulations from PAPER-II show that this is however not enough to explain the distance dependence. Instead, while convolution does affect filament widths, other causes include the worsening resolution at higher distances, with blending of wider, background structures into the main filament. In contrast, at small distances or with e.g. high-resolution ALMA observations, narrow fibers become visible (Hacar et al., 2018). The ISM thus has structure on many scales, and as filaments are not bodies with clearly-defined edges, the width of a filament strongly depends on both observations as well as on the fitting and analysis methods.

4.4.4 Filaments and magnetic fields

The orientation between magnetic fields and cloud structures is an often studied question. B-fields at cloud scales have been observed to be preferentially either aligned or perpendicular to parsec-scale B-fields (Zhang et al., 2014). All-sky Planck maps show that the magnetic field and gas structures are aligned at low column densities, but at $N(H_2) \geq 10^{21} \text{ cm}^{-2}$ the magnetic field and denser filaments are often perpendicular (Planck Collaboration et al., 2016b; Fissel et al., 2019). There is, however, large variation in the orientation between filaments and B-fields (Pattle

CHAPTER 4. MOLECULAR CLOUDS

et al., 2023). In the λ Orionis ring (PAPER-III), alignment between the B-field and filaments is poor. Rather, the filaments are aligned along the outflow direction of the central star. In the high-mass core G31.41, gas in outer core layers has been observed to collapse slower, guided by magnetic field lines, but closer to the core center collapse accelerates, breaking free of the magnetic field (Beltrán et al., 2024). It is possible that high-mass SF (HMSF) occurs in regions that are supercritical, whereas the environment of low-mass SF is at magnetic criticality, in other words, the magnetic fields in high-mass regions are less able to slow down gravitational collapse (Pattle et al., 2023). However, the high optical thickness of high-mass cores makes polarization observations of these dense regions difficult (Beltrán et al., 2024). In HMSF, magnetic fields seem to have more of an effect on cloud and filament formation, but at core and smaller scales the greater gravitational potential of high-mass cores overpowers the magnetic field (Beuther et al., 2025).

5 Clumps, cores, and star formation

While the process of SF is complex, the basic steps are fairly well-known. As illustrated in Fig. 5.1, SF begins when an interstellar filament (frame a) begins to fragment and compress (frame b), forming denser clumps and cores (frame c/d). Many forces act upon these structures. Gravitational force seeks to collapse a clump, whereas internal turbulence can eventually disperse it. Magnetic forces can either support a clump against gravity, or help direct the accretion. Finally, external pressure can further compress an otherwise insufficiently dense core.

If a clump is stable against gravity, it can eventually disperse back into the wider ISM. However, if a clump has sufficient mass, matter will continue accreting toward the center of the clump (frame e). Newborn stars, regardless of mass, have accretion disks which are formed due to conservation of angular momentum from large-scale inflows (Murillo et al., 2013; Tobin et al., 2015; Beltrán & de Wit, 2016; Andrews et al., 2018; Ahmadi et al., 2023; Tobin & Sheehan, 2024; Beuther et al., 2025). Streamers at scales down to a few thousand au (~ 0.005 pc) have been detected around YSOs using ALMA (Yen et al., 2014; Le Gouellec et al., 2019; Yen et al., 2019; Pineda et al., 2020; Valdivia-Mena et al., 2022). Similar streamers have been observed in high-mass regions (Peretto et al., 2014; Treviño-Morales et al., 2019, also the ATOMS survey). Density will increase until conditions are sufficient for nuclear fusion at $T \sim 10^6$ K (Reid & Hawley, 2006, frame f). Strong winds and radiation from the young star will begin to disperse the parent cloud but a circumstellar disk remains around the protostar (frame g).

Stars cannot form if densities are too low. A column density threshold for SF has been observed at $A_v \geq 2 - 8^{\text{mag}}$ (Kainulainen et al., 2009; Lada et al., 2010; Heiderman et al., 2010; Evans et al., 2014). Krumholz & McKee (2008) suggest a theoretical threshold for high-mass SF of $N(\text{H}_2) \sim 3 \times 10^{23} \text{ cm}^{-2}$ ($\rho \sim 1 \text{ g cm}^{-3}$, $A_v \sim 300^{\text{mag}}$), later studies empirically lower this to $\sim 5.4 \times 10^{22} \text{ cm}^{-2}$ ($A_v \approx 54^{\text{mag}}$; Kauffmann et al., 2010a,b; Kauffmann & Pillai, 2010; Beuther et al., 2025).

CHAPTER 5. CLUMPS, CORES, AND STAR FORMATION

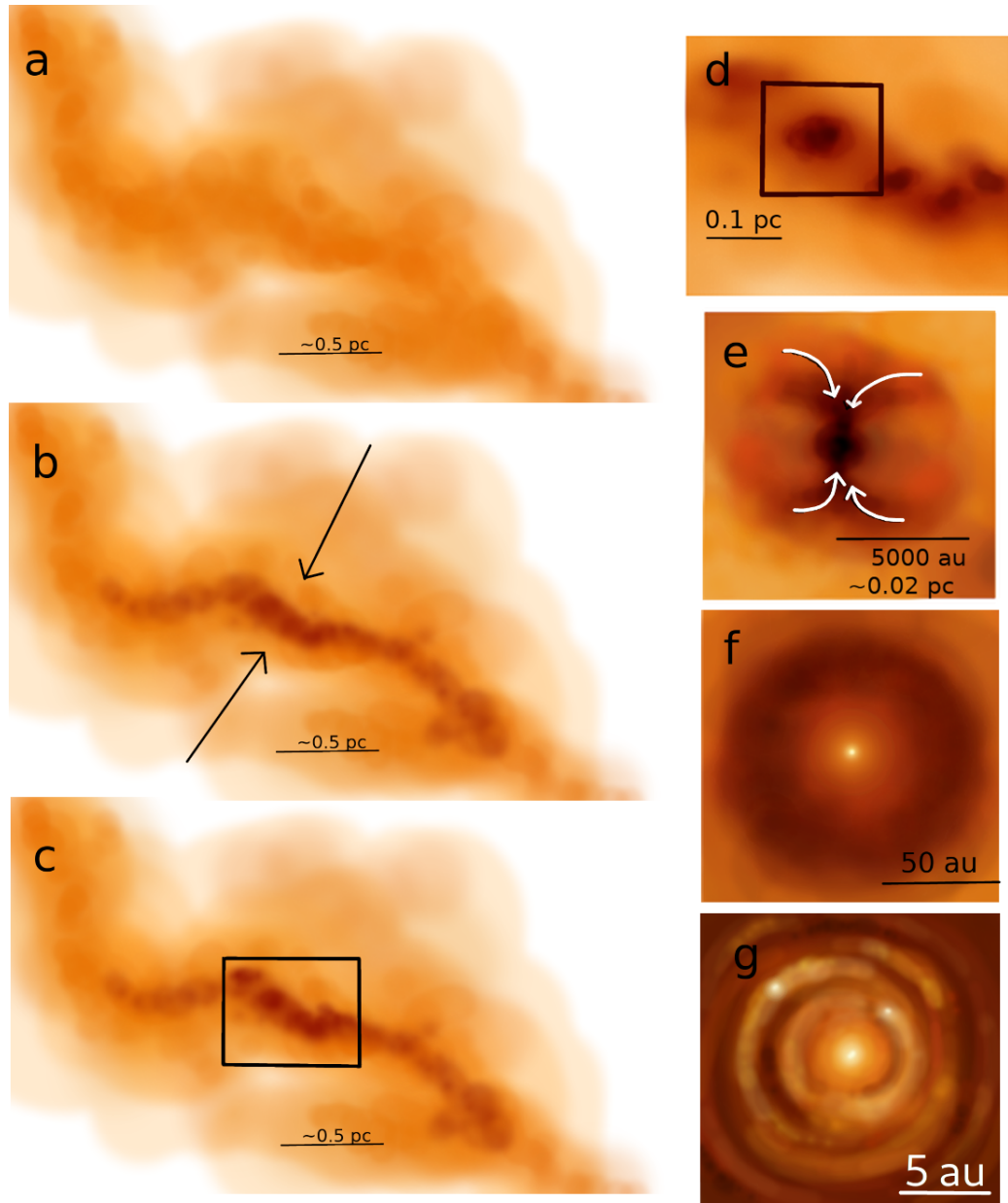


Figure 5.1: A diagram of the steps of star formation. (a) An interstellar filament. (b) Compression of the filament (c) Overdensities begin to form. (d) Clumps and cores. (e) Accretion onto a protostellar object. (f) The newborn star and its dusty envelope. (g) The young star and debris disk, with forming planets. Image by the author.

5.1 The virial theorem

An isolated cloud in equilibrium can be described by (e.g. Ward-Thompson & Whitworth, 2011)

$$\frac{1}{2}\ddot{\mathcal{I}} = \Omega_G + 2\mathcal{K} + \mathcal{M} + \mathcal{P}, \quad (5.1)$$

where $\ddot{\mathcal{I}}$ is the second time derivative of the moment of inertial \mathcal{I} , Ω_G the self-gravitational potential energy of the cloud, \mathcal{K} the internal kinetic energy of the cloud which results both from individual random thermal motions as well as bulk motions such as turbulence and rotation of the cloud, and \mathcal{M} and \mathcal{P} are the magnetic energy and external pressure on the cloud, respectively. If $\ddot{\mathcal{I}} < 0$, the total energy of the cloud is negative and the cloud will begin to collapse under its own gravity, if $\ddot{\mathcal{I}} = 0$ the cloud is in virial equilibrium.

5.1.1 Virial mass

Assuming a cloud in virial equilibrium, with mass M , radius R , and velocity dispersion σ , and neglecting external pressure and magnetism, kinetic and gravitational potential energy are

$$\begin{aligned} \mathcal{K} &= \frac{1}{2}M\sigma^2 \\ \Omega_G &\sim -\frac{GM^2}{R}, \end{aligned}$$

where G is the gravitational constant. As their sum must be equal to zero if the cloud is in equilibrium, the virial mass for a cloud can be determined

$$M_{\text{vir}} \sim \frac{\sigma^2 R}{G}. \quad (5.2)$$

Clouds with mass around the virial mass will be in virial equilibrium, and clouds with mass greater than the virial mass will collapse under gravity unless supported by other mechanisms such as magnetic fields. Likewise, a cloud with mass lower than the virial mass will likely disperse unless supported by e.g. external pressure. The virial parameter α_{vir} is used to estimate gravitational stability

$$\alpha_{\text{vir}} = M_{\text{vir}}/M_{\text{obs}}, \quad (5.3)$$

where M_{vir} and M_{obs} are the virial and observed masses, respectively. A cloud is generally said to be bound if $\alpha_{\text{vir}} \leq 1.0$ (Bresnahan et al., 2018). However, it is

very rare that all properties can be measured for a cloud. M_{vir} is often estimated using only internal turbulence and self-gravity. Bulk motion of gas has been shown to significantly skew estimates of virial parameter (Singh et al., 2021), and simulations show that estimating virial balance from CO-bright regions can result in artificially low α_{vir} (Szűcs et al., 2016). Conclusions about stability of clouds are always affected by the data and methods used. Using the catalog from PAPER-I, around 90% of all starless clumps are estimated to be virially bound; when adding estimates for external pressure around 94% are estimated to be bound. As with filament width, the resolution of observations also affects estimates of gravitational stability (see Sect. 5.4). Poor removal of background emission can also cause error in estimates of stability (Singh et al., 2021). Uncertainties in estimating α_{vir} are apparent in PAPER-III. We detect lower α_{vir} in larger structures, which are however not well-described by a spherically symmetric assumption. Furthermore, the dense cores within the λ Orionis East cloud do not appear gravitationally bound when considering CO velocity dispersion and mass despite the fact that protostars have been observed within several of these clumps (Yi et al., 2018; Saha et al., 2022).

5.2 Jeans criterion

The Jeans criterion (Jeans, 1902) is a theoretical framework which describes whether an isothermal, isotropic sphere of gas will collapse. For a gas with initial density ρ_0 and sound speed c_s , and where G is the gravitational constant, the Jeans length λ_J is described by

$$\lambda_J = \left(\frac{\pi}{G\rho_0} \right)^{1/2} c_s. \quad (5.4)$$

In this approximation, a sphere with radius less than λ_J will collapse due to gravity. The critical mass for gravitational collapse is given by Jeans mass, or the minimum mass required for a core to collapse due to gravity

$$M_J = \rho_0 \left(\frac{\lambda_J}{2} \right)^3 \propto T^{3/2} \rho_0^{-1/2}, \quad (5.5)$$

where the second part of the formula is derived with the definition of sound speed and the equation of state of an ideal gas. Thus, a certain density and temperature are required for gravitational collapse; an increase in temperature or decrease in density can halt this collapse. Jeans' criterion also does not include e.g. magnetic support.

5.3. THE INITIAL- AND CORE MASS FUNCTIONS (IMF AND CMF)

Assuming a temperature of 15 K and mean densities reported in the corresponding papers, Beuther et al. (2025) estimate mean Jeans lengths for low-, intermediate-, and high-mass regions (B213 in Taurus, IRDC 19175, and IRDC 18310-4; Tafalla & Hacar, 2015; Beuther & Henning, 2009; Beuther et al., 2015) of ~ 0.1 , 0.03 , and 0.02 pc, respectively. The observed separation of the structures corresponded well with the theoretical Jeans lengths, likewise in PAPER-II we also found that the mean clump separation in OMC-3 was similar to the Jeans length. This finding is not, however, universal: for example, minimum distance between clumps has been shown to decrease with evolutionary state of a cloud (Traficante et al., 2023). A stronger magnetic field has been shown to prevent fragmentation in simulations (Commerçon et al., 2011, 2022), and this correlation has been tentatively found in observations (Zhang et al., 2014; Palau et al., 2021) but cannot be said to have been confirmed (Beuther et al., 2024). Certainly fragmentation processes are not universal but depend on the local environment.

5.3 The initial- and core mass functions (IMF and CMF)

The initial mass function (IMF) describes the birth mass distribution of stars and the core mass function (CMF) the mass distribution of protostellar cores. Whether these two distributions are similar or not can support different theories of SF, and can give insight into the SFE of molecular clouds. The number \mathcal{N} of cores of mass M can be described as a power law with exponent Γ_{IMF} (Hennebelle & Grudić, 2024)

$$\frac{d\mathcal{N}}{d\log(M)} \propto M\mathcal{N} \propto M^{\Gamma_{\text{IMF}}}. \quad (5.6)$$

In most models, the IMF peaks at masses around $0.1\text{--}0.3 M_{\odot}$, meaning that low-mass stars are the most common stars to form. The canonical slope at high masses, the Salpeter slope, is $\alpha = 1 - \Gamma_{\text{IMF}} = 2.35$ (Salpeter, 1955).

Stars are formed from dense cores, therefore it is possible that the IMF is descended from the CMF. In the lower-mass cores of the nearby Pipe nebula ($d \sim 130$ pc), Alves et al. (2007) found that the CMF is similar in shape to the IMF in this region, but scaled to a higher mass by a factor of about three. In low-mass cores of the Aquila and Serpens main complexes, the slope of the CMF is also consistent with the IMF of the region (Fiorellino et al., 2021). However, in both the Galactic bar ($M_{\text{bar}} \sim 2 \times 10^4 M_{\odot}$, $d \sim 5.5$ kpc), and in a large sample of high-mass cores in protoclusters observed with the ALMA-IMF program ($M_{\text{cluster}} \sim 2.5\text{--}32.7 \times 10^3 M_{\odot}$,

CHAPTER 5. CLUMPS, CORES, AND STAR FORMATION

$d = 2 - 6 \text{ kpc}$), the CMF is relatively top-heavy and more flat than the canonical stellar IMF (Motte et al., 2018b; Louvet et al., 2024). Whether these complexes will create stars with a more top-heavy IMF or will evolve toward a Salpeter-like slope is unknown. These differences highlight the potentially different methods of high-mass SF when compared to low-mass SF.

5.4 Properties of clumps and cores

The properties of natal clumps affect the forming stars and can help distinguish between different SF theories. Studies of individual clumps and cores, as well as large-scale surveys, can help to understand trends in clump properties.

5.4.1 How to extract cores from the data

To estimate properties of cores one must first find them in the data. This is often done via an algorithm using some emission threshold below which structures are not considered to be sufficiently dense or coherent. However, both the chosen baseline emission as well as the method used for clump or core extraction can affect conclusions. As an example, by using three various clump extraction programs on the data in PAPER-I (GaussClumps, ClumpFind, and FellWalker; Stutzki (2014); Williams et al. (1994); Berry (2015), respectively) with the same baseline emission, the number of clumps detected varied from 529 to 785, with FellWalker detecting the lowest number of clumps. Likewise, in PAPER-II the number and type of cores found with FellWalker differed from those found with AstroDendro (Rosolowsky et al., 2008; Robitaille et al., 2019). Clearly, this difference in number of clumps would propagate to other properties. Furthermore, especially in continuum data, overlap of more diffuse structures along the line-of-sight can create structures that appear as dense clumps.

5.4.2 The shape of clumps

The density of star-forming clumps and cores as a function of distance from the center of the clump can be modeled as a powerlaw $\rho \sim r^{-p}$, with $p \sim 1 - 2$ in both low-mass (Motte & André, 2001) and high-mass SF regions (Palau et al., 2014; Wyrowski et al., 2016; Gieser et al., 2023); a similar index is found in OMC-3 in PAPER-II. Gieser et al. (2023) found that (on clump scales), the density profile of structures decreases from $p \sim 2.2 \rightarrow 1.2$ as the source evolves from a hot core to an UCH_{II} (ultra-compact H_{II}) region.

5.4. PROPERTIES OF CLUMPS AND CORES

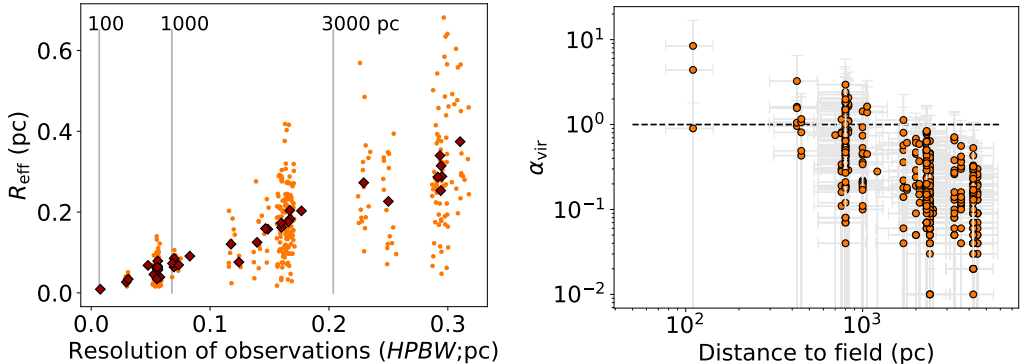


Figure 5.2: (left): Clump radius plotted against HPBW for the fields in PAPER-I; the corresponding distance in pc is labeled on the image. The diamonds mark the mean radius in each distance bin. (right): Virial parameter α_{vir} plotted against clump distance for the same data. The horizontal dashed line marks the limit of gravitational (in)stability. The error bars represent a 30% uncertainty on distance and 100% uncertainty on virial mass. Redrawn from PAPER-I.

Just as filament width has been observed to increase with lower HPBW , so has clump radius (Fig. 5.2, left). Similarly, the clumps in OMC-3 detected with the higher-resolution combined ArTéMiS and *Herschel* data have smaller radii than those detected with the lower-resolution *Herschel* data alone (PAPER-II). In PAPER-I, gravitational stability also seems to decrease with distance (Fig. 5.2, right). We have concluded that both of these findings relate more to observational limitations than to true clump properties; clumps and cores that are smaller or more diffuse are not detected at larger distances (or at lower resolution). As with filament width, the densest cores are not resolved but instead are blended with background clump structures. In the literature more distant clumps are also more likely to be gravitationally bound, with 20–60% of starless sources being bound within 500 pc of the Sun, but 80–100% being bound at distances of 1 kpc (Polychroni et al., 2013; Könyves et al., 2015; Elia et al., 2013). Certainly one could argue that more distant cores are likely to be within GMCs in the plane of the Galaxy and nearby cores are often high-latitude, low-mass cores. Disentangling physical properties from those based on observational constraints is difficult and illustrates the difficulty of analyzing even seemingly homogeneous catalog data.

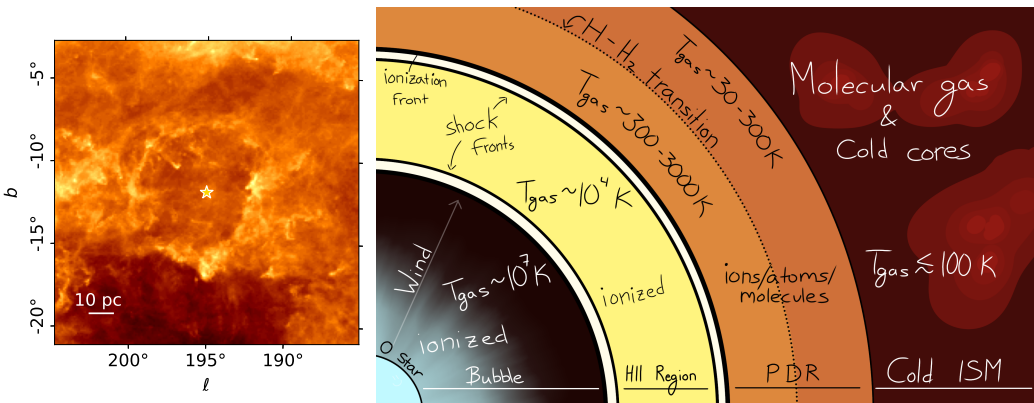


Figure 5.3: The effect of OB stars on their environment. (Left): Remains of a recent (1 Myr ago) supernova in Orion in a region also affected by ongoing feedback from the massive double star Meissa (marked with a white star). The supernova precursor was potentially another companion of Meissa. The current Meissa system contains two stars of spectral class O8III and B0Ve (Cutri et al., 2003; de Almeida et al., 2019). The image shows the cold dust emission observed with the *Planck* satellite at $850\mu\text{m}$. (Right): Schematic of an H_{II} region around an O-class star, redrawn from Haworth et al. (2018).

5.5 High-mass star formation (HMSF)

HMSF is harder to observe and model than low-mass SF, and is therefore far less understood. However, high-mass stars play a crucial role in the evolution of galaxies through feedback and supernovae (SNe). A star is classified as high-mass if it is of spectral class B3 or earlier, has luminosity $L > 10^3 L_\odot$ and stellar mass $M \geq 8 M_\odot$ (Motte et al., 2018a)¹. High-mass stars have almost no pre-main-sequence phase; instead they will begin to fuse hydrogen before accretion has ended (Palla & Stahler, 1993). Thus, even before birth, high-mass stars have a strong effect on their environment. UV radiation from OB stars heats and ionizes the surrounding gas, creating an H_{II} region which expands through the cloud (Fig. 5.3, left).

High-mass stars almost universally form in clustered environments (Beuther et al., 2007; Zinnecker & Yorke, 2007; Motte et al., 2018a; Beuther et al., 2025). In contrast, low-mass stars can form in a larger variety of environments, including isolated high-latitude clouds but also alongside high-mass stars (Beuther et al., 2025). The rate of

¹High-mass stars are also known as OB stars.

multiplicity, or the percentage of stars with stellar companions, varies strongly with stellar mass. In O-class, solar-type, and M-dwarf stars, multiplicity is $(91 \pm 3)\%$, $(46 \pm 2)\%$, and $(26.8 \pm 1.4)\%$, respectively (Sana et al., 2014; Raghavan et al., 2010; Winters et al., 2019). While some massive field stars are known, it is possible that most of these stars have formed in clusters and have been ejected. de Wit et al. (2005) have observed 43 massive O-type field stars, concluding that only $(4 \pm 2)\%$ of high-mass field stars could have been formed in an isolated environment.

In their review of HMSC, Zinnecker & Yorke (2007) detail the evolutionary steps of a high-mass core:

- IRDCs: potentially the initial stage of HMSC, IRDCs are high-mass clouds which do not show signs of active SF but may contain dense cores which will form stars. Lower-mass cores will likely form alongside high-mass stars.
- Hot molecular cores: Dense cores that are already being heated by SF, at $T \sim 300\text{ K}$ and sizes of 0.05 pc (10^4 au ; Herbst & van Dishoeck, 2009). Hot cores have complex chemistry, including COMs and maser emission.
- Hypercompact and ultracompact H_{II} (UCH_{II}) regions: Due to UV radiation from the formed central star, gas around the star is ionized. These UCH_{II} regions will increase in size due to constant radiation pressure, expanding through the molecular cloud.
- Compact and classical H_{II} regions: The H_{II} region expands hydrodynamically, blowing away clouds and halting SF.

5.6 Feedback

Feedback covers the processes with which stars affect their environment. Like high-mass YSOs, low-mass YSOs also radiatively heat their environment and can form jets and outflows (Beuther et al., 2025). In addition to these processes, feedback from high-mass stars includes photoionization and the creation of H_{II} regions, UV radiation that causes stellar winds, and supernovae (Beuther et al., 2025).

Strong feedback from newborn stars exerts radiative pressure on matter which is being accreted onto the YSO (Kee & Kuiper, 2019). As higher-mass stars have more energetic outflows, this sets an upper limit on mass of $20\text{-}40\text{ }M_{\odot}$ assuming isotropic infall and up to $150\text{ }M_{\odot}$ if infall is anisotropic (Larson & Starrfield, 1971; Kahn, 1974; Yorke & Kruegel, 1977; Nakano, 1989; Krumholz et al., 2005a; Zinnecker & Yorke, 2007). At larger scales, stellar winds can disperse gas and end accretion

CHAPTER 5. CLUMPS, CORES, AND STAR FORMATION

onto the star-disk system (Rosen, 2022). While feedback from H_{MSF} eventually destroys clouds, expanding H_{II} regions have also been observed to cause further generations of SF when gas at the edge of the region is compressed at the shock fronts (labeled on Fig. 5.3, right; Kendrew et al., 2016; Palmeirim et al., 2017). We detect compression of gas and the formation of dense cores also at the edge of the λ Orionis ring in PAPER-III.

The molecular cloud environment around an O-star is illustrated in Fig. 5.3 (right). The O-star is surrounded by a wind-blown bubble filled with hot, ionized gas. This bubble is surrounded by the H_{II} region and a photon-dominated region (PDR). Nearer to the star, gas in the PDR is primarily atomic but at a temperature around 300 K the gas becomes molecular. Far from the effects of ionizing radiation and shielded by the gas of the PDR, gas is fully molecular and dust species form.

Stars with mass over $8 M_{\odot}$ end their lives in a supernova. SNe are some of the most energetic processes in space, injecting into their environment thousands of times the Sun's entire energy output in a few seconds. As OB stars live for very short lives, at this point they are generally still embedded in the remnants of their parental cloud. This massive injection of energy will ionize the environment, completely destroying the cloud. Due to their energy, SNe can eject cold gas from the galactic disk and even from the potential well of a galaxy. In lower-mass galaxies such as small irregular galaxies, a few SNe can potentially end all SF. The λ Orionis ring (Fig. 5.3, left) is an excellent example of a region affected by feedback from the double star Meissa but which has been created by a supernova some Myr ago (Cunha & Smith, 1996; Dolan & Mathieu, 2002). The gas at the rim of the ring has been compressed, leading to cold CO-bright filamentary clouds shaped by the strong stellar winds of Meissa.

Figure 5.4 shows feedback processes relative to the age of a high-mass star, with zero-age main sequence (ZAMS) being the time after the star entered the Main Sequence. Ionization, luminosity, and stellar winds affect a star already before birth, with SNe starting at around 3 Myr for the highest-mass stars. While ionizing radiation and stellar winds are no longer relevant after a star's death, the luminosity from the supernova remnant and potentially remaining neutron star or black hole will continue to affect their environment (Schinnerer & Leroy, 2024).

5.7 Theories of star formation

Due to the relative rarity of high-mass stars, as well as their rapid birth, multiple theories around H_{MSF} exist. Some of the most widely-proposed formation methods are presented below.

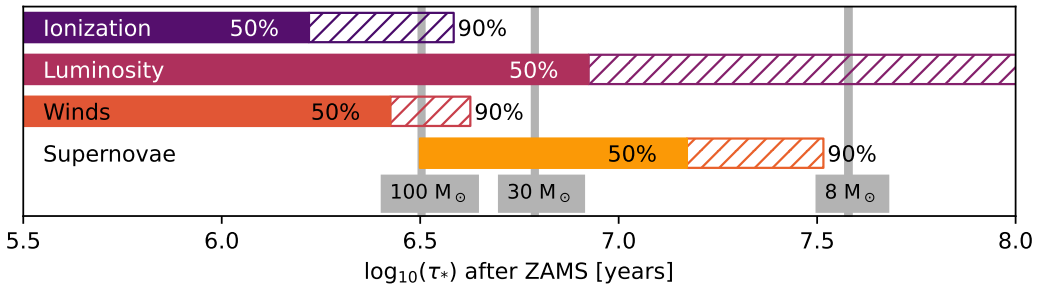


Figure 5.4: The timescales during which certain feedback processes are relevant. Redrawn from Schinnerer & Leroy (2024). The filled and hatched regions show the times at which 50% and 90% of the total emission occurs. The approximate time of supernovae for stars of different mass is shown on the bottom in the gray boxes. ZAMS stands for the zero-age main sequence.

5.7.1 Monolithic core collapse

It is possible that high-mass stars form in the same way as their low-mass counterparts. In this model, a core collapses under self-gravity without further fragmentation, forming one protostar (McKee & Tan, 2003). The majority of the mass of the star would be gained through the collapse as opposed to accretion, and thus stellar mass should directly correlate with core mass (McKee & Tan, 2003; Krumholz et al., 2005b; Alves et al., 2007). Assuming this theory, the IMF should resemble the CMF. Furthermore, isolated high-mass stars should be common, but as stated in Sect. 5.5 this is not supported by current observations. While a few high-mass stars could be born in this way, it is not likely to be the primary formation mechanism of high-mass stars. In their simulations, Padoan et al. (2020) find that the star formation timescale is comparable to the turbulence turnover time, but much larger than the freefall time, making monolithic core collapse theories unlikely.

5.7.2 Competitive accretion

The major competing theory to monolithic core collapse is the theory of competitive accretion, which proposes that a large gas cloud fragments into multiple equally-sized cores. The protostars forming inside these cores all accrete matter via Bondi-Hoyle accretion from the same reservoir, competing to grow larger than neighboring YSOs (Zinnecker, 1982; Bonnell et al., 2001). In contrast to the previous model, a significant portion of a star's mass would thus be gathered during post-formation accretion as

CHAPTER 5. CLUMPS, CORES, AND STAR FORMATION

opposed to the initial gravitational collapse (Krumholz et al., 2005b). Stellar mass would be related to local gas density so this theory would result in mass segregation, with more massive stars being found at the centers of clusters.

Supporting this theory is the observation that protostars at the centers of clusters are generally higher-mass than those at the edges (Hillenbrand & Hartmann, 1998; Bonnell et al., 2001). As the ages of the clusters are not sufficient to allow for two-body relaxation to have caused this mass segregation, this segregation likely occurs during the process of SF (Bonnell & Davies, 1998). However, simulations by Parker et al. (2024) show that stars which form through competitive accretion reside in regions with the deepest potential wells only in simulations without stellar feedback. In simulations with feedback, in only 60% of simulations are the highest-mass stars found in the deepest potential wells. Certainly the rate of clustered HMSC suggests that stars usually form together.

5.7.3 Global hierarchical collapse

This theory suggests that molecular clouds, on all scales from full MCs down to dense cores, are in a state of gravitational collapse (Vázquez-Semadeni et al., 2019). Gas accretes onto smaller structures from gas reservoirs in larger structures. As the more diffuse, warm medium begins to contract, its temperature also decreases. This increases density by a similar factor, causing a significant decrease in Jeans mass. As a cloud cools, its molecular content (as opposed to atomic gas) increases. As long as the gas remains isothermal, collapse enhances anisotropies present in the parent cloud as collapse is faster along the shortest dimensions of the cloud. Gas accretes onto filaments in a perpendicular direction, but then flows along the filaments toward dense cores or hubs.

If all clouds collapsed in free-fall time, the rate of SF predicted by this theory would be significantly higher than that which is observed. Instead, the collapse proceeds with scale: smaller (core-scale) structures exceed their Jeans mass in a faster timescale than large structures and the initial SFR of a cloud will be lower than that of a similar, older cloud. Acceleration of SF increases until the creation of protostars with mass high enough to disrupt the parent cloud through feedback.

5.7.4 Inertial-inflow

The inertial-inflow model (Padoan et al., 2020) describes SF as a combination of processes at three scales. In the inertial inflow phase, gas flows along filaments to the protostellar envelope at scales of 1-10 pc. These inflows arise naturally through

supersonic turbulence, and generally have kinetic energy larger than thermal or gravitational energy. As a core collapses, large-scale filaments may continue accreting matter onto the core. The inflow region is turbulent and dominated by random motions.

At the infall phase, at scales of 0.01-0.1 pc, self-gravity of the structures exceeds turbulent kinetic energy. Motion becomes uniform, with matter flowing from the envelope to the disk.

At the smallest scales of 100-1000 au, matter is accreted onto the protostar from the circumstellar disk. In this model, the SF timescales and accretion rate are determined by the turbulence, not the gravity of the core or protostar. The mass of the star is not determined by the core mass due to accretion from the surrounding medium through filamentary inflow. This refutes the need for the CMF to resemble the IMF in observations of high-mass SF regions. Further, this theory differs from the competitive accretion model as in this model the accretion rate is determined by large- (parsec)-scale inflow as opposed to the gravity of the forming protostar.

5.8 YSO classes

No matter how they have formed, low-mass YSOs can be divided into several classes based on the shape of their MIR spectra, illustrated in Fig. 5.5. This classification is not applicable to high-mass stars due to their rapid formation timescales (Robitaille et al., 2006). Lada (1987) presented the classification of YSOs into three categories of increasing age: I, II, and III based on these targets' spectral energy distributions. Using wavelengths in the range 2-20 μm , the spectral index a can be calculated based on the observed flux F

$$a = \frac{d \log(\lambda F_\lambda)}{d \log(\lambda)} \quad (5.7)$$

Class I sources have significant IR excess at longer wavelengths above 2 μm , with a spectral index $0 < a \leq 3$. Class II sources also have significant MIR and FIR emission but with a flat or decreasing distribution above 2 μm , and a spectral index of $-2 \leq a \leq 0$. Class III sources have only a slight MIR excess and a spectral index of $-3 < a \leq -2$. Andre et al. (1993) added a fourth classification of Class 0 protostars. These sources are deeply embedded in their parent clouds, thus are undetected in the NIR ($\lambda < 10 \mu\text{m}$) and have SEDs resembling that of a single-temperature blackbody. A further classification of flat-spectrum sources have a spectral index $-0.3 < a < 0.3$ (Greene et al., 1994; Kang et al., 2017). Though in general class correlates with the age of a YSO, the viewing angle of the YSO can affect the shape of its observed

CHAPTER 5. CLUMPS, CORES, AND STAR FORMATION

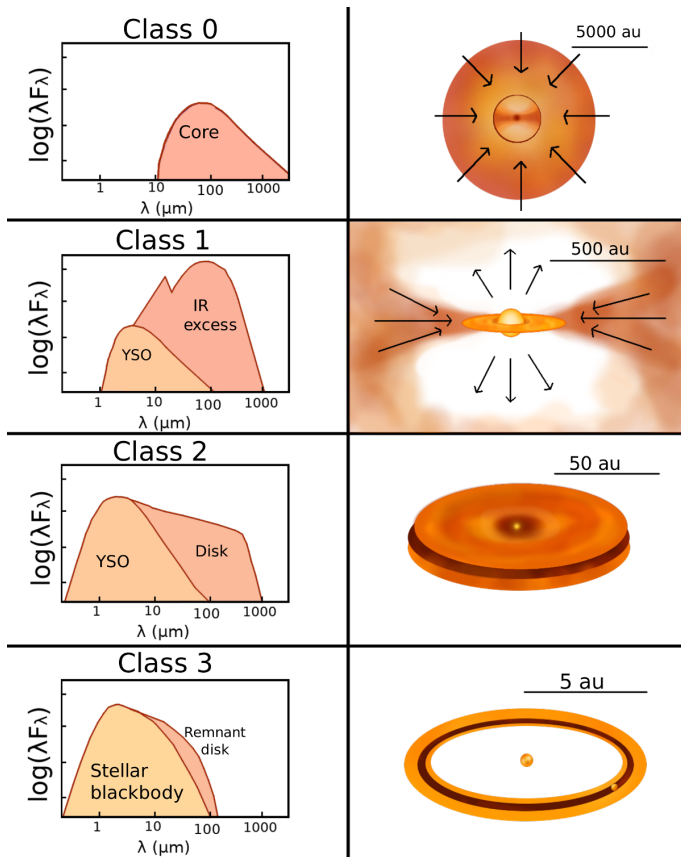


Figure 5.5: Typical spectra and morphology of YSO classes 0-III. Image by the author, based on Maddison (2017); Vogel (2019). The arrows show direction of gas flows.

spectrum. As an example, an edge-on embedded protostar can appear to be of a later class if its flux is dominated by scattered light; the effect of viewing angle is stronger if a narrow range of wavelengths are used to estimate the shape of the SED (Robitaille et al., 2006).

6 Summary of the publications

The thesis consists of 5 journal publications:

- **Paper I:** Mannfors, E., et al., *Characterization of dense Planck clumps observed with Herschel and SCUBA-2*, A& A, (2021) vol. 654. pp. A123
- **Paper II:** Mannfors, E., et al., *Comparison of Herschel and ArTéMiS observations of massive filaments*, A& A, (2025) vol. 695. pp. A242
- **Paper III:** Mannfors, E., et al., *B-FROST: B-Fields and star formation across Scales with TRAO III: The high-energy λ Orionis ring*, submitted
- **Paper IV:** Juvela, M., Mannfors, E., Liu, T., & Tóth, L. V., *Synthetic Next Generation Very Large Array line observations of a massive star-forming cloud*, A& A, (2022) vol. 666. pp. A74
- **Paper V:** Juvela, M., & Mannfors, E., *Filaments in the OMC-3 cloud and uncertainties in estimates of filament profiles*, A& A, (2023) vol. 671. pp. A111

The papers are summarized below. The author's contribution to the papers is described at the end of each section. The full publications, including all appendices, are available in color at the references above and on ArXiv. PAPER-III will also be published in open access.

6.1 Paper I

In this paper we analyzed a sample of 53 fields which were observed with the JCMT SCUBA-2 instrument as part of the TOP-SCOPE project. Using ancillary *Herschel* observations of these fields, we performed MBB fitting to determine column densities and temperatures. We detected dense clumps in the SCUBA-2 data, and categorized them as starless, prestellar, or protostellar based on association of YSOs from catalogs

CHAPTER 6. SUMMARY OF THE PUBLICATIONS

as well as virial analysis using estimates of internal turbulence from TRAO line data. We also calculated kinematic distances for 27 PGCC fields without previous distance estimates.

Analyzing global dust properties for our sample we detected $\langle \beta \rangle \approx 1.7\text{--}1.9$, $\langle N(\text{H}_2) \rangle \approx (1\text{--}3) \times 10^{21} \text{ cm}^{-2}$, and $\langle T \rangle \approx 16\text{--}23 \text{ K}$. These values are in good agreement with those found in the dense ISM. The inclusion of $160 \mu\text{m}$ data into the MBB fit increases temperature and lowers β and $N(\text{H}_2)$ whereas the inclusion of $850 \mu\text{m}$ data does not significantly affect derived β . We detect a strong temperature- β anti-correlation in both the full field and for the values of individual clumps.

This paper resulted in a catalog of 529 dense clumps found in a variety of Galactic environments. The derived properties of the clumps show them to be cold, dense structures ($\langle T \rangle \approx 10\text{--}25 \text{ K}$; $\langle N(\text{H}_2) \rangle \approx 10^{22} \text{ cm}^{-2}$). While clump temperature does not differ between clump categories, we found that starless clumps are significantly more diffuse than prestellar or protostellar clumps. Such a large catalog is excellent for analyzing trends in clump properties as a function of distance or local environment. As distance to the field increases, we detected a larger percentage of large, high-density clumps with higher temperatures. Thus, α_{vir} also seems to decrease with distance and a higher percentage of distant clumps appear gravitationally bound. This is however interpreted to result from lower spatial resolution at higher distances. Correlation is also found between properties and location in the Galactic plane. Fields that are closer to the Galactic plane were found to be more complex with a larger number of clumps. We also detected higher column density in the central Galaxy as compared to the Galactic anticenter, as well as higher temperature in the Galactic plane.

Author's contribution: The SCUBA-2 data were provided by the SCOPE project and TRAO molecular line data by T. Liu. EM did most of the analysis, including kinematic distance estimation, convolution and reprojection of data, MBB fitting (adapting a code written by MJ), clump detection and calculating of clump properties, finding ancillary data including YSO catalogs and analyzing said data, and gravitational stability analysis. EM wrote the paper (with the exception of section 4.4.), with significant comments and input from MJ and the other coauthors. EM created the images and the final catalog. EM was responsible for the publishing and referee process.

6.2 Paper II

A dense filament in the OMC-3 cloud was observed with the APEX ArTéMiS instrument. We combined *Herschel* data with the ArTéMiS observations to analyze this filament. We estimated dust properties with MBB fitting, performed Plummer fitting of the filament, and compared high- (\mathcal{C} ; combined ArTéMiS+ *Herschel* with $FWHM \sim 10''$) and low- (\mathcal{H} ; *Herschel* alone with $FWHM \sim 20''$) resolution data of the same field to understand the effect of limited telescope resolution on our results, most notably the controversial 0.1 pc filament width. We further include *Herschel* data of two other fields at a resolution of $\sim 20''$ for a larger sample of filament profiles.

The filaments studied have mean $N(H_2) \sim 10^{22} \text{ cm}^{-2}$, with column densities in OMC-3 extending to 10^{23} cm^{-2} in the densest regions. Temperatures are somewhat higher than for the catalog in PAPER-I, at $\sim 21\text{-}25$ K. Line masses are of the order $100\text{-}300 M_\odot \text{ pc}^{-1}$. Virial line masses calculated with internal gravity and nonthermal turbulence suggest that all the filaments are in a state of global gravitational collapse. We compared the low-resolution \mathcal{H} maps and the high-resolution \mathcal{C} maps. The \mathcal{C} data reach higher column densities and derived masses than the \mathcal{H} maps. Fragmentation at smaller scales is detected in the \mathcal{C} data.

The most controversial finding of this paper is the difference in filament width detected between \mathcal{C} and \mathcal{H} . While at the *Herschel* resolution we observe mean filament widths consistent with the canonical width of 0.1 pc, at the ArTéMiS resolution derived widths are only ~ 0.05 pc. We further detected a correlation between resolution of observations *HPBW* and the derived $FWHM$ of each filament profile, consistent also with results from the literature. We tested the effect of observational parameters and form of Plummer function used on derived properties. In general, higher-intensity filament profiles were more robust against sources of error. We detected a correlation between resolution and $FWHM$ also in our simulated filaments.

Author's contribution: The ArTéMiS data were provided by MJ. The data calibration of OMC-3 was performed by MJ, but checked by EM. EM extracted ancillary data from the archives. EM did much of the analysis, including feathering (combination) of the *Herschel* and ArTéMiS data, filament extraction and alignment (adapting scripts originally created by MJ), MBB analysis (adapting the script as in PAPER-I), Plummer fitting and analysis, dense clump detection, fragmentation analysis, and much of the simulations in the appendices. MJ originally wrote the code for 2D Plummer convolution, which EM adapted in Section A.5. EM created the images and tables, and wrote the paper, with comments and input from the coauthors including significant input from MJ. EM was responsible for the publishing and referee process.

6.3 Paper III

Paper III is part of the B-FROST project, and so some of the analysis used in this paper were done originally for the first B-FROST paper (B-FROST I). PAPER-III focuses on two fields (East and South; E and S) in the high-energy ring λ Orionis. We further perform some analysis on West (W), but due to issues during observations were not able to fully study the field. We used ^{12}CO and ^{13}CO molecular line data, combined with ancillary *Planck* column density and polarization data, *Herschel* SPIRE data for E, as well as clump and YSO catalogs to understand how the bright OB star Meissa affects dense gas.

We calculated H_2 and CO column densities, as well as X-factors and $[\text{CO}/\text{H}_2]$ abundances, for E and S. Column densities at the TRAO resolution ($48''$) are of the order 10^{21} cm^{-2} and an order of magnitude lower at *Planck* resolution ($5'$). X(^{12}CO) is slightly higher than the mean X-factor for the Galaxy but abundance is an order of magnitude lower than that detected in e.g. Orion B and Taurus. In abundance we detected CO depletion in several dense cores and the central filament in E. λ Orionis shows many signatures of being a high-energy environment. The behavior of gas at the Meissa-facing edge of the cloud is completely different to that of the shielded back edge: the transitions between atomic gas $\rightarrow \text{H}_2$ and atomic C $\rightarrow \text{H}_2$ and CO are not resolved at the TRAO resolution (corresponding to $\sim 0.1 \text{ pc}$ at a distance of 400 pc) in the irradiated edge. In contrast, in the shielded region of the cloud the transition from atomic carbon to CO occurs much deeper inside the cloud than the transition from H to H_2 . In the irradiated edge the extent of ^{12}CO and ^{13}CO are nearly equal, unlike what is expected for CO in the dense ISM. High-energy feedback from Meissa irradiates and compresses gas at the head of the λ Orionis clouds and will likely disperse much of the cloud in the future. Nonetheless, several dense cores, including protostellar cores, are visible both in our data and in previous surveys.

Polarization fraction p is around 4-7% in the region, with $N(\text{H}_2)$ being anticorrelated with p . We use the filament-finding algorithm FilDReaMS and the histogram of relative orientations (HRO) method to study B-field and filament alignment in the λ Orionis clouds. Filaments are more perpendicular to the B-field at low CO integrated intensity $W(^{12}\text{CO})$ and more parallel at high $W(^{12}\text{CO})$, but the correlation between B-field and filament position angle is weak. For example, the long axis of the λ Orionis E cloud is aligned with the direction of radiation from Meissa, but is tilted $\sim 45^\circ$ from the B-field. We conclude that stellar feedback is dominant over the B-field in the λ Orionis ring. This paper will facilitate comparison to other B-FROST fields in future papers.

Author's contribution: EM contributed significantly to the observations for

the B-FROST project. For all the B-FROST data EM created the moment maps, extracted Planck data from the archives (polarization, dust properties), extracted *Herschel* data, performed MBB calculations, and contributed to the writing of the first B-FROST paper. For PAPER-III specifically, EM was responsible for much of the analysis, including creating and analyzing dendrograms, finding ancillary clump and YSO data, creation of X-factor and abundance maps, and analysis of the data. EM was responsible for the writing of the paper, and most pictures and tables, with significant contribution from the coauthors (especially JV and JM). JO performed the FilDReaMS analysis and created Figs. C.1-C.3. EM wrote these sections with input from JO. EM is responsible for the publishing and referee process.

6.4 Paper IV

PAPER IV was part of the planning stages for the ngVLA interferometer. We used magnetohydrodynamic simulations of a GMC, focusing on a filamentary structure that resembles an IRDC. This selection contains around 230 already-formed YSOs and is composed of two separate clouds connected by a thin bridge in 3D space. In the 2D observations, these structures fall partly along the same LOS. We performed RT modeling of the region, including emission from the YSOs and line modeling of multiple dense gas tracers but without depletion in dense cores. We then created synthetic observations of the region using the CASA simulator in the Core Subarray (94 antennae, baseline ≤ 1.3 km). We then added observational noise and performed reduction of these observations as would be done for real interferometric data. We compared the synthetic observations to the true parameters extracted from the 3D model cloud.

Large-scale structure is lost during reduction of the interferometric observations. We also detected areas of negative intensity around the filament. At small scales and high column densities, the correspondence between the ideal and simulated observations is good, but column density estimates are less accurate at lower densities. Additional sources of error come from the assumption of a single velocity component along the LOS. In general, we find multiple sources of error in observations. Nonetheless, at core scales the data loss from filtering is not significant. If one wishes to study the larger-scale environment of a filament, single-dish data are still needed. We created simulated single-dish data of the $\text{N}_2\text{H}^+(1-0)$ line at a resolution of $8.1''$, corresponding to a 100-m dish. These data were combined with the interferometric data in the same way as in PAPER-II. In regions outside the densest cores, we found that single-dish data are crucial to recovering the structure of MCs.

CHAPTER 6. SUMMARY OF THE PUBLICATIONS

Author’s contribution: EM created the single-dish simulated observations and combined them with the interferometric data. EM provided feedback, and wrote the first draft (including the original illustrations) of the single-dish section.

6.5 Paper V

PAPER V was a companion paper to PAPER II. Using similar methods, we analyzed filament properties using continuum and Spitzer extinction data. Instead of the one major filament, we utilized four of the densest filament segments in the data for this paper. Simulations of the effect of a bright point source on filament widths were presented. Unlike in PAPER-II, we did not find a significant difference in filament widths between ArTéMiS, *Herschel*, and extinction data. This is not due to different Plummer fitting scripts, but rather a difference between the brightest filament segments in PAPER-V and the full filament in PAPER-II.

Author’s contribution: PAPER-II and PAPER-V were created using many of the same methods and data. While MJ performed the published Plummer fitting on the selected filament segments, EM tested the fit with their own fitting code. MJ also tested the fits in PAPER-II with his own code; both of these tests led to the same results as those published. EM provided feedback and comments on the paper.

7 Concluding remarks

The processes of SF and the evolution of the ISM are complex. Beyond the scope of this thesis, phenomena at intergalactic scales can enrich the gas of galaxies, and certainly galaxy mergers have a huge effect on the gas content within galaxies. SF is not constant through time; the SFR of the Milky Way was highest billions of years ago. At scales below those in this thesis, the physics within accretion disks affect the masses of stars and the formation of planets. The high resolution achievable with interferometry has made detailed studies of cores possible, and has enabled us to observe SF at the cloud level in external galaxies. The prevalence of open-access archival data allows us to combine data observed in differing ways for a more thorough picture of the ISM.

The ISM cannot be studied in isolation. Matter flows from large scales, funneled by filaments onto cores. It is ejected by outflows from YSOs and at stellar death, ionized by bright stars, and again cools and forms dense clouds. These dense molecular clouds could not exist without an outer shielding layer of more diffuse atomic gas. Turbulence, pressure, gravity, and magnetic fields all affect the ISM in unique and sometimes unpredictable ways. All processes within the ISM are interconnected, and they in turn connect to galaxy evolution, stellar evolution, and planetary formation.

In this complex field, it is crucial to understand how various factors affect each other. Observational uncertainties add a further layer of complications to astronomy. Many seemingly apparent conclusions can be the result of observational limitations: resolution, noise, or of assumptions made during data reduction and analysis.

Using a large array of data, both self-observed and archival, this thesis demonstrates the wide variance in the properties of clouds and cores. Both PAPER-I and the B-FROST survey provide data which can be used by the community to draw conclusions on cloud and core properties across a wide range of environments. PAPER-II and PAPER-V focused on one region, but show the importance of being critical of universal properties and illustrate the importance of observations at differing resolution. PAPER-IV has demonstrated both the observing capabilities and also some drawbacks of the ngVLA interferometer, which can in the future be

CHAPTER 7. CONCLUDING REMARKS

used by the global astronomical community to observe the smallest scales of SF and answer questions about the evolution of cores.

Many questions about SF and the evolution of the ISM still remain. The question of the canonical 0.1 pc width of filaments is still hotly debated in the community. In PAPER-II we compared continuum observations, but even at the ArTéMiS resolution the smallest-scale filaments are not resolved. While molecular line observations of the region exist, they do not necessarily trace the same structures. Extinction observations are also limited by the background emission within the region. Future JWST or interferometric continuum observations would detect whether filamentary structure is visible also at au-scales in the OMC-3 cloud, possibly clarifying the multiscale structure of a dense filament. Furthermore, observations of the same region, tracing the same material, will help us to connect the filamentary scales to fragmentation and subparsec-scale physics.

With increasing computational power, more detailed modeling of observations is possible. Future observations able to resolve core-scale physics can help constrain these models, making accurate studies of the Galaxy achievable. A connection of modeling and observations is crucial to understand exactly how observational uncertainties and projection effects change our analysis of the data. Comparing results from differing publications is difficult: assumptions made during analysis can dramatically change the results. Without an understanding of these differences it is impossible to properly compare results in the literature.

PAPER-III was limited in its scope due to a lack of data: only one of the three fields has higher-resolution *Herschel* data, and due to issues with the TRAO observations we were not able to use the ^{13}CO data for the λ Orionis West cloud. The filamentary "wings" streaming behind this cloud and blown away by stellar winds would be a fascinating region to understand how these pillar-like structures form and evolve. High-resolution polarization data of the λ Orionis cloud could answer questions of magnetic support at smaller scales which is not possible with *Planck* data.

The field of ISM research is an ever-evolving field. As we answer old questions, new ones are revealed. With high-resolution observations, all-sky surveys at multiple wavelengths, and increasing computing power we are able to probe deeper into interstellar clouds, answering fundamental questions about the birth of stars- and even of our own solar system.

Bibliography

- Acharyya, K., Fuchs, G. W., Fraser, H. J., van Dishoeck, E. F., & Linnartz, H. 2007, *Astronomy & Astrophysics*, 466, 1005
- Ahmadi, A., Beuther, H., Bosco, F., et al. 2023, *Astronomy & Astrophysics*, 677, A171
- Allamandola, L. J., Tielens, A. G. G. M., & Barker, J. R. 1985, *The Astrophysical Journal Letters*, 290, L25
- Alves, J., Lombardi, M., & Lada, C. J. 2007, *Astronomy & Astrophysics*, 462, L17
- Alves, J., Zucker, C., Goodman, A. A., et al. 2020, *Nature*, 578, 237
- André, P., Di Francesco, J., Ward-Thompson, D., et al. 2014, in *Protostars and Planets VI*, ed. H. Beuther, R. S. Klessen, C. P. Dullemond, & T. Henning, 27
- Andre, P., Ward-Thompson, D., & Barsony, M. 1993, *The Astrophysical Journal*, 406, 122
- André, P., Men'shchikov, A., Bontemps, S., et al. 2010, *Astronomy & Astrophysics*, 518, L102
- André, P., Revéret, V., Könyves, V., et al. 2016, *Astronomy & Astrophysics*, 592, A54
- André, P. J., Palmeirim, P., & Arzoumanian, D. 2022, *Astronomy & Astrophysics*, 667, L1
- Andrews, S. M., Huang, J., Pérez, L. M., et al. 2018, *The Astrophysical Journal Letters*, 869, L41
- APEX. 2024, ARTEMIS

BIBLIOGRAPHY

- Arzoumanian, D., André, P., Didelon, P., et al. 2011, *Astronomy & Astrophysics*, 529, L6
- Ballesteros-Paredes, J., & Hartmann, L. 2007, *Revista Mexicana de Astronomia y Astrofisica*, 43, 123
- Bally, J., Langer, W. D., Stark, A. A., & Wilson, R. W. 1987, *The Astrophysical Journal Letters*, 312, L45
- Beckwith, S. V. W., Sargent, A. I., Chini, R. S., & Guesten, R. 1990, *The Astronomical Journal*, 99, 924
- Beltrán, M. T., & de Wit, W. J. 2016, *The Astronomy and Astrophysics Review*, 24, 6
- Beltrán, M. T., Padovani, M., Galli, D., et al. 2024, *Astronomy & Astrophysics*, 686, A281
- Benedettini, M., Schisano, E., Pezzuto, S., et al. 2015, *Monthly Notices of the Royal Astronomical Society*, 453, 2036
- Bergin, E. A., Langer, W. D., & Goldsmith, P. F. 1995, *The Astrophysical Journal*, 441, 222
- Berry, D. S. 2015, *Astronomy and Computing*, 10, 22
- Bertulani, C. A. 2013, Nuclei in the Cosmos (WORLD SCIENTIFIC), 10, https://www.worldscientific.com/doi/suppl/10.1142/8573/suppl_file/8573_chap01.pdf, accessed 28.7.2025
- Beuther, H., & Henning, T. 2009, *Astronomy & Astrophysics*, 503, 859
- Beuther, H., Kuiper, R., & Tafalla, M. 2025, *Annual Review of Astronomy & Astrophysics*, 63, 1
- Beuther, H., Leurini, S., Schilke, P., et al. 2007, *Astronomy & Astrophysics*, 466, 1065
- Beuther, H., Henning, T., Linz, H., et al. 2015, *Astronomy & Astrophysics*, 581, A119
- Beuther, H., Gieser, C., Soler, J. D., et al. 2024, *Astronomy & Astrophysics*, 682, A81

BIBLIOGRAPHY

- Blitz, L., Bloemen, J. B. G. M., Hermsen, W., & Bania, T. M. 1985, *Astronomy & Astrophysics*, 143, 267
- Blitz, L., & Shu, F. H. 1980, *The Astrophysical Journal*, 238, 148
- Bobylev, V. V. 2014, *Astrophysics*, 57, 583
- Bohlin, R. C., Savage, B. D., & Drake, J. F. 1978, *The Astrophysical Journal*, 224, 132
- Bolatto, A. D., Wolfire, M., & Leroy, A. K. 2013, *Annual Review of Astronomy & Astrophysics*, 51, 207
- Bonnell, I. A., Bate, M. R., Clarke, C. J., & Pringle, J. E. 2001, *Monthly Notices of the Royal Astronomical Society*, 323, 785
- Bonnell, I. A., & Davies, M. B. 1998, *Monthly Notices of the Royal Astronomical Society*, 295, 691
- Boogert, A. C. A., Gerakines, P. A., & Whittet, D. C. B. 2015, *Annual Review of Astronomy & Astrophysics*, 53, 541
- Boogert, A. C. A., Huard, T. L., Cook, A. M., et al. 2011, *The Astrophysical Journal*, 729, 92
- Bovy, J. 2017, *Monthly Notices of the Royal Astronomical Society*, 470, 1360
- Brand, J., & Blitz, L. 1993, *Astronomy & Astrophysics*, 275, 67
- Bresnahan, D., Ward-Thompson, D., Kirk, J. M., et al. 2018, *Astronomy & Astrophysics*, 615, A125
- Cami, J., Bernard-Salas, J., Peeters, E., & Malek, S. E. 2010, *Science*, 329, 1180
- CASA Team, Bean, B., Bhatnagar, S., et al. 2022, *Publications of the Astronomical Society of the Pacific*, 134, 114501
- CDMS. 2025, Cologne Database for Molecular Spectroscopy: Molecules in Space
- Chiar, J. E., Adamson, A. J., Kerr, T. H., & Whittet, D. C. B. 1995, *The Astrophysical Journal*, 455, 234
- Chiar, J. E., Pendleton, Y. J., Allamandola, L. J., et al. 2011, *The Astrophysical Journal*, 731, 9

BIBLIOGRAPHY

- Clark, P. C., Glover, S. C. O., Klessen, R. S., & Bonnell, I. A. 2012, Monthly Notices of the Royal Astronomical Society, 424, 2599
- Cohen, R. S., Cong, H., Dame, T. M., & Thaddeus, P. 1980, The Astrophysical Journal Letters, 239, L53
- Commerçon, B., González, M., Mignon-Risse, R., Hennebelle, P., & Vaytet, N. 2022, Astronomy & Astrophysics, 658, A52
- Commerçon, B., Hennebelle, P., & Henning, T. 2011, The Astrophysical Journal Letters, 742, L9
- Compiègne, M., Verstraete, L., Jones, A., et al. 2011, Astronomy & Astrophysics, 525, A103
- Cunha, K., & Smith, V. V. 1996, Astronomy & Astrophysics, 309, 892
- Cutri, R. M., Skrutskie, M. F., van Dyk, S., et al. 2003, VizieR Online Data Catalog, II/246
- Dame, T. M., Elmegreen, B. G., Cohen, R. S., & Thaddeus, P. 1986, The Astrophysical Journal, 305, 892
- Dame, T. M., & Thaddeus, P. 1994, The Astrophysical Journal Letters, 436, L173
- de Almeida, E. S. G., Marcolino, W. L. F., Bouret, J. C., & Pereira, C. B. 2019, Astronomy & Astrophysics, 628, A36
- de Wit, W. J., Testi, L., Palla, F., & Zinnecker, H. 2005, Astronomy & Astrophysics, 437, 247
- Désert, F. X., Macías-Pérez, J. F., Mayet, F., et al. 2008, Astronomy & Astrophysics, 481, 411
- Dobbs, C. L., Burkert, A., & Pringle, J. E. 2011, Monthly Notices of the Royal Astronomical Society, 417, 1318
- Dolan, C. J., & Mathieu, R. D. 2002, The Astronomical Journal, 123, 387
- Draine, B. T., Li, A., Hensley, B. S., et al. 2021, The Astrophysical Journal, 917, 3
- Dupac, X., Bernard, J. P., Boudet, N., et al. 2003, Astronomy & Astrophysics, 404, L11

BIBLIOGRAPHY

EAS. 2025, JCMT

Eden, D. J., Liu, T., Moore, T. J. T., et al. 2024, Monthly Notices of the Royal Astronomical Society, 530, 5192

Elia, D., Molinari, S., Fukui, Y., et al. 2013, The Astrophysical Journal, 772, 45

Elia, D., Molinari, S., Schisano, E., et al. 2022, The Astrophysical Journal, 941, 162

Elmegreen, B. G. 2000, The Astrophysical Journal, 530, 277

Elmegreen, B. G., & Scalo, J. 2004, Annual Review of Astronomy & Astrophysics, 42, 211

Elmegreen, D. M., & Elmegreen, B. G. 1979, The Astronomical Journal, 84, 615

EPA. 2023, Air Quality Guide for Particle Pollution

ESA. 2006, Planck operations

—. 2010, Herschel operations

ESO. 2025a, ALMA and Interferometry

—. 2025b, APEX:Reaching new heights in submillimetre astronomy

ESO, Guisard, S., & Brunier, S. 2009, The GigaGalaxy Zoom composite

Evans, II, N. J., Heiderman, A., & Vutisalchavakul, N. 2014, The Astrophysical Journal, 782, 114

Falgarone, E., Pety, J., & Hily-Blant, P. 2009, Astronomy & Astrophysics, 507, 355

Federrath, C. 2016, Monthly Notices of the Royal Astronomical Society, 457, 375

Federrath, C., Rathborne, J. M., Longmore, S. N., et al. 2016, The Astrophysical Journal, 832, 143

Ferrière, K. M. 2001, Reviews of Modern Physics, 73, 1031

Field, G. B., Goldsmith, D. W., & Habing, H. J. 1969, The Astrophysical Journal Letters, 155, L149

Fiorellino, E., Elia, D., André, P., et al. 2021, Monthly Notices of the Royal Astronomical Society, 500, 4257

BIBLIOGRAPHY

- Fissel, L. M., Ade, P. A. R., Angilè, F. E., et al. 2019, *The Astrophysical Journal*, 878, 110
- Gaia. 2022, Gaia Data Release 3 (Gaia DR3)
- Gieser, C., Beuther, H., Semenov, D., et al. 2023, *Astronomy & Astrophysics*, 674, A160
- Gillett, F. C., Forrest, W. J., & Merrill, K. M. 1973, *The Astrophysical Journal*, 183, 87
- Glover, S. C. O., & Mac Low, M.-M. 2007, *The Astrophysical Journal*, 659, 1317
- Goldsmith, P. F., & Li, D. 2005, *The Astrophysical Journal*, 622, 938
- Goodman, A. A., Alves, J., Beaumont, C. N., et al. 2014, *The Astrophysical Journal*, 797, 53
- Gould, B. A. 1874, *American Journal of Science and Arts*, 8, 325
- Gould, R. J., & Salpeter, E. E. 1963, *The Astrophysical Journal*, 138, 393
- Greene, T. P., Wilking, B. A., Andre, P., Young, E. T., & Lada, C. J. 1994, *The Astrophysical Journal*, 434, 614
- Griffin, M. J., Abergel, A., Abreu, A., et al. 2010, *Astronomy & Astrophysics*, 518, L3
- Güsten, R., Nyman, L. Å., Schilke, P. and Menten, K., Cesarsky, C., & Booth, R. 2006, *Astronomy & Astrophysics*, 454, L13
- Hacar, A., Tafalla, M., Forbrich, J., et al. 2018, *Astronomy & Astrophysics*, 610, A77
- Hartmann, J. 1904, *The Astrophysical Journal*, 19, 268
- Hartmann, L. 2002, *The Astrophysical Journal*, 578, 914
- Hartmann, L., Ballesteros-Paredes, J., & Bergin, E. A. 2001, *The Astrophysical Journal*, 562, 852
- Haworth, T. J., Glover, S. C. O., Koepferl, C. M., Bisbas, T. G., & Dale, J. E. 2018, *Nature Astronomy*, 82, 1

BIBLIOGRAPHY

- Hayashi, C. 1961, Publications of the Astronomical Society of the Pacific, 13, 450
- Hayashi, C., & Hoshi, R. 1961, Publications of the Astronomical Society of the Pacific, 13, 442
- Heiderman, A., Evans, Neal J., I., Allen, L. E., Huard, T., & Heyer, M. 2010, The Astrophysical Journal, 723, 1019
- Hennebelle, P. 2013, Astronomy & Astrophysics, 556, A153
- Hennebelle, P., & André, P. 2013, Astronomy & Astrophysics, 560, A68
- Hennebelle, P., & Grudić, M. Y. 2024, arXiv e-prints, arXiv:2404.07301
- Henley, L. G., Lelevier, R., & Levée, R. D. 1955, Publications of the Astronomical Society of the Pacific, 67, 154
- Herbst, E., & van Dishoeck, E. F. 2009, Annual Review of Astronomy & Astrophysics, 47, 427
- Herschel, Sir, J. F. W. 1847, Results of astronomical observations made during the years 1834, 5, 6, 7, 8, at the Cape of Good Hope; being the completion of a telescopic survey of the whole surface of the visible heavens, commenced in 1825
- Herschel Science Centre. 2017, THE HETERODYNE INSTRUMENT FOR THE FAR INFRARED (HIFI) HANDBOOK, Tech. Rep. HERSCHEL-HSC-DOC-2097, v, ESA
- Heyer, M., & Dame, T. M. 2015, Annual Review of Astronomy & Astrophysics, 53, 583
- Heyer, M. H., Carpenter, J. M., & Snell, R. L. 2001, The Astrophysical Journal, 551, 852
- Hill, T., André, P., Arzoumanian, D., et al. 2012, Astronomy & Astrophysics, 548, L6
- Hillenbrand, L. A., & Hartmann, L. W. 1998, The Astrophysical Journal, 492, 540
- Hollenbach, D., & Salpeter, E. E. 1971, The Astrophysical Journal, 163, 155
- Hollenbach, D. J., Werner, M. W., & Salpeter, E. E. 1971, The Astrophysical Journal, 163, 165

BIBLIOGRAPHY

- Howard, A. D. P., Whitworth, A. P., Marsh, K. A., et al. 2019, Monthly Notices of the Royal Astronomical Society, 489, 962
- IRSA. 2025, Planck Public Data Release 2 Maps
- Jappsen, A. K., Klessen, R. S., Larson, R. B., Li, Y., & Mac Low, M. M. 2005, Astronomy & Astrophysics, 435, 611
- Jeans, J. H. 1902, Philosophical Transactions of the Royal Society of London Series A, 199, 1
- Juvela, M. 2023, Astronomy & Astrophysics, 673, A145
- Juvela, M., Malinen, J., & Lunttila, T. 2012, Astronomy & Astrophysics, 544, A141
- Juvela, M., & Mannfors, E. 2023, Astronomy & Astrophysics, 671, A111
- Juvela, M., Mannfors, E., Liu, T., & Tóth, L. V. 2022, Astronomy & Astrophysics, 666, A74
- Juvela, M., Montillaud, J., Ysard, N., & Lunttila, T. 2013, Astronomy & Astrophysics, 556, A63
- Juvela, M., Neha, S., Mannfors, E., et al. 2020, Astronomy & Astrophysics, 643, A132
- Juvela, M., & Ysard, N. 2012, Astronomy & Astrophysics, 541, A33
- Juvela, M., Ristorcelli, I., Montier, L. A. and Marshall, D. J., et al. 2010, Astronomy & Astrophysics, 518, L93
- Juvela, M., Ristorcelli, I., Pelkonen, V. M., et al. 2011, Astronomy & Astrophysics, 527, A111
- Juvela, M., Ristorcelli, I., Marshall, D. J., et al. 2015a, Astronomy & Astrophysics, 584, A93
- Juvela, M., Demyk, K., Doi, Y., et al. 2015b, Astronomy & Astrophysics, 584, A94
- Kahn, F. D. 1974, Astronomy & Astrophysics, 37, 149
- Kainulainen, J., Beuther, H., Henning, T., & Plume, R. 2009, Astronomy & Astrophysics, 508, L35

BIBLIOGRAPHY

- Kainulainen, J., Hacar, A., Alves, J., Beuther, H. and Bouy, H., & Tafalla, M. 2016, *Astronomy & Astrophysics*, 586, A27
- Kang, S.-J., Kerton, C. R., Choi, M., & Kang, M. 2017, *The Astrophysical Journal*, 845, 21
- Karttunen, H., Donner, K. J., Kr, L., et al. 2010, *Tahtitieteen Perusteet*, 5 edn. (Helsinki: URSA)
- KASI. 2025, Taeduk Radio Astronomy Observatory (TRAO)
- Kauffmann, J., & Pillai, T. 2010, *The Astrophysical Journal Letters*, 723, L7
- Kauffmann, J., Pillai, T., Shetty, R., Myers, P. C., & Goodman, A. A. 2010a, *The Astrophysical Journal*, 712, 1137
- . 2010b, *The Astrophysical Journal*, 716, 433
- Kee, N. D., & Kuiper, R. 2019, *Monthly Notices of the Royal Astronomical Society*, 483, 4893
- Kendrew, S., Beuther, H., Simpson, R., et al. 2016, *The Astrophysical Journal*, 825, 142
- Kim, J., Chevance, M., Kruijssen, J. M. D., et al. 2022, *Monthly Notices of the Royal Astronomical Society*, 516, 3006
- Kirk, H., Klassen, M., & Pudritz, Ralph and Pillsworth, S. 2015, *The Astrophysical Journal*, 802, 75
- Klessen, R. S., Ballesteros-Paredes, J., Li, Y., & Mac Low, M. M. 2004, in *Astro- nomical Society of the Pacific Conference Series*, Vol. 322, *The Formation and Evolution of Massive Young Star Clusters*, ed. H. J. G. L. M. Lamers, L. J. Smith, & A. Nota, 299–308
- Könyves, V., André, P., Men'shchikov, A., et al. 2015, *Astronomy & Astrophysics*, 584, A91
- Kou, Z., Li, X., Qin, S.-L., et al. 2025, *Monthly Notices of the Royal Astronomical Society*, 538, 2579
- Kruegel, E., & Siebenmorgen, R. 1994, *Astronomy & Astrophysics*, 288, 929

BIBLIOGRAPHY

- Krumholz, M. R., & McKee, C. F. 2008, *Nature*, 451, 1082
- Krumholz, M. R., McKee, C. F., & Klein, R. I. 2005a, *The Astrophysical Journal Letters*, 618, L33
- . 2005b, *Nature*, 438, 332
- Lada, C. J. 1987, in *Star Forming Regions*, ed. M. Peimbert & J. Jugaku, Vol. 115, 1
- Lada, C. J., Lombardi, M., & Alves, J. F. 2010, *The Astrophysical Journal*, 724, 687
- Larson, R. B. 1981, *Monthly Notices of the Royal Astronomical Society*, 194, 809
- . 1985, *Monthly Notices of the Royal Astronomical Society*, 214, 379
- . 2003, *Reports on Progress in Physics*, 66, 1651
- Larson, R. B., & Starrfield, S. 1971, *Astronomy & Astrophysics*, 13, 190
- Le Gouellec, V. J. M., Hull, C. L. H., Maury, A. J., et al. 2019, *The Astrophysical Journal*, 885, 106
- Leger, A., & Puget, J. L. 1984, *Astronomy & Astrophysics*, 137, L5
- Lewis, J. A., Lada, C. J., & Dame, T. M. 2022, *The Astrophysical Journal*, 931, 9
- Li, A. 2020, *Nature Astronomy*, 4, 339
- Li, A., & Draine, B. T. 2001, *The Astrophysical Journal*, 554, 778
- Li, X.-M., Zhang, G.-Y., Men'shchikov, A., et al. 2023, *Astronomy & Astrophysics*, 674, A225
- Liu, H.-L., Tej, A., Liu, T., et al. 2022, *Monthly Notices of the Royal Astronomical Society*, 510, 5009
- Liu, T., Kim, K.-T., Juvela, M., et al. 2018, *The Astrophysical Journal Supplement Series*, 234, 28
- Lombardi, M. 2009, *Astronomy & Astrophysics*, 493, 735
- Lombardi, M., & Alves, J. 2001, *Astronomy & Astrophysics*, 377, 1023

BIBLIOGRAPHY

- Lombardi, M., Bouy, H., Alves, J., & Lada, C. J. 2014, *Astronomy & Astrophysics*, 566, A45
- Louvet, F., Sanhueza, P., Stutz, A., et al. 2024, *Astronomy & Astrophysics*, 690, A33
- Maddison, S. 2017, Swinburne Astronomy Online: Project 181: Classifying Young Stellar Objects
- Magnani, L., & Smith, A. J. 2010, *The Astrophysical Journal*, 722, 1685
- Mai, X., Liu, T., Liu, X., et al. 2024, *The Astrophysical Journal Letters*, 961, L35
- Malhotra, S. 1994, *The Astrophysical Journal*, 437, 194
- Malinen, J., Juvela, M., Rawlings, M. G. and Ward-Thompson, D., Palmeirim, P., & André, P. 2012, *Astronomy & Astrophysics*, 544, A50
- Mangum, J. G., & Shirley, Y. L. 2015, *Publications of the Astronomical Society of the Pacific*, 127, 266
- Mannfors, E., Juvela, M., Liu, T., & Pelkonen, V. M. 2025, *Astronomy & Astrophysics*, 695, A242
- Mannfors, E., Juvela, M., Bronfman, L., et al. 2021, *Astronomy & Astrophysics*, 654, A123
- McKee, C. F., & Krumholz, M. R. 2010, *The Astrophysical Journal*, 709, 308
- McKee, C. F., & Ostriker, J. P. 1977, *The Astrophysical Journal*, 218, 148
- McKee, C. F., & Tan, J. C. 2003, *The Astrophysical Journal*, 585, 850
- McKellar, A. 1940, *Publications of the Astronomical Society of the Pacific*, 52, 187
- Mennella, V., Brucato, J. R., Colangeli, L., et al. 1998, *The Astrophysical Journal*, 496, 1058
- Men'shchikov, A., André, P., Didelon, P., et al. 2010, *Astronomy & Astrophysics*, 518, L103
- Meny, C., Gromov, V., Boudet, N., Bernard, J. Ph. and Paradis, D., & Nayral, C. 2007, *Astronomy & Astrophysics*, 468, 171

BIBLIOGRAPHY

- Merrill, P. W. 1934, Publications of the Astronomical Society of the Pacific, 46, 206
- . 1936, The Astrophysical Journal, 83, 126
- Messenger, S., Keller, L., & Nakamura-Messenger, K. 2013, Dust in the Solar System - Properties and Origins
- Molinari, S., Swinyard, B., Bally, J., et al. 2010, Astronomy & Astrophysics, 518, L100
- Montillaud, J., Juvela, M., Rivera-Ingraham, A. and Malinen, J., et al. 2015, Astronomy & Astrophysics, 584, A92
- Motte, F., & André, P. 2001, Astronomy & Astrophysics, 365, 440
- Motte, F., Bontemps, S., & Louvet, F. 2018a, Annual Review of Astronomy & Astrophysics, 56, 41
- Motte, F., Nony, T., Louvet, F., et al. 2018b, Nature Astronomy, 2, 478
- MPA. 2025, The Millennium Simulation Project
- Murillo, N. M., Lai, S.-P., Bruderer, S., Harsono, D., & van Dishoeck, E. F. 2013, Astronomy & Astrophysics, 560, A103
- Myers, P. C. 2009, The Astrophysical Journal, 700, 1609
- Nakamura, F., & Li, Z.-Y. 2008, The Astrophysical Journal, 687, 354
- Nakano, T. 1989, The Astrophysical Journal, 345, 464
- Narayanan, D., Krumholz, M. R., Ostriker, E. C., & Hernquist, L. 2012, Monthly Notices of the Royal Astronomical Society, 421, 3127
- NASA. 2019, Spitzer Space Telescope
- Norris, R. 2007, The Emu in the Sky
- NRAO. 2025a, ALMA Basics
- . 2025b, The Karl G. Jansky Very Large Array
- . 2025c, ngVLA
- NREL. 2025, Solar Spectra

BIBLIOGRAPHY

- Nutter, D., Kirk, J. M., Stamatellos, D., & Ward-Thompson, D. 2008, Monthly Notices of the Royal Astronomical Society, 384, 755
- Offner, S. S. R., Clark, P. C., Hennebelle, P., et al. 2014, in Protostars and Planets VI, ed. H. Beuther, R. S. Klessen, C. P. Dullemond, & T. Henning, 53–75
- Oka, T., Hasegawa, T., Sato, F., et al. 2001, The Astrophysical Journal, 562, 348
- Ossenkopf, V., & Henning, T. 1994, Astronomy & Astrophysics, 291, 943
- Ostriker, E. C., Gammie, C. F., & Stone, J. M. 1999, The Astrophysical Journal, 513, 259
- Ostriker, E. C., Stone, J. M., & Gammie, C. F. 2001, The Astrophysical Journal, 546, 980
- Ostriker, J. 1964, The Astrophysical Journal, 140, 1056
- Padoan, P., Juvela, M., Goodman, A. A., & Nordlund, Å. 2001, The Astrophysical Journal, 553, 227
- Padoan, P., Pan, L., Juvela, M., Haugbølle, T., & Nordlund, Å. 2020, The Astrophysical Journal, 900, 82
- Palau, A., Estalella, R., Girart, J. M., et al. 2014, The Astrophysical Journal, 785, 42
- Palau, A., Zhang, Q., Girart, J. M., et al. 2021, The Astrophysical Journal, 912, 159
- Palla, F., & Stahler, S. W. 1993, The Astrophysical Journal, 418, 414
- Palmeirim, P., André, P., Kirk, J. and Ward-Thompson, D., et al. 2013, Astronomy & Astrophysics, 550, A38
- Palmeirim, P., Zavagno, A., Elia, D., et al. 2017, Astronomy & Astrophysics, 605, A35
- Panopoulou, G. V., Clark, S. E., Hacar, A., et al. 2022, Astronomy & Astrophysics, 657, L13
- Panopoulou, G. V., Psarakis, I., Skalidis, R., Tassis, K., & Andrews, J. J. 2017, Monthly Notices of the Royal Astronomical Society, 466, 2529

BIBLIOGRAPHY

- Paradis, D., Veneziani, M., Noriega-Crespo, A., et al. 2010, *Astronomy & Astrophysics*, 520, L8
- Parker, R. J., Pinson, E. J., Alcock, H. L., & Dale, J. E. 2024, *The Astrophysical Journal*, 974, 8
- Pattle, K., Fissel, L., Tahani, M., Liu, T., & Ntormousi, E. 2023, in *Astronomical Society of the Pacific Conference Series*, Vol. 534, *Protostars and Planets VII*, ed. S. Inutsuka, Y. Aikawa, T. Muto, K. Tomida, & M. Tamura, 193
- Pattle, K., Lai, S.-P., Wright, M., et al. 2021, *Monthly Notices of the Royal Astronomical Society*, 503, 3414
- Peretto, N., Fuller, G. A., André, P., et al. 2014, *Astronomy & Astrophysics*, 561, A83
- Pilbratt, G. L., Riedinger, J. R., Passvogel, T. andCrone, G., et al. 2010, *Astronomy & Astrophysics*, 518, L1
- Pillai, T., Kauffmann, J., Wyrowski, F., et al. 2011, *Astronomy & Astrophysics*, 530, A118
- Pineda, J. E., Caselli, P., & Goodman, A. A. 2008, *The Astrophysical Journal*, 679, 481
- Pineda, J. E., Segura-Cox, D., Caselli, P., et al. 2020, *Nature Astronomy*, 4, 1158
- Pineda, J. L., Goldsmith, P. F., Chapman, N., et al. 2010, *The Astrophysical Journal*, 721, 686
- Planck Collaboration, Ade, P. A. R., Aghanim, N., et al. 2011a, *Astronomy & Astrophysics*, 536, A22
- . 2011b, *Astronomy & Astrophysics*, 536, A23
- Planck Collaboration, Abergel, A., Ade, P. A. R., et al. 2014, *Astronomy & Astrophysics*, 571, A11
- Planck Collaboration, Ade, P. A. R., Aghanim, N., et al. 2016a, *Astronomy & Astrophysics*, 594, A28
- Planck Collaboration, Ade, P. A. R., Aghanim, N. andAlves, M. I. R., et al. 2016b, *Astronomy & Astrophysics*, 586, A138

BIBLIOGRAPHY

- Plummer, H. C. 1911, Monthly Notices of the Royal Astronomical Society, 71, 460
- Poglitsch, A., Waelkens, C., Geis, N., et al. 2010, Astronomy & Astrophysics, 518, L2
- Polychroni, D., Schisano, E., Elia, D., et al. 2013, The Astrophysical Journal Letters, 777, L33
- Ragan, S. E., Henning, T., Tackenberg, J., et al. 2014, Astronomy & Astrophysics, 568, A73
- Raghavan, D., McAlister, H. A., Henry, T. J., et al. 2010, The Astrophysical Journal Supplement Series, 190, 1
- Recchi, S., Hacar, A., & Palestini, A. 2013, Astronomy & Astrophysics, 558, A27
- Reid, N., & Hawley, S. 2006, New Light on Dark Stars: Red Dwarfs, Low-Mass Stars, Brown Stars, 2nd edn. (Springer Science & Business Media), 108, https://books.google.com/books?id=o7pe7Fp4JaAC&pg=PA108&redir_esc=y#v=onepage&q&f=false, accessed 28.7.2025
- Ren, Z., Chen, X., Liu, T., et al. 2023, The Astrophysical Journal, 955, 104
- Revéret, V., André, P., Le Pennec, J., et al. 2014, in Society of Photo-Optical Instrumentation Engineers (SPIE) Conference Series, Vol. 9153, Millimeter, Submillimeter, and Far-Infrared Detectors and Instrumentation for Astronomy VII, ed. W. S. Holland & J. Zmuidzinas, 915305
- Rieke, G. H. 2009, Experimental Astronomy, 25, 125
- Ripple, F., Heyer, M. H., Gutermuth, R., Snell, R. L., & Brunt, C. M. 2013, Monthly Notices of the Royal Astronomical Society, 431, 1296
- Rivera-Ingraham, A., Ristorcelli, I., Juvela, M., et al. 2016, Astronomy & Astrophysics, 591, A90
- Robitaille, T., Rice, T., Beaumont, C., et al. 2019
- Robitaille, T. P., Whitney, B. A., Indebetouw, R., Wood, K., & Denzmore, P. 2006, The Astrophysical Journal Supplement Series, 167, 256
- Rosen, A. L. 2022, The Astrophysical Journal, 941, 202

BIBLIOGRAPHY

- Rosolowsky, E. W., Pineda, J. E., Kauffmann, J., & Goodman, A. A. 2008, *The Astrophysical Journal*, 679, 1338
- Sadavoy, S. I., di Francesco, J., André, P., et al. 2012, *Astronomy & Astrophysics*, 540, A10
- Saha, P., Gopinathan, M., Ojha, D. K., & Neha, S. 2022, *Monthly Notices of the Royal Astronomical Society*, 510, 2644
- Saintonge, A., & Catinella, B. 2022, *Annual Review of Astronomy & Astrophysics*, 60, 319
- Saintonge, A., Lutz, D., Genzel, R., et al. 2013, *The Astrophysical Journal*, 778, 2
- Salji, C. J., Richer, J. S., Buckle, J. V., et al. 2015, *Monthly Notices of the Royal Astronomical Society*, 449, 1782
- Salpeter, E. E. 1955, *The Astrophysical Journal*, 121, 161
- Sana, H., Le Bouquin, J. B., Lacour, S., et al. 2014, *The Astrophysical Journal Supplement Series*, 215, 15
- Sánchez-Monge, Á., Palau, A., Fontani, F., et al. 2013, *Monthly Notices of the Royal Astronomical Society*, 432, 3288
- Schinnerer, E., & Leroy, A. K. 2024, *Annual Review of Astronomy & Astrophysics*, 62, 369
- Schisano, E., Rygl, K. L. J., Molinari, S., et al. 2014, *The Astrophysical Journal*, 791, 27
- Schneider, S., & Elmegreen, B. G. 1979, *The Astrophysical Journal Supplement Series*, 41, 87
- Schuller, F., André, P., Shimajiri, Y., et al. 2021, *Astronomy & Astrophysics*, 651, A36
- Scoville, N. Z., & Hersh, K. 1979, *The Astrophysical Journal*, 229, 578
- Sheffer, Y., Rogers, M., Federman, S. R., et al. 2008, *The Astrophysical Journal*, 687, 1075
- Shetty, R., Beaumont, C. N., Burton, M. G., Kelly, B. C., & Klessen, R. S. 2012, *Monthly Notices of the Royal Astronomical Society*, 425, 720

BIBLIOGRAPHY

- Shetty, R., Kauffmann, J., Schnee, S., & Goodman, A. A. 2009a, *The Astrophysical Journal*, 696, 676
- Shetty, R., Kauffmann, J., Schnee, S., Goodman, A. A., & Ercolano, B. 2009b, *The Astrophysical Journal*, 696, 2234
- Singh, A., Matzner, C. D., Friesen, R. K., et al. 2021, *The Astrophysical Journal*, 922, 87
- Smith, R. J., Glover, S. C. O., Clark, P. C., Klessen, R. S., & Springel, V. 2014a, *Monthly Notices of the Royal Astronomical Society*, 441, 1628
- Smith, R. J., Glover, S. C. O., & Klessen, R. S. 2014b, *Monthly Notices of the Royal Astronomical Society*, 445, 2900
- Sodroski, T. J., Odegard, N., Dwek, E., et al. 1995, *The Astrophysical Journal*, 452, 262
- Solomon, P. M., & Klemperer, W. 1972, *The Astrophysical Journal*, 178, 389
- Solomon, P. M., Rivolo, A. R., Barrett, J., & Yahil, A. 1987, *The Astrophysical Journal*, 319, 730
- Solomon, P. M., & Wickramasinghe, N. C. 1969, *The Astrophysical Journal*, 158, 449
- Steinacker, J., Baes, M., & Gordon, K. D. 2013, *Annual Review of Astronomy & Astrophysics*, 51, 63
- Steinacker, J., Pagani, L., Bacmann, A., & Guieu, S. 2010, *Astronomy & Astrophysics*, 511, A9
- Stepnik, B., Abergel, A., Bernard, J. P., et al. 2003, *Astronomy & Astrophysics*, 398, 551
- Sternberg, A., & Dalgarno, A. 1995, *The Astrophysical Journal Supplement Series*, 99, 565
- Sternberg, A., Le Petit, F., Roueff, E., & Le Bourlot, J. 2014, *The Astrophysical Journal*, 790, 10
- Stodółkiewicz, J. S. 1963, *Acta Astronomica*, 13, 30

BIBLIOGRAPHY

- Stutzki, J. 2014, GAUSSCLUMPS: Gaussian-shaped clumping from a spectral map, *Astrophysics Source Code Library*, ascl:1406.018
- Sun, J., Leroy, A. K., Rosolowsky, E., et al. 2022, *The Astronomical Journal*, 164, 43
- Swings, P., & Rosenfeld, L. 1937, *The Astrophysical Journal*, 86, 483
- Szúcs, L., Glover, S. C. O., & Klessen, R. S. 2014, *Monthly Notices of the Royal Astronomical Society*, 445, 4055
- . 2016, *Monthly Notices of the Royal Astronomical Society*, 460, 82
- Tabatabaei, F. S., Redaelli, E., Galli, D., et al. 2024, *Astronomy & Astrophysics*, 688, A98
- Tacconi, L. J., Neri, R., Genzel, R., et al. 2013, *The Astrophysical Journal*, 768, 74
- Tafalla, M., & Hacar, A. 2015, *Astronomy & Astrophysics*, 574, A104
- Tobin, J. J., & Sheehan, P. D. 2024, *Annual Review of Astronomy & Astrophysics*, 62, 203
- Tobin, J. J., Dunham, M. M., Looney, L. W., et al. 2015, *The Astrophysical Journal*, 798, 61
- Toci, C., & Galli, D. 2015, *Monthly Notices of the Royal Astronomical Society*, 446, 2110
- Traficante, A., Jones, B. M., Avison, A., et al. 2023, *Monthly Notices of the Royal Astronomical Society*, 520, 2306
- Treviño-Morales, S. P., Fuente, A., Sánchez-Monge, Á., et al. 2019, *Astronomy & Astrophysics*, 629, A81
- Valdivia-Mena, M. T., Pineda, J. E., Segura-Cox, D. M., et al. 2022, *Astronomy & Astrophysics*, 667, A12
- van Dishoeck, E. F., & Black, J. H. 1988, *The Astrophysical Journal*, 334, 771
- Vázquez-Semadeni, E., Palau, A., Ballesteros-Paredes, J., Gómez, G. C., & Zamora-Avilés, M. 2019, *Monthly Notices of the Royal Astronomical Society*, 490, 3061

BIBLIOGRAPHY

- Visser, R., van Dishoeck, E. F., & Black, J. H. 2009, *Astronomy & Astrophysics*, 503, 323
- Vogel, R. 2019, strange young stars
- Ward-Thompson, D., & Whitworth, A. P. 2011, An Introduction to Star Formation
- Watkins, L. L., van der Marel, R. P., Sohn, S. T., & Evans, N. W. 2019, *The Astrophysical Journal*, 873, 118
- Werner, M. W., Roellig, T. L., Low, F. J., et al. 2004, *The Astrophysical Journal Supplement Series*, 154, 1
- Whittet, D. C. B., Cook, A. M., Herbst, E., Chiar, J. E., & Shenoy, S. S. 2011, *The Astrophysical Journal*, 742, 28
- Williams, J. P., de Geus, E. J., & Blitz, L. 1994, *The Astrophysical Journal*, 428, 693
- Wilson, R. W., Jefferts, K. B., & Penzias, A. A. 1970, *The Astrophysical Journal Letters*, 161, L43
- Winters, J. G., Henry, T. J., Jao, W.-C., et al. 2019, *The Astronomical Journal*, 157, 216
- Woon, D. 2025, Interstellar & circumstellar molecules
- Wyrowski, F., Güsten, R., Menten, K. M., et al. 2016, *Astronomy & Astrophysics*, 585, A149
- Yamamoto, S. 2017, *Introduction to Astrochemistry : Chemical Evolution from Interstellar Clouds to Star and Planet Formation* (Springer Japan), 293, <http://ebookcentral.proquest.com/lib/helsinki-ebooks/detail.action?docID=4804630>
- Yen, H.-W., Gu, P.-G., Hirano, N., et al. 2019, *The Astrophysical Journal*, 880, 69
- Yen, H.-W., Takakuwa, S., Ohashi, N., et al. 2014, *The Astrophysical Journal*, 793, 1
- Yi, H.-W., Lee, J.-E., Liu, T., et al. 2018, *The Astrophysical Journal Supplement Series*, 236, 51

BIBLIOGRAPHY

- Yorke, H. W., & Kruegel, E. 1977, *Astronomy & Astrophysics*, 54, 183
- Zavagno, A., André, P., Schuller, F., et al. 2020, *Astronomy & Astrophysics*, 638, A7
- Zhang, C., Zhang, G.-Y., Li, J.-Z., & Li, X.-M. 2022, *Research in Astronomy and Astrophysics*, 22, 055012
- Zhang, G.-Y., André, P., Men'shchikov, A., & Wang, K. 2020, *Astronomy & Astrophysics*, 642, A76
- Zhang, Q., Qiu, K., Girart, J. M., et al. 2014, *The Astrophysical Journal*, 792, 116
- Zhang, X., Qiu, K., Zhang, Q., et al. 2024, *Astronomy & Astrophysics*, 684, A142
- Zinnecker, H. 1982, *Annals of the New York Academy of Sciences*, 395, 226
- Zinnecker, H., & Yorke, H. W. 2007, *Annual Review of Astronomy & Astrophysics*, 45, 481
- Zucker, C., Battersby, C., & Goodman, A. 2015, *The Astrophysical Journal*, 815, 23
- Zucker, C., Speagle, J. S., Schlafly, E. F., et al. 2019, *The Astrophysical Journal*, 879, 125